Energy Research and Development Division

FINAL PROJECT REPORT

ADVANCED ENERGY DELIVERY FOR FOOD PROCESSING: DIRECT STEAM GENERATION IN PARABOLIC TROUGH SOLAR COLLECTORS

Appendices

Prepared for: California Energy Commission

Prepared by: Abengoa Solar LLC

AUGUST 2013

CEC-500-2014-073-APB-APD

ABENGOA

Prepared by:

Primary Author(s):
E. Kenneth May
Angelo Chialva

Abengoa Solar LLC
11500 West 13th Avenue
Lakewood, CO 80215
303-928-8500
www.abengoasolar.com

Olivier Desjardins
Jeremy McCaslin

Sibley School of Mechanical and Aerospace Engineering
Cornell University, Ithaca, NY 14853

Contract Number: PIR-09-003

Prepared for:

California Energy Commission

Michael Lozano
Contract Manager

Virginia Lew
Office Manager
Energy Efficiency Research Office

Laurie Ten-Hope
Deputy Director
ENERGY RESEARCH AND DEVELOPMENT DIVISION

Robert P. Oglesby
Executive Director

DISCLAIMER

This report was prepared as the result of work sponsored by the California Energy Commission. It does not necessarily represent the views of the Energy Commission, its employees or the State of California. The Energy Commission, the State of California, its employees, contractors and subcontractors make no warrant, express or implied, and assume no legal liability for the information in this report; nor does any party represent that the uses of this information will not infringe upon privately owned rights. This report has not been approved or disapproved by the California Energy Commission nor has the California Energy Commission passed upon the accuracy or adequacy of the information in this report.

ACKNOWLEGMENTS

The primary authors Ken May and Angelo Chialva acknowledge the support of the California Energy Commission in funding this work and Abengoa Solar Inc. for funding its participant cost share. We would also like to acknowledge the contribution of Professor Olivier Desjardins and his graduate student Jeremy McCaslin, from the University of Colorado, Boulder. Both are currently at Cornell University for their ground breaking contribution in applying Computational Fluid Dynamics to this complex problem of two-phase horizontal flow with thermal energy input.

PREFACE

The California Energy Commission Energy Research and Development Division supports public interest energy research and development that will help improve the quality of life in California by bringing environmentally safe, affordable, and reliable energy services and products to the marketplace.

The Energy Research and Development Division conducts public interest research, development, and demonstration (RD&D) projects to benefit California.

The Energy Research and Development Division strives to conduct the most promising public interest energy research by partnering with RD&D entities, including individuals, businesses, utilities, and public or private research institutions.

Energy Research and Development Division funding efforts are focused on the following RD&D program areas:

- Buildings End-Use Energy Efficiency
- Energy Innovations Small Grants
- Energy-Related Environmental Research
- Energy Systems Integration
- Environmentally Preferred Advanced Generation
- Industrial/Agricultural/Water End-Use Energy Efficiency
- Renewable Energy Technologies
- Transportation

This is the final report on the subject of Advanced Energy Delivery for Food Processing: Direct Steam Generation in Parabolic Trough Solar Collectors under grant award number PIR-09-003 conducted by Abengoa Solar LLC. The information from this project contributes to the Energy Research and Development Divisions's Industrial/Agricultural/Water End-Use Energy Efficiency

For more information about the Energy Research and Development Division, please visit the Energy Commission's website at www.energy.ca.gov/research/ or contact the Energy Commission at 916-327-1551.

ABSTRACT

Food processing is the third largest industrial energy user in California consuming 600 million therms of natural gas and 3,700 million kWh per year. This industry is a major user of low temperature heat and a prime target for using solar technology. Steam is a common mode of energy delivery in the industry and technologies to reduce solar steam costs will improve competitiveness in the market place.

Direct steam generation (DSG) in the absorber tube of a parabolic trough collector could reduce steam costs by increasing thermal output and reducing capital costs compared to existing technology. This report addresses the technical challenges of commercializing industrial DSG technology.

Abengoa Solar built a pilot plant for operational experience in DSG and to generate data to develop models that would be used in the design of commercial installations. Experiments under varying conditions of steam flow, pressure and solar radiation confirmed the performance advantages of DSG, demonstrated the stability of this process and discovered no mechanical issues that would preclude the industrial use of the technique.

Future work is required to develop theoretical correlations of the experimental data. These correlations would be used to design the pipe network of a commercial DSG plant and to test the stability of the network against flow excursions. The cost and performance of the commercial design would be compared against the parameters of conventional technology to determine the economic benefits of DSG technology.

A first commercial demonstration DSG plant would be necessary to accelerate the technology in the marketplace.

Keywords: California Energy Commission, solar collectors, solar concentrators, parabolic troughs, solar thermal, solar heat generation, solar steam generation, two phase flow, direct steam generation, computational fluid dynamics, food processing industry, renewable energy, industrial process heat, San Joaquin Valley

Report citation:

May, E. Kenneth; Chialva, Angelo. (Abengoa Solar LLC) 2013. ***Advanced Energy Delivery for Food Processing: Direct Steam Generation in Parabolic Trough Solar Collectors.*** California Energy Commission. Publication number: CEC-500-2014-073-APB-APD.

TABLE OF CONTENTS

ACKNOWLEGMENTS i

PREFACE ii

ABSTRACT iii

TABLE OF CONTENTS iv

APPENDIX B: First-Principle-Based Modeling of Direct Steam Generation Final Report B-1

APPENDIX C: Design of DSG Solar Pilot Plant C-1

APPENDIX D: Results of DSG Experiments D-1

APPENDIX B:
First-Principle-Based Modeling of Direct Steam Generation
Final Report

Olivier Desjardins. "First-principle-based modeling of Direct Steam Generation, Final Report", September 2, 2011, Sibley School of Mechanical and Aerospace Engineering, Cornell University, Ithaca, NY 14853

APPENDIX C:
Design of DSG Solar Pilot Plant

APPENDIX D:
Results of DSG Experiments

First-principle-based modeling of Direct Steam Generation

Final report submitted by:

Olivier Desjardins (PI)

Sibley School of Mechanical and Aerospace Engineering
Cornell University
Ithaca, NY 14853

Submitted to:
Abengoa Solar
Lakewood, CO 80215

For the period:
September 3, 2010 through September 2, 2011

Contract number:
OCG5478B

Contents

1 Introduction **4**
1.1 Background . . . 4
1.2 Objective . . . 4
1.3 Challenges and opportunities . . . 5
1.4 Overview of this report . . . 6

2 Literature findings **6**
2.1 Observed flow regimes . . . 6
2.2 Experimental and numerical work . . . 8
2.3 Flow pattern maps . . . 8
2.4 Heat transfer and pressure drop correlations . . . 10
2.4.1 Discussion of two-phase pressure drop . . . 11
2.4.2 A note on annular flow . . . 15
2.4.3 Discussion of two-phase heat transfer . . . 15
2.5 Possible reference experiments . . . 16
2.6 Localization of DSG on regime maps . . . 17

3 Computational approach **18**
3.1 Mathematical formulation . . . 18
3.2 Numerical methodology . . . 18
3.3 Discontinuous Galerkin Conservative Level Set . . . 19
3.3.1 Accurate Conservative Level Set approach . . . 19
3.3.2 Discontinuous Galerkin discretization . . . 20
3.3.3 Curvature computation . . . 22
3.3.4 Scalability . . . 22
3.4 High density ratio correction . . . 23
3.5 Simulation strategy . . . 25
3.5.1 Level of resolution . . . 25
3.5.2 NGA . . . 26
3.5.3 Computational domain . . . 26

4 Preliminary work **27**
4.1 Test case . . . 27
4.2 Flow forcing . . . 28
4.3 Transverse gravity . . . 31
4.4 Three dimensions . . . 31

5 Resolution requirements **33**
5.1 Turbulent scaling arguments for DNS . . . 33
5.1.1 General Reynolds number considerations . . . 33
5.1.2 Frictional resolution requirements . . . 34
5.1.3 Gas-liquid interface resolution requirements . . . 35
5.2 Flow characterization . . . 36

6 Reduction of governing flow parameters **37**
6.1 Importance of the Froude number . . . 38
6.1.1 Simulations testing Fr . . . 38

7 DSG-relevant simulations **39**
7.1 Abengoa parameters . . . 39
7.2 Description of performed simulations . . . 40
7.3 Effect of varying void fraction . . . 41
7.4 Effect of increasing Reynolds number . . . 42
7.5 First-order statistics . . . 42
7.5.1 Liquid volume fraction . . . 42
7.5.2 Velocity profiles . . . 42
7.5.3 Film height and dry-out . . . 44
7.6 Second-order statistics . . . 45
7.7 Film sustainment . . . 46
7.7.1 Mechanisms discussed in the literature . . . 46
7.7.2 Secondary gas flow . . . 47
7.7.3 Wave pumping . . . 47
7.7.4 Droplet entrainment and deposition . . . 48

8 Conclusion **52**
8.1 Summary of literature findings . . . 53
8.2 Summary of numerical approach . . . 53
8.3 Summary of results . . . 54
8.4 Limitations and future work . . . 54

9 References **56**

A Opportunities for future collaboration **60**
A.1 Questions from Abengoa Solar . . . 60
A.2 Discussion . . . 61
A.2.1 Limitations from heat and mass transfer . . . 61
A.2.2 Proposal for a wall/film LES model . . . 61
A.3 Work plan and deliverables . . . 62
A.4 Opportunity . . . 64

B Boundary layer simulation **65**
B.1 Motivation . . . 65
B.2 Computational domain . . . 65
B.3 Results . . . 66

1 Introduction

1.1 Background

Direct Steam Generation (DSG) is a subset of the Concentrating Solar Power (CSP) initiative that seeks to use solar heating to evaporate water into steam for industrial applications. This is achieved by flowing water through pipes that are located at the foci of a field of parabolic solar reflectors. Abengoa Solar is an innovation company that, as stated on its website, "develops and applies technologies to generate electricity from the sun, working to limit climate change and to develop local communities using mostly concentrating solar thermal, but also photovoltaic technologies." As such a company, DSG is one of Abengoa's solar-thermal undertakings. Figure 1, taken from the Abengoa gallery, shows an Abengoa field of solar reflectors. The renewable approach of direct steam generation is very favorable to its conventional counterpart that uses fossil fuels as a heat source in typical thermal power stations. Much effort is being put forth by researchers such as those at Abengoa to increase the viability of direct steam generation.

Figure 1: A field of Abengoa Solar reflective parabolas for the purpose of DSG.

1.2 Objective

A complex multiphysics problem such as DSG is difficult to approach in its entirety. It is often more productive to first reduce the complexity by focusing on a sub-problem. One sub-problem that is the concern of the current project is to understand what is going on inside the tubing that is carrying the working fluid. Figure 2, taken from the Abengoa gallery, shows a close up of the tubing that is the concern of the current project. Understanding the thermal and fluid dynamics of the system are essential for designing optimized and efficient loops that maximize energy production and minimize cost. Obtaining this understanding requires much effort as the system is comprised of many complications, such as the presence of two phases, non-uniform and unsteady solar heating, pipe interactions, etc. As the working fluid is the medium by which heat is removed from the tubing, knowledge of the hydrodynamic and thermal properties could be useful in preventing damage of operating equipment. The objective of this project is to increase understanding of the physical processes of DSG from first principles, meaning to provide understanding of the system that goes

beyond experimental correlations and that can be used for more informed physical models.

Figure 2: An image showing the tubing that carries fluid through the field of Abengoa Solar reflective parabolas.

1.3 Challenges and opportunities

Many challenges are associated with understanding the thermofluid dynamics of the DSG process. Experiments can be difficult to perform, as properly instrumenting the flow can be hard to do in the industrial settings that such flows are directed towards. Even the fundamental task of visualizing the flow in this setting can be difficult. Most of the relevant experiments that have been performed to date provide data in the form of rough experimental correlations that vary widely from one experiment to the next: very little experimentation has been done to shed any light on the theoretical understanding of DSG-relevant flows.

In light of the experimental difficulties briefly mentioned above, using computational models to study DSG-relevant flows may shed light on the physics of these flows; provided the necessary tools are available. Not until recently have those tools become available: the state-of-the-art code NGA [1] has many unique capabilities that make it ideal for studying the current problem numerically. One of the basic pieces of information that NGA has the ability to predict is the interfacial distribution between the gas and liquid inside the tube. The relative location of the phases has large impacts on the hydrodynamic and thermal properties of the overall system. While studying the problem numerically requires us to isolate a small region of the system, make simplifying assumptions, and study a reduced version of the overall tubing, it has the potential to provide fundamental understanding of the relevant physical processes.

At the beginning of the year-long project, a broad range of tasks and objectives were discussed for the purpose of project direction. As the project progressed and results began to materialize, these objectives were refined in-line with what was shown to be feasible on the basis of numerical and theoretical study. The simulations performed in the past year are one-of-a-kind in both the physical system they resemble and their size. Although the largest Reynolds numbers simulated

are still far from those of the actual system, they are large enough to capture many of the relevant physical processes and provide a wealth of fundamental information that until this point has not been studied in a theoretical or numerical setting.

1.4 Overview of this report

The final report seeks to summarize what has been achieved over the past year of the CU-Abengoa collaboration for first-principle-based modeling of direct steam generation. The first task of the project was to survey the literature, and those findings are included here. The numerical techniques used to approach this problem are described, followed by a description of how our simulations fit into the big picture of DSG. Preliminary simulations were performed in order to ensure proper behavior of the code, they are summarized next. Theoretical and numerical work with direct relevance to DSG is then presented. Lastly, statistics obtained from simulations and mechanisms for film sustainment are discussed, followed by a brief description of future work.

2 Literature findings

Many processes found in industry involve the presence of multiphase flows. More specifically, two-phase flows are present in applications such as chemical and nuclear reactors, pipelines and oil wells, and solar collectors. As is evident in the expression, "two-phase flow" refers to the combined flow of either a gas and a solid, a gas and a liquid, a liquid and a solid, or two different liquids. Of these four possibilities, the gas-liquid flow is the most complicated in light of the deformability of the phases and the compressibility of one, if not both, of the phases. The common goal of studying gas-liquid flows is to understand the thermal and hydrodynamic properties of the flow, which are highly dependent on the interfacial distribution and interaction between the two phases. However, understanding the deformable distribution between two different phases in relative motion is a highly complex problem that has been the subject of much research in the past few decades. Understanding the heat transfer that is impacted by the complex gas-liquid distribution is essential to many industrial applications as it relates to optimized operation and economical design.

Direct Steam Generation (DSG) involves two-phase gas-liquid flow in the form of liquid and vapor water coflowing through horizontal round pipes. This literature survey will focus on two-phase gas-liquid flows through horizontal pipes, in effort to focus on the scenario relevant to DSG. A discussion of the different observed flow patterns will be presented first, as the interfacial distribution is crucial to hydrodynamic and thermal properties of the flow (i.e. pressure drop and heat transfer). A summary of much of the relevant experimental and numerical work that has been done will be provided, including a discussion of flow pattern maps as well as heat transfer and pressure drop correlations. After reviewing the experimental work available in the literature, possible reference experiments will be discussed for the purpose of code validation. The governing flow parameters will be discussed for the DSG regime, and this regime will be localized on certain flow pattern maps.

2.1 Observed flow regimes

The primary flow patterns that arise for gas-liquid flow in horizontal pipes are depicted in Fig. 3. The main difference between horizontal and vertical flow regimes is the tendency for stratification to occur: due to buoyancy the vapor migrates towards the top of the pipe while liquid occupies the

lower portion. When the quality is very low (the quality $x = \dot{m}_v/(\dot{m}_v + \dot{m}_l)$ is the ratio of mass flow rate of vapor to the total mass flow rate), a *bubbly flow* is characteristically observed. Small bubbles begin to coalesce as the quality is increased, forming larger bubbles. These larger bubbles flow in the upper region of

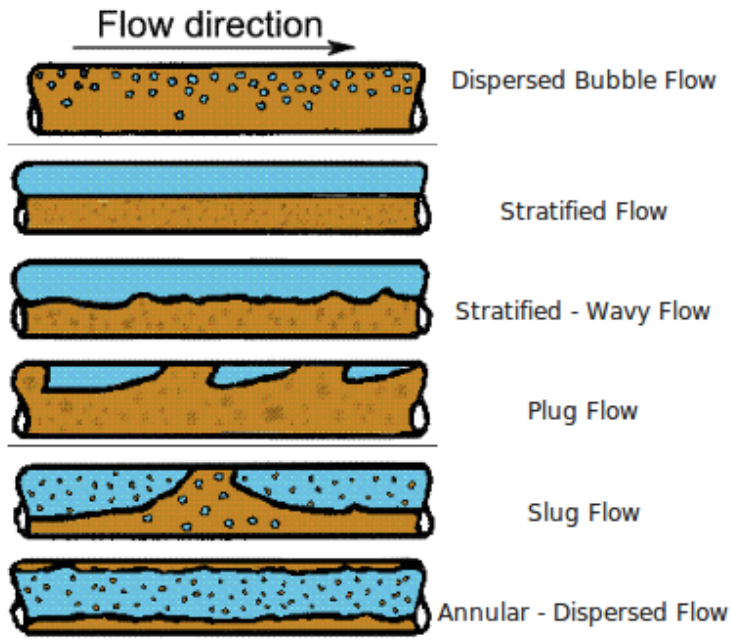

Figure 3: Observed flow patterns for two-phase gas-liquid flow in horizontal round pipes.

the pipe and characterize an intermittent regime known as *plug flow*. If the quality is relatively high while relatively low flow rates are maintained, the vapor and liquid phases separate and *stratified flow* occurs. Kelvin-Helmholtz instability can occur in the stratified regime if the flow rate or quality is increased, triggering the interface between the phases to become wavy: this regime is known as *wavy* or *stratified-wavy flow*. The amplitude of the waves in wavy flow may increase if the liquid flow rate is increased, to the point where they reach the top of the pipe. This pattern has a "sluglike" appearance and is thus referred to as *slug flow*. For the case of high quality and relatively high vapor velocities, the liquid assumes the annular form of a thin film around the interior surface of the pipe while a vapor core flows through the center of the pipe, known as *annular flow*. Depending on the relative dominance of stratification or advection, buoyancy effects may cause the film to be thinner near the top of the pipe than the bottom. Shear caused by the vapor core also has a tendency to entrain liquid droplets, as may be the case for wavy flow as well.

In the presence of vaporization, the quality is changing and the flow regime can change along the pipe length. The typically observed sequence of patterns for a vaporizing flow, starting from a single liquid, is first *bubbly* to *plug* to *slug* to *wavy* to *annular*. If vaporization continues past the annular regime, the flow can go from *dispersed mist flow* to *single-phase vapor flow*. This regime can cause damage to the pipe as dry-out is prone to occur (as is also possible in earlier high-quality regimes).

In discussing the above observed flow patterns for gas-liquid flow in horizontal pipes, it is important to realize that the lines which separate one regime from another are not clear. It can be difficult to visually assign a particular flow pattern to a particular regime, as transitional forms of these regimes are common. In the past half-century much work has gone into characterizing different flow patterns that arise in gas-liquid pipe flows and developing flow pattern maps in order to predict flow regimes based on important governing parameters. The experimental development of such flow pattern maps, as well as numerical validation and testing, is the topic of the next section.

2.2 Experimental and numerical work

Many experiments have been conducted in an effort to create flow pattern maps that generalize the previously mentioned regimes into specific categories. Towards the midpoint of the twentieth century, Kosterin [2], Alves [3], Baker [4], Krasiakova [5] and Hoogendoorn [6] were some of the first to propose maps for the prediction of flow patterns based on parameters such as superficial velocities and superficial Reynolds numbers of the gas and liquid (to be defined below), and mass flux ratios of the gas and liquid. Formulation of theories to predict transitions between certain regimes (i.e. stratified to annular [7]) has also been of interest.

As the types of problems that can be solved computationally continue to increase in size and complexity, numerical methods contribute more and more to problems involving a wide range of scales and non-uniformly varying properties, such as spray atomization and a variety of other flows involving multiple phases. In recent years numerical methods have been developed that are aimed towards dealing with multiphase flows in general [8, 9, 10], as well as simulations pertaining directly to the development of slug flow using a two-fluid model [11], three-phase slug flow using a multi-fluid model [12], bubble entrainment in slug flow [13] and two-phase annular flow [14].

2.3 Flow pattern maps

Of the many flow pattern maps proposed in the literature, the most notable are probably those of Baker [4], Mandhane [15], and Taitel and Dukler [16]. The latter two will be discussed here. In order to understand the abscissa and ordinate of these flow pattern maps, some fundamentals for gas-liquid pipe flow must be discussed. Defining the total mass flow rate as the sum of the vapor mass flow rate and liquid mass flow rate

$$\dot{m} = \dot{m}_v + \dot{m}_l \,, \tag{1}$$

the quality of the saturated mixture is defined as the ratio of vapor flow rate to total mass flow rate (as mentioned earlier):

$$x = \frac{\dot{m}_v}{\dot{m}} \,. \tag{2}$$

For a pipe with cross sectional area A, it is typical to define a "mass velocity"

$$G = \frac{\dot{m}}{A} \,, \tag{3}$$

which aids in the definition of superficial vapor and liquid velocities j_v and j_l, respectively:

$$j_v = \frac{Gx}{\rho_v} \tag{4}$$

$$j_l = \frac{G(1-x)}{\rho_l}\,, \tag{5}$$

where ρ_v and ρ_l are the densities of the vapor and liquid, respectively. These superficial velocities are numerically equivalent to the velocity that each phase would have were it flowing through the pipe alone at its specific mass flow rate. Thus, despite having units of velocity, they can also be thought of as the volume flux through the pipe of the respective phases. The flow pattern map of Mandhane [15] (Fig. 4(a)) uses the superficial gas velocity for the abscissa and the superficial liquid velocity as the ordinate to predict the interfacial distribution of the two-phase flow.

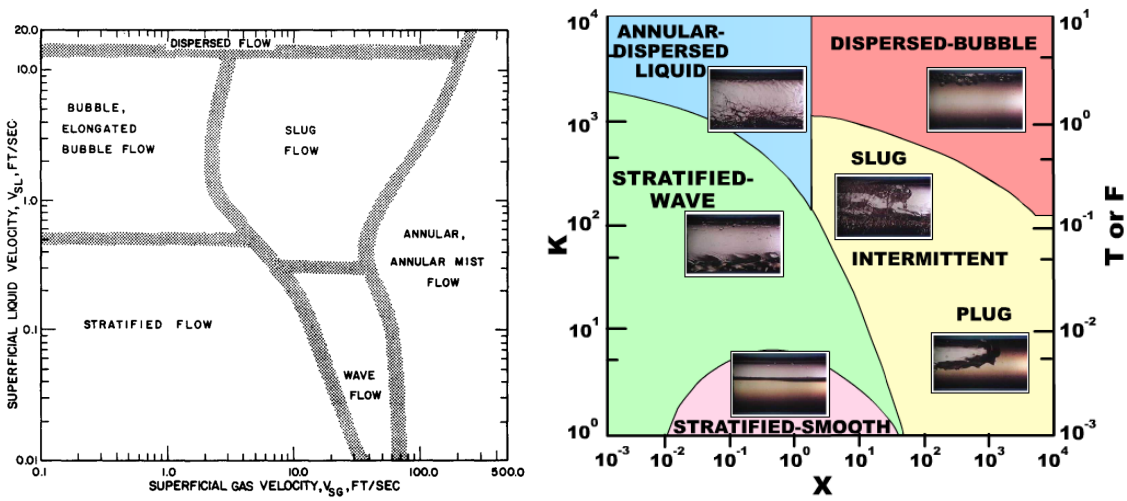

(a) Flow regime map of Mandhane [15].

(b) Flow regime map of Taitel and Dukler [16], taken from [17].

Figure 4: Two flow regime maps for gas-liquid flow in horizontal pipes.

The map that has the strongest theoretical basis is that of Taitel and Dukler [16] (Fig. 5(b)), and this map is the one that will be primarily discussed in this review for the purposes of DSG. To explain its coordinates, we can define superficial Reynolds numbers for the vapor and liquid, based on their superficial velocities:

$$\mathrm{Re}_v = \frac{\rho_v j_v D}{\mu_v} = \frac{GxD}{\mu_v} \tag{6}$$

$$\mathrm{Re}_l = \frac{\rho_l j_l D}{\mu_l} = \frac{G(1-x)D}{\mu_l}\,, \tag{7}$$

where D is the pipe diameter and μ_v and μ_l are the vapor and liquid dynamic viscosities, respectively. The abscissa of Fig. 5(b) is the dimensionless Martinelli factor, defined as

$$X = \sqrt{\frac{(dP/dz)_l}{(dP/dz)_v}}\,. \tag{8}$$

$(dP/dz)_l$ and $(dP/dz)_v$ are the frictional pressure gradients for the liquid and vapor phases flowing alone in the pipe. According to the formulation of Carey [18], these pressure gradients can be computed as

$$\left(\frac{dP}{dz}\right)_l = -\frac{2 f_l G^2 (1-x)^2}{\rho_l D} \tag{9}$$

$$\left(\frac{dP}{dz}\right)_v = -\frac{2 f_v G^2 x^2}{\rho_v D} \tag{10}$$

where the factors f_l and f_v are defined as

$$f_l = B\,\mathrm{Re}_l^{-n} \tag{11}$$

$$f_v = B\,\mathrm{Re}_v^{-n}\,. \tag{12}$$

If either Re_l or $\mathrm{Re}_v < 2000$ ("laminar" flow), the constants B and n are taken as $B = 16$ and $n = 1$; the constants are taken as $B = 0.079$ and $n = 0.25$ for Re_l or $\mathrm{Re}_v \geq 2000$ (turbulent flow).

The ordinate of Fig. 5(b) is either K, F or T (all dimensionless) depending on the transition being considered. If the transition being considered is stratified to wavy, then K is used:

$$K = \sqrt{\frac{\rho_v j_v^2 j_l}{\nu_l(\rho_l - \rho_v) g}}\,, \tag{13}$$

where ν_l is the kinematic viscosity of the liquid and g is gravity. If the transition considered is wavy-annular or wavy-intermittent (plug flow and slug flow) then the parameter

$$F = \sqrt{\frac{\rho_v j_v^2}{(\rho_l - \rho_v) D g}} \tag{14}$$

is used. The bubbly flow to intermittent flow transition uses the parameter

$$T = \sqrt{\frac{-(dP/dz)_l}{(\rho_l - \rho_v) g}}\,. \tag{15}$$

2.4 Heat transfer and pressure drop correlations

As many industrial applications require information involving pressure drop and heat transfer for multiphase flows through pipes, work regarding this dating back to the middle of the twentieth century is available in the literature [19, 20]. The first to model two-phase friction pressure drop were Lockhart and Martinelli [19], and they defined the pressure gradients of the liquid and gas flowing alone in the pipe (used in the formulation of the Martinelli factor equation (8)) as

$$\left(\frac{dp}{dz}\right)_l = \frac{1}{2}\frac{(\alpha_l \rho_l j_l)^2 \lambda_l}{\rho_l D} \tag{16}$$

$$\left(\frac{dp}{dz}\right)_g = \frac{1}{2}\frac{(\alpha_g \rho_g j_g)^2 \lambda_g}{\rho_g D}\,, \tag{17}$$

where α_i is the volume fraction and λ_i is the friction pressure loss coefficient of either the gas ($i = g$) or the liquid ($i = l$), respectively. The friction pressure loss coefficient for either species

is a function of both the volume fraction times the superficial Reynolds number and the surface roughness factor k/D:

$$\lambda_i = \lambda_i \left(\mathrm{Re}_i = \alpha_i \frac{\rho_i j_i D}{\mu_i}, \frac{k}{D} \right) .$$

2.4.1 Discussion of two-phase pressure drop

The Martinelli factor X in equation (8) is used to locate the x position on the Taitel and Dukler [16] flow pattern map of Fig. 5(b), but the issue of calculating the actual pressure drop within the pipe remains. Carey [18] offers an analytical expression for the two-phase pressure drop in a gas-liquid flow, valid for the regimes discussed above. As is common for general predictions of pressure drop within pipes, the derivation model assumes a steady, one-dimensional flow within the pipe (full derivations for three-dimensional, time-varying two-phase flow are given by Ishii [21] and Boure [22]). This one-dimensional assumption means that all dependent variables are constant at a given cross section of the pipe and vary in the axial direction only. The expression for pressure drop is derived from conservation of mass within the pipe combined with a force-momentum balance in the axial direction on both the vapor and liquid phases, and the emerging relation for pressure drop is

$$-\left(\frac{dP}{dz}\right) = -\left(\frac{dP}{dz}\right)_{fr} + \left[(1-\alpha_g)\rho_l + \alpha_g \rho_v\right] g \sin\Omega + \frac{d}{dz}\left\{ \frac{G^2 x^2}{\rho_v \alpha_g} + \frac{G^2 (1-x)^2}{\rho_l (1-\alpha_g)} \right\} . \tag{18}$$

In equation (18), α_g is the void fraction defined as the the ratio of area occupied by vapor to the total cross sectional area

$$\alpha_g = \frac{A_v}{A} , \tag{19}$$

and Ω is the angle of inclination of the pipe. In this relation, the total two-phase pressure drop can be decomposed into three contributions: frictional head effects (first term), gravitational head effects (second term) and acceleration or deceleration of the flow (third term). Note that for a horizontal pipe, the second term on the RHS is zero ($\sin(\Omega = 0) = 0$). Also, if there is no vaporization (or condensation) occurring then α and x are constant and the third term is zero. Relations derived from simplified theories or empirical correlations are available for the evaluation of α and $(dP/dz)_{fr}$.

If we assume that the two phases are in thermodynamic equilibrium and that the actual phase velocities

$$u_v = \frac{Gx}{\rho_v \alpha_g} \quad \text{and} \tag{20}$$

$$u_l = \frac{G(1-x)}{\rho_l (1-\alpha_g)} \tag{21}$$

are uniform over the area they occupy (A_v and A_l, respectively), but are not necessarily equal to

each other, then the two-phase multipliers

$$\phi_l = \sqrt{\frac{(dP/dz)_{fr}}{(dP/dz)_l}}\,, \tag{22}$$

$$\phi_{lo} = \sqrt{\frac{(dP/dz)_{fr}}{(dP/dz)_{lo}}}\,, \text{ and} \tag{23}$$

$$\phi_v = \sqrt{\frac{(dP/dz)_{fr}}{(dP/dz)_v}} \tag{24}$$

can be evaluated from the local flow conditions [19]. The subscripts l and v in equations (22) & (24) denote pressure gradients if the liquid or vapor flowed alone in the pipe with a mass flow rate of $G(1-x)A$ or GxA, respectively (as in equation (8)). The subscript lo in equation (23) denotes the pressure gradient that would result if liquid flowed alone in the pipe with the same total mass flow rate $\dot{m} = GA$.

Equations (22)-(24) can be solved for the frictional component of the total two-phase pressure drop in equation (18), expressing it in terms of any of the two-phase multipliers as

$$\left(\frac{dP}{dz}\right)_{fr} = \phi_i^2 \left(\frac{dP}{dz}\right)_i\,, \tag{25}$$

where $i = l$, lo or v. Substituting this relation into equation (18), we need closure for the terms ϕ_i^2, $(dP/dz)_i$ and α. The closure for these terms depends on the assumption of the nature of the two-phase flow, namely whether it can be approximated by the *homogeneous flow model* (often referred to as the *friction factor model* or the *fog flow model*) or must be treated as *separated flow* (for which the discussion of the above regimes applies). Closure for the homogeneous model is discussed below.

Homogeneous flow model

The central assumption of the homogeneous flow model is that the vapor and liquid phases have the same velocities and that the two-phase flow behaves as a single phase with fluid properties that are the average of the phase properties. This model is only valid for limited circumstances and may yield reasonably accurate results near the critical point when the vapor and liquid properties differ by a negligible amount, or when the slip velocity between the phases is small; such as in bubbly flow or mist flow.

The determination of α is straightforward: equating the phase velocities in equations (20) & (21) leads to the relation

$$\alpha_g = \frac{x/\rho_v}{[(1-x)/\rho_l] + (x/\rho_v)} = \frac{xv_v}{(1-x)v_l + xv_v}\,, \tag{26}$$

where v_i is the specific volume of species i (the inverse of ρ_i). Because we are assuming the two-phase flow to behave as an equivalent single-phase flow, we can evaluate $-(dP/dz)_{lo}$ and $-(dP/dz)_{fr}$ by a conventional Fanning friction factor f_{lo} and an effective friction factor f_{tp}:

$$-\left(\frac{dP}{dz}\right)_{lo} = \frac{2f_{lo}G^2}{\rho_l D} \tag{27}$$

$$-\left(\frac{dP}{dz}\right)_{tp} = \frac{2f_{tp}G^2}{\bar{\rho} D}\,, \tag{28}$$

where $\bar{\rho}$ is the mean flow density defined as

$$\frac{1}{\bar{\rho}} = \frac{x}{\rho_v} + \frac{1-x}{\rho_l} = v_v x + (1-x)v_l = \bar{v}\,. \tag{29}$$

Note that equation (27) is essentially equation (9) with a quality of zero. Friction factors are typically expressed as power-law functions of Reynolds number. Assuming the relations

$$f_{lo} = M\,\mathrm{Re}_{lo}^{-m} = M\left(\frac{GD}{\mu_l}\right)^{-m} \quad \text{and} \tag{30}$$

$$f_{tp} = N\,\mathrm{Re}_{tp}^{-n} = N\left(\frac{GD}{\bar{\mu}}\right)^{-n} \tag{31}$$

for f_{tp} and f_{lo}, plugging equations (27) & (28) into equation (23) yields

$$\phi_{lo}^2 = \left(\frac{N}{M}\right)\left(\frac{GD}{\mu_l}\right)^{m-n}\left(\frac{\bar{\mu}}{\mu_l}\right)^{n}\left\{1+\left(\frac{\rho_l}{\rho_v}-1\right)x\right\}\,. \tag{32}$$

The constants M, N, m and n are evaluated in the same way as B and n in equations (11) & (12). The mean flow viscosity $\bar{\mu}$ can be evaluated similarly to the mean flow density (as suggested by McAdams et al. [23]):

$$\frac{1}{\bar{\mu}} = \frac{x}{\mu_v} + \frac{1-x}{\mu_l}\,. \tag{33}$$

If the two-phase flow is turbulent while the corresponding liquid-only flow is laminar, then it makes sense to differentiate between f_{lo} and f_{tp}. If both flows are turbulent (as is often the case), then $M = N = 0.079$ and $m = n = 0.25$ and the dependence of the two-phase factor on G is eliminated, reducing equation (32) to

$$\phi_{lo}^2 = \left(\frac{\bar{\mu}}{\mu_l}\right)^{1/4}\left\{1+\left(\frac{\rho_l}{\rho_v}-1\right)x\right\}\,. \tag{34}$$

Using equation (33) into equation (34) and the relation (26) for the void fraction in the acceleration term of equation (18), we use the chain rule to differentiate out and simplify expression (18) (see Carey [18] for details). The two-phase pressure drop, under the assumptions listed for the homogeneous model, becomes

$$-\left(\frac{dP}{dz}\right) = \left[\phi_{lo}^2\left(\frac{2f_{lo}G^2v_l}{D}\right) + G^2 v_{lv}\left(\frac{dx}{dz}\right) + \frac{g\sin\Omega}{v_l + v_{lv}x}\right]\Bigg/\left[1 + G^2 x\frac{dv_v}{dP}\right]\,. \tag{35}$$

Separated flow

For the more general case of separated flow when the assumption of homogeneous flow is not made, the solution for the two-phase pressure drop provided by equation (18) is treated differently. Using the two-phase multiplier ϕ_l given in equation (22), the pressure drop of the liquid phase alone $(dP/dz)_l$ is given by equations (9) & (11). Applying the chain rule directly to the acceleration term in equation (18), plugging in for $(dP/dz)_l$ and solving for the two-phase pressure drop yields

$$\begin{aligned} -\left(\frac{dP}{dz}\right) &= \frac{1}{\Lambda}\Bigg(\phi_l^2\left[\frac{2f_lG^2(1-x)^2}{\rho_l D}\right] + \left[(1-\alpha_g)\rho_l + \alpha_g\rho_v\right]g\sin\Omega \\ &\quad + G^2\frac{dx}{dz}\left\{\left[\frac{2xv_v}{\alpha_g} - \frac{2(1-x)v_l}{1-\alpha_g}\right]\right\}\Bigg)\,, \end{aligned} \tag{36}$$

where

$$\Lambda = 1 + G^2 \left\{ \frac{x^2}{\alpha_g} \left(\frac{dv_v}{dP} \right) + \frac{d\alpha_g}{dP} \left[\frac{(1-x)^2 v_l}{(1-\alpha_g)^2} - \frac{x^2 v_v}{\alpha_g^2} \right] \right\} . \tag{37}$$

As was the case for the homogeneous flow model, the two-phase pressure drop can also be expressed in terms of ϕ_{lo} or ϕ_v [18].

For equation (36) to be useful, we need to know the void fraction α and the two-phase multiplier ϕ_l. Based off of the work of Lockhart and Martinelli [19] on adiabatic gas-liquid flows, Chisholm and Laird [24] formulated what is known as the Lockhart and Martinelli correlation (only shown for ϕ_l here):

$$\phi_l = \sqrt{1 + \frac{C}{X} + \frac{1}{X^2}} , \tag{38}$$

where C depends on the superficial Reynolds numbers of the liquid and vapor phases. The liquid flow is considered laminar if $\mathrm{Re}_l \leq 2000$ and turbulent if $\mathrm{Re}_l > 2000$, and the transition for the gas flow is taken to be at $\mathrm{Re}_v = 2000$ as well. The value of C changes based on the combinations of Re_l and Re_v and Table 1 summarizes the values used in the literature.

Table 1: Summary of values for C in correlation (38).

liquid	gas	subscript	C
turbulent	turbulent	tt	20
viscous	turbulent	vt	12
turbulent	viscous	tv	10
viscous	viscous	vv	5

Similar to the two-phase multiplier, the void fraction α was also correlated to the Martinelli factor by Lockhart and Martinelli [19]. The correlation, which was also confirmed by Butterworth [25], is expressed as

$$\alpha_g = \left(1 + 0.28 X^{0.71}\right)^{-1} . \tag{39}$$

A correlation to predict two-phase pressure drop for boiling flows was also developed by Martinelli and Nelson [26]. Assuming that the phases are in thermodynamic equilibrium and that the two-phase flow corresponds to the turbulent-turbulent case for flow boiling, they developed a correlation for the turbulent-turbulent two-phase multiplier $(\phi_l)_{tt}$ and void fraction α as a function of pressure and the parameter χ_{tt}, defined as

$$\chi_{tt} = \left(\frac{\rho_v}{\rho_l} \right)^{0.571} \left(\frac{\mu_l}{\mu_v} \right)^{0.143} \left(\frac{1-x}{x} \right) . \tag{40}$$

If we plug in the appropriate constants for the turbulent-turbulent case, we see that this only differs slightly from the turbulent-turbulent Martinelli factor, which comes out to be

$$X_{tt} = \left(\frac{\rho_v}{\rho_l} \right)^{0.5} \left(\frac{\mu_l}{\mu_v} \right)^{0.125} \left(\frac{1-x}{x} \right)^{0.875} . \tag{41}$$

These two factors are quite similar, and based on its strong theoretical basis and relative simplicity, the Lockhart-Martinelli formulation discussed above is recommended for adiabatic conditions or

flow boiling conditions with low heat flux. The correlations of Baroczy [27] may be explored as well.

The correlations discussed explicitly above are in some sense the baseline correlations that have laid the foundation for pressure drop correlations of two-phase gas-liquid flows in general. There are many other pressure drop correlations that are used in more specific scenarios. Some of the work done in DSG modeling thus far (i.e. Eck [28]) has relied on the correlations of Friedel [29], which included a database of 25,000 points to develop a correlation for the two-phase multiplier ϕ_{lo}. Pressure drop data for DSG can be found in the works of Natan et al. [30] and Pye et al. [31]. Many other pressure drop correlations are available, and the selection of the best one seems to depend primarily on the flow regime being considered, as well as other factors (see Spedding et al. [32] for a more detailed description of various correlations).

2.4.2 A note on annular flow

Annular flow is a regime commonly seen due to higher qualities and velocities/flow rates. This regime is quite common in many engineering two-phase gas-liquid systems. Much of the available information pertaining to pressure drop comes specifically from annular flow experiments [33, 34]. Theoretical work has gone into understanding both the stability of annular flow [7] and bubble entrainment in annular flow [35, 36]. Rodriguez [14] performed a numerical simulation of the water-vapor annular experiment of Würtz [34], ranging from 30 bar to 90 bar. This simulation was done for a thirty degree wedge of pipe, using periodic conditions both axially and circumferentially. Radial velocity profiles were computed, extracting the law of the wall for the annular liquid film.

2.4.3 Discussion of two-phase heat transfer

Available experimental data and heat transfer correlations for gas-liquid two-phase flow in horizontal and vertical pipes can be found in a comprehensive discussion provided by Kim et al. [37]. Despite the many efforts, there is still no global treatment for predicting heat transfer in two-phase flows. For the case of non-boiling gas-liquid flow, a relatively recent series of experiments sought to develop and validate a general heat transfer correlation with different flow patterns, accounting for the effect of interfacial distribution by introducing a flow pattern factor (essentially an effective wetted-perimeter) [38, 39, 40, 41]. The correlation takes the form

$$h_{TP} = F_P h_L \left\{ 1 + C \left[\left(\frac{x}{1-x} \right)^m \left(\frac{1-F_P}{F_P} \right)^n \left(\frac{\mathrm{Pr}_G}{\mathrm{Pr}_L} \right)^p \left(\frac{\mu_G}{\mu_L} \right)^q \right] \right\} , \tag{42}$$

where h_{TP} is the overall mean two-phase heat transfer coefficient, F_P is the flow pattern factor, h_L is the the heat transfer coefficient as if only the liquid phase was flowing, x is the quality, Pr is the Prandtl number and μ is viscosity. The subscripts L and G are for the liquid and gas phases, respectively. The values of the coefficients C, m, n, p and q are given as 0.7, 0.08, 0.06, 0.03 and -0.14, respectively. The details of how well this correlation fit data within different regimes can be found in Kim and Ghajar [40].

More generally, the convective heat transfer coefficient h is correlated in terms of the turbulent-turbulent Martinelli factor, the liquid-only Reynolds number and the Prandtl number of the liquid

phase:

$$\frac{hD}{k_l} = f\left(X_{tt}, \mathrm{Re}_l, \mathrm{Pr}_l\right) , \tag{43}$$

where k_l is the thermal conductivity of the liquid. Variations of equation (43) have taken the form

$$\frac{h}{h_i} = f\left(\frac{1}{X_{tt}}\right) , \tag{44}$$

where the subscript i can be either l, designating the heat transfer coefficient for the liquid flowing alone, or lo, designating the heat transfer coefficient for the entire flow as a liquid (this notation is analogous to the two-phase multiplier ϕ_i). If the Blasius correlation for single-phase turbulent flow is used to express the friction factor, then the constants of equation (11) are $B = 0.04$ and $n = 0.2$. With these constants the turbulent-turbulent Martinelli factor comes out to be

$$X_{tt} = \left(\frac{1-x}{x}\right)^{0.9} \left(\frac{\rho_v}{\rho_l}\right)^{0.5} \left(\frac{\mu_l}{\mu_v}\right)^{0.1} . \tag{45}$$

This is the formulation of X_{tt} used by Kim and Ghajar [39].

Several correlations are available in the literature that express equation (44) in the form

$$\frac{h}{h_{lo}} = B\left(\frac{1}{X_{tt}}\right)^n , \tag{46}$$

where values of $B = 3.5$, $n = 0.5$ (see [42]) and $B = 3.4$, $n = 0.45$ (see [43]) have been used. In the case of DSG in parallel pipes, Natan et al. [30] used the formulation of Tong [44] to express the overall two-phase heat transfer coefficient h_{TP} as

$$\frac{h_{TP}}{h_{LP}} = B\left(\frac{1}{X_{tt}}\right)^n , \tag{47}$$

with $B = 2.17$, $n = 0.7$ and X_{tt} expressed as in equation (45). The liquid phase heat transfer coefficient is expressed as

$$h_{LP} = 0.023\,\frac{k_l}{D}\left[\frac{D\dot{m}(1-x)}{\mu_l}\right]^{0.8} \left(\frac{c_{PL}\mu_l}{k_l}\right)^{0.4} , \tag{48}$$

where x is the quality and c_{PL} is the specific heat of the liquid.

2.5 Possible reference experiments

Direct Numerical Simulation (DNS) of a two-phase gas-liquid flow inside a horizontal pipe is a central element in this project. A possible validation strategy involves reproducing some of the discussed flow patterns as the quality and velocities/mass flow rates of the phases are varied. Reynolds numbers based on the average two-phase flow property and the pipe diameter larger than around 10,000 (note this is the Reynolds number calculated from the assumption of the homogeneous flow model) are challenging to simulate directly and require modeling of the subgrid scales. Such models do not exist at this time. Table 2 lists the values of Reynolds numbers and Weber numbers expected for Abengoa DSG, based on the range of operating pressures and steam qualities shown.

Table 2: Re and We for a given quality x and operating pressure P predicted by the homogeneous flow model.

P [psig]	x [%]	Re	We
203.63	3.23	1.53×10^5	1.03×10^3
160.27	13.06	2.43×10^5	4.06×10^3
1249.79	10.04	5.74×10^5	6.06×10^3
1190.90	68.20	1.45×10^6	2.64×10^4

The lowest value of Re in Table 2 is much higher than the value of Re that is thought to be feasible for DNS. This means that we will need to pick a different experiment for our DNS code validation. Kim and Ghajar [39] offer a selection of experiments for which we could compare our DNS results with the flow patterns they observed based on their flow conditions. The work of Spedding and Spence [45] may also provide a good experimental test case for us to simulate. Another possibility for code validation is to reproduce the two-phase water-vapor experiment of Würtz [34] by following the methodology of Rodriguez [14]. This would also allow us to perform a detailed comparison of velocity profiles.

2.6 Localization of DSG on regime maps

As discussed earlier, there are many available flow pattern maps for two-phase gas-liquid flow in horizontal pipes. The most well-established in the literature seems to be the one proposed by Taitel and Dukler [16], shown in Fig. 5(b). Many other maps have been proposed, typically with superficial liquid and gas velocities or Reynolds numbers as the plotting coordinates. Fig. 5 demonstrates the likely flow patterns of DSG as predicted by the maps of Taitel and Dukler [16] and Ghajar and Tang [41]. The maps show the possible progression of the flow as the quality increases from 0.01 to

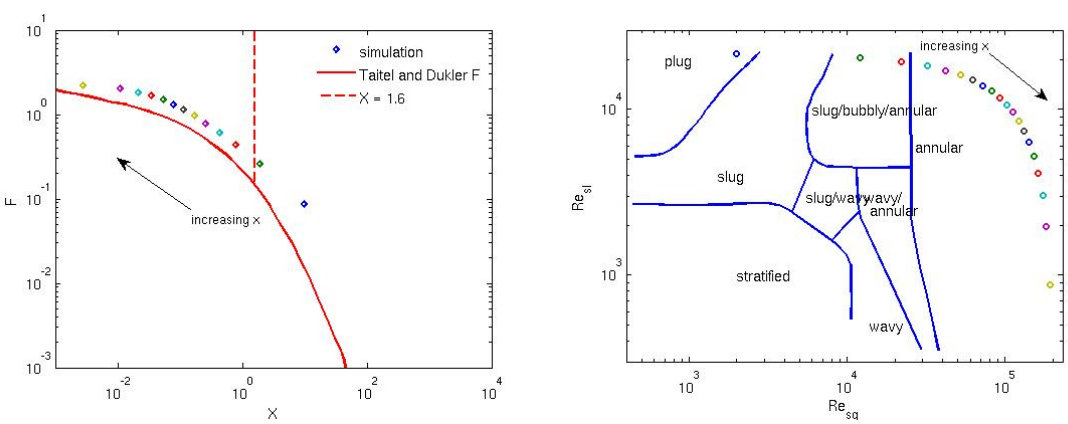

(a) DSG on the flow pattern map of Taitel and Dukler [16], using the wavy-annular or wavy-intermittent transition parameter.

(b) DSG on the flow pattern map of Ghajar and Tang [41].

Figure 5: Possible progression of flow pattern in DSG pipes as steam quality increases.

5 to 7 to 10%, at an example operating pressure of 50 psig. Although the maps are not in perfect agreement, they both seem to suggest a progression from an intermittent or wavy-annular type of regime to annular flow as the quality increases.

3 Computational approach

3.1 Mathematical formulation

The gas-liquid flow of interest can be described using the continuity and Navier-Stokes equations. Assuming that both phases are incompressible, i.e. , $\nabla \cdot \boldsymbol{u} = 0$, the continuity equation is written

$$\frac{D\rho}{Dt} = \frac{\partial \rho}{\partial t} + \boldsymbol{u} \cdot \nabla \rho = 0, \tag{49}$$

where $\boldsymbol{u}$ is the velocity field and ρ is the density. The Navier-Stokes equations are written

$$\frac{\partial \rho \boldsymbol{u}}{\partial t} + \nabla \cdot (\rho \boldsymbol{u} \otimes \boldsymbol{u}) = -\nabla p + \nabla \cdot \left(\mu \left[\nabla \boldsymbol{u} + \nabla \boldsymbol{u}^{\mathsf{T}} \right] \right) + \rho \boldsymbol{g}, \tag{50}$$

where p is the pressure, $\boldsymbol{g}$ is the gravitational acceleration, and μ is the dynamic viscosity.

The material properties are considered to be constant in each phase. The subscript l is used to describe the density and the viscosity in the liquid, respectively ρ_l and μ_l. Similarly, the subscript g corresponds to the density and the viscosity in the gas, respectively ρ_g and μ_g. It is convenient to introduce the jump of these quantities across the phase-interface Γ, defined by $[\rho]_\Gamma = \rho_l - \rho_g$ and $[\mu]_\Gamma = \mu_l - \mu_g$. In the absence of mass transfer between the two phases, the velocity field is continuous across Γ, i.e. , $[\boldsymbol{u}]_\Gamma = 0$. In contrast, the existence of surface tension forces will lead to a discontinuity in the normal stresses at the gas-liquid interface. This translates into a pressure jump that can be expressed as

$$[p]_\Gamma = \sigma \kappa + 2 \, [\mu]_\Gamma \, \boldsymbol{n}^{\mathsf{T}} \cdot \nabla \boldsymbol{u} \cdot \boldsymbol{n}, \tag{51}$$

where σ is the surface tension coefficient, κ is the curvature of the phase-interface, and $\boldsymbol{n}$ is the phase-interface normal.

3.2 Numerical methodology

The numerical methods used in this work are based on arbitrarily high-order accurate fully conservative finite difference schemes implemented in the NGA code [1]. These schemes are both robust and accurate, and are therefore ideally suited to the numerical simulation of turbulence. In this work, the second-order version of these schemes is used, since it greatly simplifies the implementation of the multiphase numerics.

Equation (51) highlights the need for a specific strategy regarding discontinuities. In this work, the discontinuities in density and pressure that arise in the pressure gradient term of equation (50) are treated using the ghost-fluid method (GFM) of Fedkiw *et al.* [46]. This approach provides a sharp and robust discretization of the discontinuities across the phase-interface. However, it presents specific challenges when considering the viscous term discontinuities, and for this reason this term is discretized using a height function strategy, as presented for example by Sussman *et al.* [47]. For more details on the numerical discretization for multiphase flow problems in NGA, the reader is referred to prior work [1, 48].

Two new developments have been introduced here, namely a quadrature-free discontinuous Galerkin conservative level set method for interface transport, and a novel discretization of the momentum convection term that allows for robust high density ratio simulations. These two methods are presented briefly below, along with numerical tests.

3.3 Discontinuous Galerkin Conservative Level Set

Turbulent primary atomization is a process that includes significant interface dynamics that result in a large quantity of small droplets. Hence, an interface scheme must combine excellent accuracy with excellent mass conservation properties in order to be successfully used to simulate primary atomization. We present here a novel methodology that is based on the Accurate Conservative Level Set (ACLS) technique [49], but relies on a quadrature-free discontinuous Galerkin discretization for improved accuracy [50]. This approach has the following properties: (1) it is very accurate since it uses a polynomial representation of the level set function to an arbitrarily high order in each cell, (2) it has excellent mass conservation properties since it uses only discretely conserving schemes, and (3) it has the smallest possible numerical stencil size, which leads to excellent parallel scalability.

3.3.1 Accurate Conservative Level Set approach

According to the level set methodology, the interface is defined implicitly as an iso-surface of a smooth function ψ, and is transported by solving

$$\frac{\partial \psi}{\partial t} + \nabla \cdot (\boldsymbol{u}\psi) = 0. \tag{52}$$

Note that since the velocity field is solenoidal, this equation implies that the phase-interface undergoes material transport, in accordance with equation (49). In ACLS [49], the level set function is defined as an hyperbolic tangent profile, written

$$\psi(\boldsymbol{x}, t) = \frac{1}{2}\left(\tanh\left(\frac{\phi(\boldsymbol{x}, t)}{2\varepsilon}\right) + 1\right), \tag{53}$$

where ε is a parameter that sets the thickness of the profile. We set ε to half the characteristic cell size in all simulations in this paper. In the previous equation, ϕ corresponds to a standard signed distance function, i.e. ,

$$|\phi(\boldsymbol{x}, t)| = |\boldsymbol{x} - \boldsymbol{x}_\Gamma|, \tag{54}$$

where $\boldsymbol{x}_\Gamma$ corresponds to the closest point on the interface from $\boldsymbol{x}$, and $\phi(\boldsymbol{x}, t) > 0$ on one side of the interface, and $\phi(\boldsymbol{x}, t) < 0$ on the other side. Finally, a reinitialization equation is introduced in order to preserve the hyperbolic tangent profile. This equation is written

$$\frac{\partial \psi}{\partial \tau} + \nabla \cdot (\psi(1-\psi)\boldsymbol{n}) = \nabla \cdot (\varepsilon(\nabla\psi \cdot \boldsymbol{n})\boldsymbol{n}), \tag{55}$$

and is solved in pseudo-time τ at each time-step. This approach is chosen because it combines the accuracy of level set methods with excellent conservation properties. The ACLS methodology, in particular its coupling with the GFM, is described in more details by Desjardins *et al.*[49].

3.3.2 Discontinuous Galerkin discretization

Discontinuous Galerkin (DG) schemes offer a variety of desirable properties when applied to the conservative level set method. DG allows for arbitrarily high order of accuracy without the necessity of a large stencil resulting in a robust, accurate, and highly scalable scheme. The novel discretization introduced here is presented in two parts: the first deals with the transport of the conservative level set, the second considers the reinitialization equation. The formulation for both equations is derived in a quadrature-free form, where all surface and volume integrals that appear in the derivation are computed *a priori* in order to reduce computational cost.

The hyperbolic tangent level set is conservatively transported with a quadrature-free DG strategy. The main idea of DG is to represent the level set function as a linear combination of basis functions ϕ_n, such as

$$\psi(\boldsymbol{x}, t) = \sum_{n=0}^{N} g_n(t)\phi_n(\boldsymbol{x}), \tag{56}$$

where $N+1$ is the number of degrees of freedom and ϕ_n is the basis function with associated weight g_n. Although almost any set of basis functions will work, Legendre polynomials have the beneficial property of being orthogonal to each other and are therefore used in this work. To obtain the quadrature-free DG version of the transport equation, we multiply equation (52) by each basis function, and integrate by parts over each computational cell, leading to

$$\begin{aligned} \frac{\partial g_n}{\partial t} \int_V \phi_n \phi_t dV - g_i u_j \int_V \frac{\partial \phi_t}{\partial x_j} \phi_i dV \\ + (u_j)_{\text{face}} (g_i)_{\text{up}} N_j \int_S (\phi_i)_{\text{up}} \phi_t dS = 0, \end{aligned} \tag{57}$$

using Einstein's summation notation and $(g_i)_{\text{up}}$ defined as the ith weight upwinded based on the velocity field. $(*)_{\text{face}}$ is defined as quantity $(*)$ interpolated to the face. It should be noted that an assumption of u_j being constant within each cell allows for it to be removed from the integral in the previous equation. This assumption is reasonable for us since we make use of a second order accurate velocity solver. In addition, the surface normal N_j is a constant for flat faces found in regular grids. Removing u_j and N_j from the integrals allows us to write the conservative transport equation in quadrature-free form, i.e. where all the integrals are only a function of the basis functions and not a function of time. As a result, they can be precomputed for a chosen set of basis functions, and then equation (57) can easily be updated without evaluating any integrals. Additionally, the equation uses only data from the cell of interest and the faces of neighboring cells. Such a small stencil leads to excellent parallelization properties. The resulting level set representation is illustrated in Fig. 6 for a circle resolved by 5 cells, using second order polynomials.

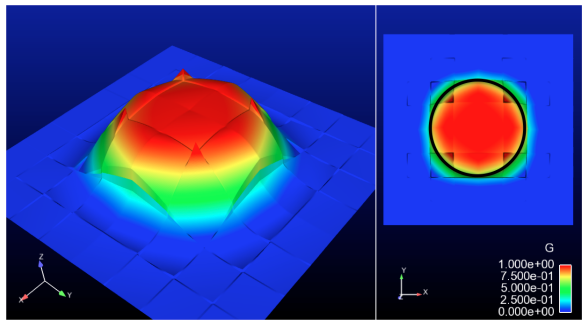

Figure 6: Discontinuous polynomial representation of the conservative level set field.

Reinitialization is used to maintain the thickness of the hyperbolic tangent profile and control mass loss. The reinitialization equation presented above, equation (55) is solved using DG applied in a similar fashion as described in the previous section. However, the reinitialization equation contains a diffusion term that requires special treatment, and is handled here following the ideas of Lou *et al.* [51]. This method involves constructing a function over the two cells that contain the face, i.e.

$$\boldsymbol{R} = \sum_{n=0}^{N} r_n \tilde{\phi}_n, \tag{58}$$

where $\tilde{\phi}_n$ is a scaled basis function that spans the two cells and r_n is the weight associated with the scaled basis function. The weights are calculated by imposing the following constraints in a least-squares sense,

$$\int_{V^-} g_i^- \phi_i \tilde{\phi}_t dV = \int_{V^-} r_i \tilde{\phi}_i \tilde{\phi}_t dV, \tag{59a}$$

$$\int_{V^+} g_i^+ \phi_i \tilde{\phi}_t dV = \int_{V^+} r_i \tilde{\phi}_i \tilde{\phi}_t dV. \tag{59b}$$

Using this approach a unique flux can be determined at each face. For brevity, the details of the derivation of the algorithm are omitted here, and only the final discretized quadrature-free equation is shown:

$$\begin{aligned}
\frac{\partial g_n}{\partial \tau} \int_V \phi_n \phi_t dV - g_i n_j \int_V \phi_i \frac{\partial \phi_t}{\partial x_j} dV \\
&+ (g_i)_{\text{up}} (n_j)_{\text{face}} N_j \int_S (\phi_i)_{\text{up}} \phi_t dS \\
&+ g_i g_k n_j \int_V \phi_i \phi_k \frac{\partial \phi_t}{\partial x_j} dV \\
&- (g_i g_k)_{\text{up}} (n_j)_{\text{face}} N_j \int_S (\phi_i \phi_k)_{\text{up}} \phi_t dS \\
= &- \varepsilon g_i n_j n_k \int_V \frac{\partial \phi_i}{\partial x_j} \frac{\partial \phi_t}{\partial x_k} dV \\
&+ \varepsilon r_i \left(n_j n_k\right)_{\text{face}} N_k \int_S \frac{\partial \tilde{\phi}_i}{\partial x_j} \phi_t dS.
\end{aligned} \tag{60}$$

3.3.3 Curvature computation

An accurate curvature scheme is key component of any level set approach. For pde-based level set schemes that rely on a signed distance function, curvature can typically be obtained easily using finite differencing to compute the divergence of the normal vector. However, because the proposed level set is a hyperbolic tangent function, it is significantly more curved in its normal direction than in its tangential directions, making finite differencing very inaccurate. This problem is similar to the challenge faced by volume of fluid (VOF) users, for which it has been shown that using a height function was an appropriate strategy [52]. As a consequence, a height function approach was implemented and tested. It consists of integrating the level set function in its normal direction in order to form a height, which is then fitted using a second order polynomial, leading to a curvature. The convergence of this approach is assessed on a circle discretized with an increasingly finer mesh. The L_∞ and L_2 norm of the curvature error are shown in Fig. 7, where it can be observed that the curvature converges with a rate between second and third order accuracy.

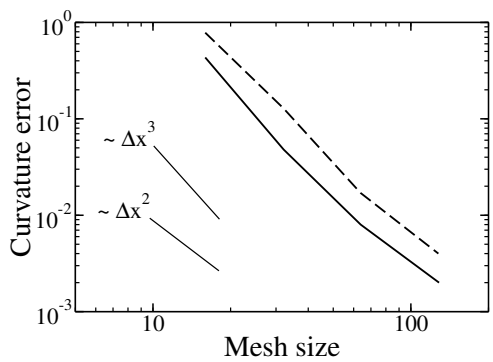

Figure 7: Convergence of the curvature error on a circle: L_∞ norm (dashed line) and L_2 norm (solid line).

3.3.4 Scalability

The DG conservative level set method relies on a fourth order Runge-Kutta temporal integration. Because of the combination of an explicit temporal integration scheme and a minimal stencil size, excellent scaling properties are obtained for this method, as illustrated in Fig. 14(a) for a Zalesak disk test case. This excellent scaling compliments the scaling of the NGA code, as shown in Fig. 14(b).

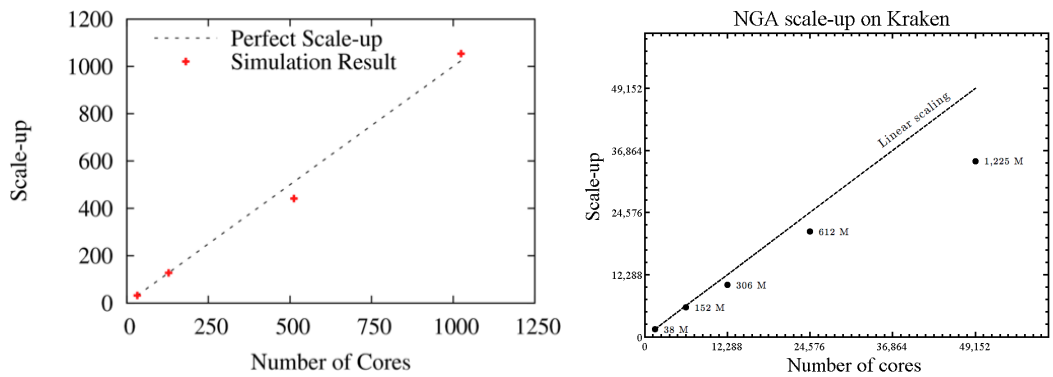

(a) Weak scaling test for level set transport and re-initialization.

(b) Weak scaling of the NGA code.

Figure 8: Scaling for the DG scheme and the NGA code.

3.4 High density ratio correction

Transport inconsistencies between density and velocity give rise to numerical difficulties, as spurious errors in momentum can appear, leading to spurious variations in kinetic energy. This problem is exacerbated by the presence of strong shear at the interface and high density ratios, and ultimately causes numerical stability issues. Note that it can affect both level set [53] and VOF methods [54], since these approaches rely on very specific strategies for transporting the phase-interface, which are likely to differ from the way momentum is convected. In the context of VOF, Rudman [55] suggested using VOF density fluxes when calculating the momentum convection term, thereby forcing a discrete compatibility between density and momentum transport. This strategy for dealing with high density ratio flows was then adapted to level set methods by Raessi [56] and Raessi & Pitsch [57], although their work was limited to one- and two-dimensional problems. In this work, we make use of a novel approach for extending this correction to level set methods. This new high-density scheme performs well regardless of the density ratio and shear rate, making it ideal for air-blast fuel injection problems.

The Navier-Stokes equations are advanced by solving

$$\frac{\boldsymbol{u}^{\star}_{k+1} - \boldsymbol{u}^{n}}{\Delta t} = P_k^{n+\frac{1}{2}} - C_{k+1}^{n+\frac{1}{2}} - V_{k+1}^{n+\frac{1}{2}}, \tag{61}$$

where

$$\begin{aligned} P_k^{n+\frac{1}{2}} &= -\frac{1}{\rho^{n+\frac{1}{2}}} \nabla p_k^{n+\frac{1}{2}}, \\ C_{k+1}^{n+\frac{1}{2}} &= \nabla \cdot \left(\boldsymbol{u}_{k+1}^{n+\frac{1}{2}} \otimes \boldsymbol{u}_{k+1}^{n+\frac{1}{2}} \right), \quad \text{and} \\ V_{k+1}^{n+\frac{1}{2}} &= \frac{1}{\rho^{n+\frac{1}{2}}} \nabla \cdot \left(\mu^{n+\frac{1}{2}} \left[\nabla \boldsymbol{u}_{k+1}^{n+\frac{1}{2}} + \nabla \boldsymbol{u}_{k+1}^{n+\frac{1}{2}} \Big|^{\mathsf{T}} \right] \right) \end{aligned}$$

are the pressure, convective, and viscous terms, respectively. In order to improve the coupling between momentum convection and level set transport, the convective term is re-cast in a form

that includes density, which will be carefully constructed from the level set. The new convection term is obtained by writing the discrete Navier-Stokes equation in terms of the momentum instead of the velocity, giving

$$\widehat{C}_{k+1}^{n+\frac{1}{2}} = \frac{1}{\hat{\rho}^{n+1}} \nabla \cdot \left(\hat{\rho}^{n+\frac{1}{2}} \boldsymbol{u}_{k+1}^{n+\frac{1}{2}} \otimes \boldsymbol{u}_{k+1}^{n+\frac{1}{2}} \right) + \frac{1}{\hat{\rho}^{n+1}} \frac{\hat{\rho}^{n+1} \boldsymbol{u}^n - \hat{\rho}^n \boldsymbol{u}^n}{\Delta t}. \tag{62}$$

In the previous expression, the density can vary by several orders of magnitude, which requires special attention. We start by writing

$$\hat{\rho}_i^n = \rho_g + [\rho]_\Gamma \, h \left(\phi_{i-\frac{1}{2}}^n, \phi_{i+\frac{1}{2}}^n \right), \tag{63}$$

where the height function h is defined by

$$h \left(\phi_{i-\frac{1}{2}}^n, \phi_{i+\frac{1}{2}}^n \right) = \begin{cases} 1 & \text{if } \phi_{i-\frac{1}{2}}^n \geq 0 \text{ and } \phi_{i+\frac{1}{2}}^n \geq 0 \\ 0 & \text{if } \phi_{i-\frac{1}{2}}^n < 0 \text{ and } \phi_{i+\frac{1}{2}}^n < 0 \\ \frac{\phi_{i-\frac{1}{2}}^{n+} + \phi_{i+\frac{1}{2}}^{n+}}{|\phi_{i-\frac{1}{2}}^n| + |\phi_{i+\frac{1}{2}}^n|} & \text{otherwise,} \end{cases} \tag{64}$$

where $a^+ = \max(a, 0)$. Next, $\hat{\rho}^{n+\frac{1}{2}} \boldsymbol{u}_{k+1}^{n+\frac{1}{2}}$ is treated as a density flux for the continuity equation, allowing us to perform simple upwinding, leading to

$$\hat{\rho}_{i+\frac{1}{2}}^{n+\frac{1}{2}} = \begin{cases} \hat{\rho}_i^n & \text{if } \left. \boldsymbol{u}_{k+1}^{n+\frac{1}{2}} \right|_{i+\frac{1}{2}} \geq 0 \\ \hat{\rho}_{i+1}^n & \text{otherwise.} \end{cases} \tag{65}$$

Finally, we obtain $\hat{\rho}^{n+1}$ using

$$\hat{\rho}^{n+1} = \hat{\rho}^n - \Delta t \nabla \cdot \left(\hat{\rho}^{n+\frac{1}{2}} \boldsymbol{u}_{k+1}^{n+\frac{1}{2}} \right). \tag{66}$$

This approach ensures a tight coupling between level set and momentum transport, since $\hat{\rho}^n$ is defined directly from the level set at each time-step. While this scheme is first-order in both space and time, more accurate schemes can readily be used provided they maintain the boundedness of $\hat{\rho}^{n+1}$. Finally, note that the extension to three dimensions is straightforward.

This momentum correction scheme is evaluated on a simple two-dimensional test case of droplet transport. A droplet of diameter D is placed in the middle of a periodic computational domain of size $5D \times 5D$. Various meshes are considered, ranging from 32^2 to 128^2. The velocity field is initialized by giving the liquid a velocity $u_l = 1$ and $v_l = 0$, while the gas is initially at rest. The time-step size is chosen such that the convective CFL remains below 0.2. Both gas and liquid viscosities, as well as the surface tension coefficient, are set to zero. Finally, the density ratio between the liquid and the gas is set to 10^6. Under these conditions, the droplet is expected to remain perfectly circular. However, the non-corrected scheme becomes unstable and fails in less than a third of a flow-through time regardless of the mesh refinement or time-step size. In

comparison, the density-corrected scheme runs robustly with all meshes for any number of flow-through times. Some deformation of the drop is visible, although it does not appear to increase significantly with time. Figure 9 shows the phase-interface after one flow-through time for the various meshes, compared to the exact solution. The drop shape converges satisfyingly toward the exact solution.

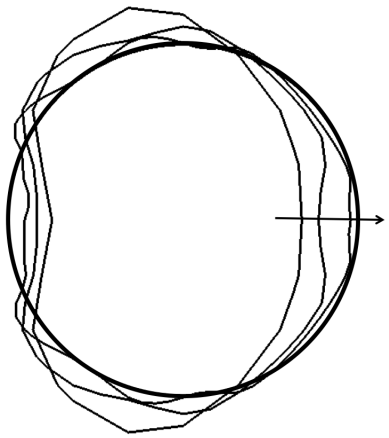

Figure 9: Droplet shape after one flow-through time using the density-based momentum flux correction scheme. The arrow indicates mesh size increasing from 32^2 to 64^2 to 128^2, and the thick line is the exact solution.

3.5 Simulation strategy

3.5.1 Level of resolution

The possible simulation approaches available are direct numerical simulation (DNS), in which all scales of the flow are fully resolved, large-eddy simulation (LES), in which the large-scale fluctuations are resolved and the small scales are modeled, and Reynolds-averaged Navier-Stokes (RANS), in which the governing equations are solved only for the mean values and all fluctuations are modeled (see Fig. 10(a) for a visual description of these approaches).

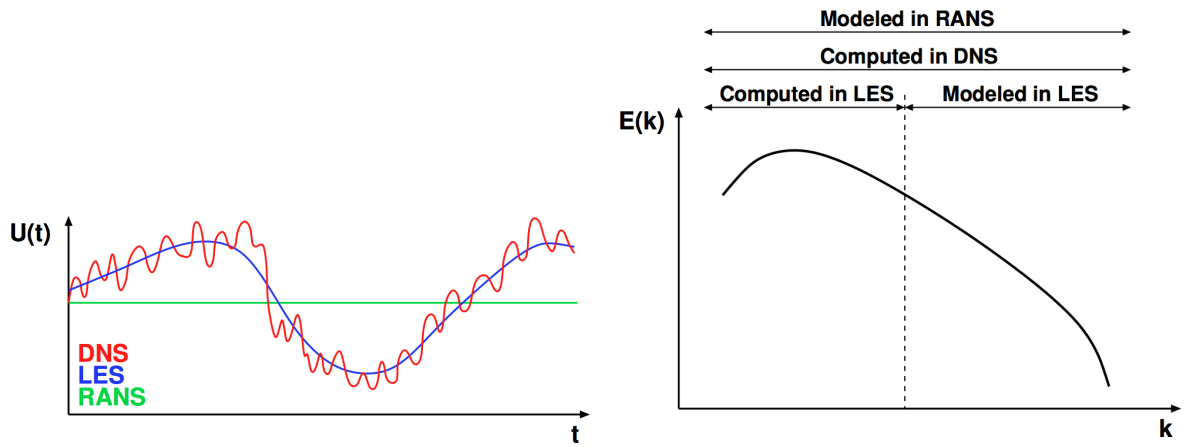

(a) Comparison between DNS, LES, and RANS in physical space.

(b) Comparison between DNS, LES, and RANS in spectral space.

Figure 10: Different approaches for simulating turbulence.

The cost of these methods decreases in the order they have been presented: DNS is the most costly and the most accurate while RANS is the cheapest and captures the least amount of physics. LES is of moderate cost and the accuracy of this approach lies somewhere between RANS and DNS, depending on how small of scales you choose to resolve (see Fig. 10(b)).

3.5.2 NGA

In previous projects, we extended high order fully conservative numerical algorithms to complex multiphase reacting turbulent flows [58, 59, 48], ultimately leading to the development of an efficient multi-physics DNS/LES code of arbitrarily high accuracy called NGA. This code has meanwhile been used in numerous DNS and LES studies including liquid atomization, spray dynamics, spray combustion, premixed, partially-premixed, and non-premixed turbulent jets and combustion in technical devices, such as large-scale furnaces, internal combustion engines, and aircraft engine afterburners. NGA has been shown to scale extremely well on large-scale parallel computing clusters, and several simulations have been conducted on up to 50,000 processors and 1.6 billion cells. Such a tool provides a unique platform on which physical phenomena can be studied through detailed simulations, and new models can be developed and tested.

3.5.3 Computational domain

In order to get good results from LES and RANS it is necessary to have sensible models (often based on knowledge of relevant physical processes) for the scales that are not resolved. Obviously, this is a difficult thing to do when little is known about the processes involved in the physical system being studied. Due to the fact that there is virtually nothing in the literature regarding numerical work done on the two-phase water/steam turbulent pipe flows encountered in DSG, it is a necessary, significant step for us to perform a direct numerical simulation (DNS) of such a flow. This can be thought of as a numerical experiment, accounting for the proper physics. However, with Reynolds numbers on the order of 10^5 and lengths of typical solar reflector loops in the range

of 200 ft, it is simply impossible at this time to simulate a whole loop while resolving all flow scales (Reynolds number scaling is given explicitly in later sections).

To simulate a DSG-relevant gas-liquid flow that is fully resolved, we introduce a numerical "test section" that is part of a full DSG loop (see Fig. 11).

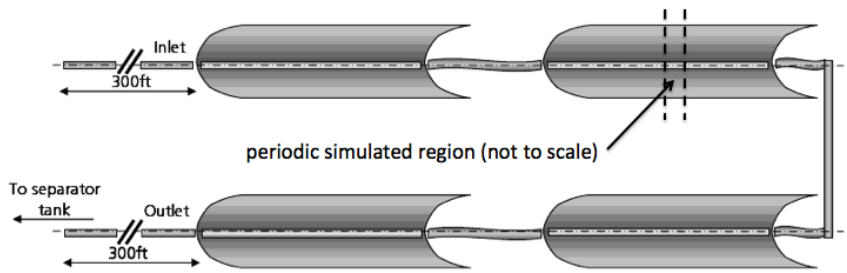

Figure 11: schematic showing the (not to scale) periodically simulated region of the DSG loop.

This region, with a length of a few inner diameters of the pipe (typically three or four, ideally more), is short enough that the flow quality remains fairly constant throughout its length, allowing us to neglect the effect of heat transfer/phase change. Initial conditions are given and the flow is then forced (see below for a discussion on both initial conditions and forcing) with periodic boundary conditions until a statistically steady state is reach.

4 Preliminary work

4.1 Test case

First, a verification test is run to analyze how the code handles the presence of gas and liquid simultaneously in a periodic section of pipe. The test case corresponds to a two-phase Poiseuille flow, testing NGA's ability to generate a discontinuous velocity gradient. A brief derivation of the exact solution is given below as follows:

For the case of steady, fully-developed, two-dimensional, stratified two-phase flow in the x-direction between to parallel plates, the Navier-Stokes equation reduces to

$$\frac{1}{\rho}\frac{dP}{dx} = \nu \frac{d^2u}{dy^2}\,, \tag{67}$$

or

$$\frac{d^2u}{dy^2} = \frac{1}{\mu}\frac{dP}{dx}\,. \tag{68}$$

For single-phase Poiseuille flow, this has the solution

$$u(y) = \frac{1}{\mu}\frac{dP}{dx}y^2 + Ay + B\,, \tag{69}$$

where the integration constants A and B are determined by the no slip condition at the top and bottom of the channel. In the case of two phases, for a channel height of H where the liquid height

ratio is h_l (i.e. the liquid reaches a height of $h_l H$), the solution in each phase is similarly

$$u_g(y) = \frac{1}{\mu_g}\left(\frac{dP}{dx}\right)_g y^2 + Ay + B \tag{70}$$

$$u_l(y) = \frac{1}{\mu_l}\left(\frac{dP}{dx}\right)_l y^2 + Cy + D\,. \tag{71}$$

The constants A, B, C and D are determined from the no-slip condition at the surfaces and the fact that there is no jump in shear stress across the interface Γ, i.e.

$$\left[\mu\frac{du}{dy}\right]_\Gamma = 0\,. \tag{72}$$

Utilizing these boundary conditions, the constants become

$$A = \frac{dP/dx_g\left(h_l^2(\mu_l - 2\mu_g) - H^2\mu_l\right) + dP/dx_l h_l^2 \mu_g}{2\mu_g(H\mu_l + h_l(\mu_g - \mu_l))}\,, \tag{73}$$

$$B = -\frac{H\left(dP/dx_g\left(h_l^2(\mu_l - 2\mu_g) - H^2\mu_l\right) + dP/dx_l h_l^2\mu_g\right)}{2\mu_g(H\mu_l + h_l(\mu_g - \mu_l))} - \frac{dP/dx_g H^2}{2\mu_g}\,, \tag{74}$$

$$C = \frac{\frac{dP/dx_g\left(h_l^2(\mu_l - 2\mu_g) - H^2\mu_l\right) + dP/dx_l h_l^2\mu_g}{2(H\mu_l + h_l(\mu_g - \mu_l))} + dP/dx_g h_l - dP/dx_l h_l}{\mu_l}\,, \text{ and} \tag{75}$$

$$D = 0\,. \tag{76}$$

The exact solution that was advected in NGA has parameters that are given in Table 3. Because

$\left(\frac{dP}{dx}\right)_l$ [kg/(m^{2}s^2)]	$\left(\frac{dP}{dx}\right)_g$ [kg/(m^{2}s^2)]	H [m]	h_l [m]	μ_l [kg/(m s)]	μ_g [kg/(m s)]
-0.0001	-0.0002	1	0.5	1.269×10^{-4}	1.698×10^{-5}

Table 3: Parameters for the two-phase Poiseuille flow used in NGA.

the flow is laminar and the flow rates of the phases are not expected to vary at all, the flow was forced by conserving the bulk flow rate U_{bulk} (the next section provides details on flow forcing). Using this bulk flow rate to define a time scale as $t' = H/U_{bulk}$, Fig. 12(a) shows the solution of the code compared to the exact solution at different values of non-dimensional time $\tau = t/t'$. As seen in Fig. 12(a), there is virtually no distinction between the initial condition and $\tau \approx 24$.

4.2 Flow forcing

Since we are interested in simulating a periodic (i.e. infinite) section of pipe, momentum lost at the walls needs to be re-introduced in the form of a source term in order to sustain the flow. Different possibilities for a gas-liquid flow include maintaining the total mass flow rate, maintaining the flow rates of each phase (note that these are not mutually exclusive), or simply forcing with a mean pressure gradient. The forcing term acts as a numerical "pump" which pushes the fluid through the pipe, similarly to the actual pump used to force fluid through the DSG loop. The forcing F_i, where subscript $i = g$ for the gas phase and $i = l$ for the liquid phase, is added to the right hand

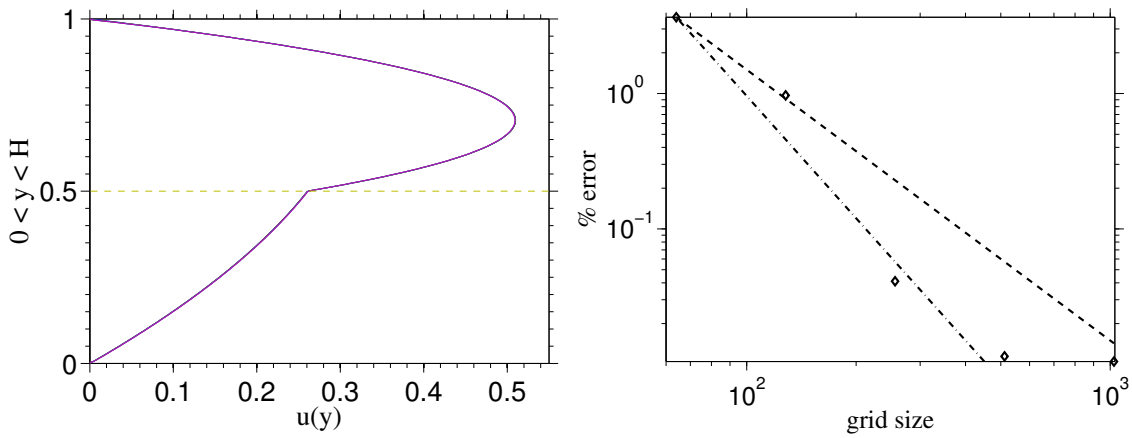

(a) Two-phase Poiseuille flow profile using NGA compared to the analytic solution at $\tau = 2.6$ (green), $\tau = 7.8$ (red), $\tau = 15.7$ (cyan), and $\tau = 23.5$ (purple). The yellow dashed line shows the location of the interface Γ.

(b) Grid convergence of the test case compared to second order (- -) and third order (- ·).

Figure 12: The test case of two-phase Poiseuille flow and the grid convergence study.

side of equation (50). The form of the forcing depends on the method selected. To enforce that the mass flow rate of each phase is maintained, F_i takes the form

$$F_i = \frac{\rho_i u_i^0 - \rho_i u_i^{n+1}}{\Delta t} \tag{77}$$

where the superscript n denotes the time step of the simulation and Δt is the step size. This just enforces that the phase flow rate of each time step is the same as that of the preceding step. Note that the denominator Δt is only present here for dimensional consistency with the other terms in eqn (50).

The other options discussed here is to force the flow with a mean pressure gradient in the axial direction, which we will call x. Then the forcing F_i takes the form

$$F_i = \frac{1}{\Delta t}\overline{\frac{dP}{dx}}\,, \tag{78}$$

where $\overline{dP/dx}$ is the mean gradient in the axial direction. This form of F_i is much more natural, as each phase feels the pressure gradient force per unit mass ($\frac{1}{\rho_i}\overline{dP/dx}$) differently according to its density. Although we expect the flow rates of each phase to reach a statistically stationary state, we do not know what that value will be. The added benefit of this form of F_i is exactly that: we are not forcing the flow rate of each phase, since it is only arbitrarily prescribed by our initial conditions.

To experiment with the difference between the forcing options, we performed a two-dimensional version of the vertical annular flow taken from Rodriguez [14]. A comparison of the second and third options is shown in Fig. 13(a), showing that the difference in the forcing mechanisms lies mostly in the quantitative value of velocity and not in the qualitative structure of the flow. The

flow converged to an annular flow, as was the case in the experiment that Rodriguez simulated. The placement of the test case on the vertical flow regime map of Hewitt is shown in Fig. 15(d).

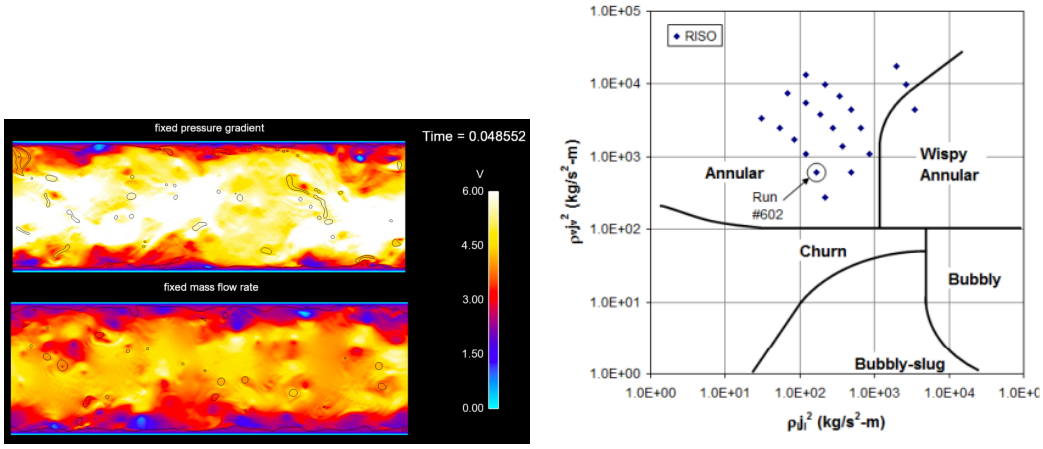

(a) Comparison of different forcing mechanisms. (b) Flow regime map of Hewitt taken from Rodriguez [14].

Figure 13: Comparison of forcing mechanisms (a) and the vertical regime map of Hewitt taken from Rodriguez [14].

Figure 14 demonstrates the fluctuation of the phase flow rates for a simulation that is forced with a mean pressure gradient, showing the progression towards a statistically stationary value. In both phases, the stationary value that the flow seems to be converging to deviates from the initial value. This option was chosen since it does not require a priori knowledge about the flow rate in

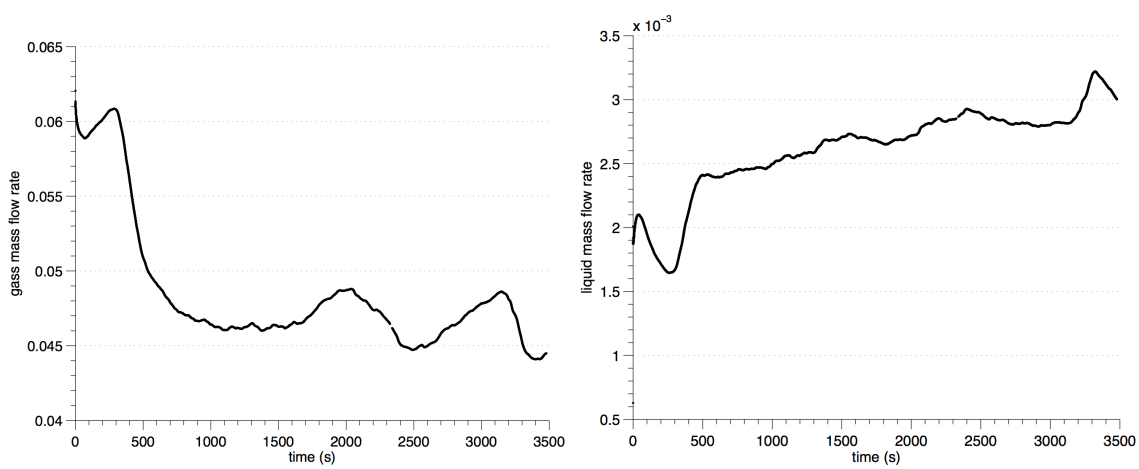

(a) Mass flow rate of the gas phase. (b) Mass flow rate of the liquid phase.

Figure 14: The mass flow rates of the gas and liquid phases.

each phase.

4.3 Transverse gravity

After determining the best way to force the gas-liquid pipe flow, we explored the effect of transverse gravity for different DSG parameters, in two dimensions. There is no mechanism for film drainage in 2D other than the film breaking and falling to the bottom of the pipe, so the dynamics of the flows are quite different than in three dimensions. However, the flows do converge to annular, as seen in Fig. 15. In effort to build from the work done in the literature survey, these flows with DSG parameters are plotted on the Taitel and Dukler [16] map, confirming the annular appearance (see Fig. 15).

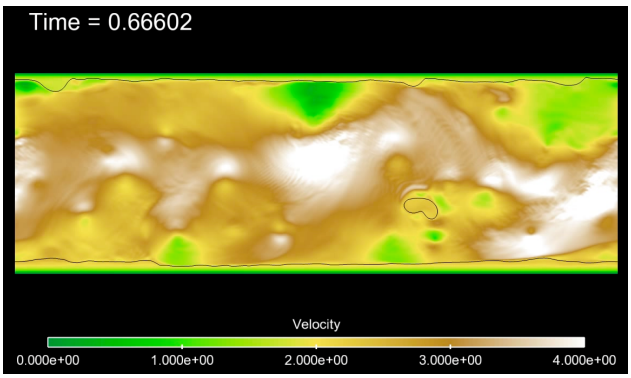

(a) Annular 2D flow with AR = 3.

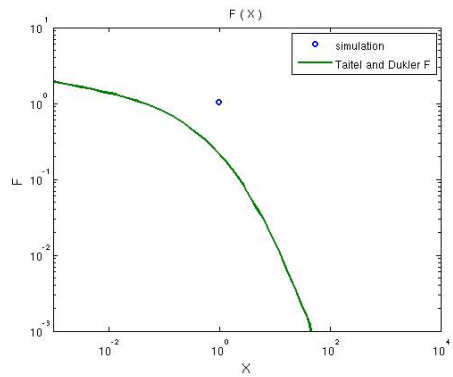

(b) F transition parameter for AR = 3 pipe, indicating annular flow.

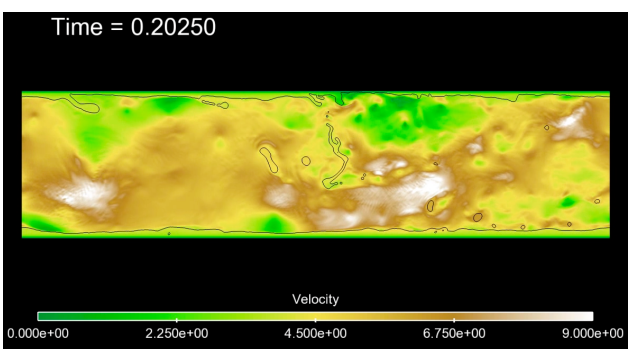

(c) Annular 2D flow with AR = 4.

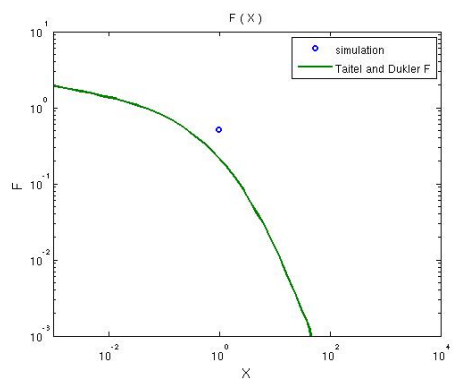

(d) F transition parameter for AR = 4 pipe, indicating annular flow.

Figure 15: 2D simulations of annular flows with DSG parameters for an aspect ratio of 3 (a) and 4 (c), with the corresponding flow regime maps ((b) and (d)).

It is worth noting that the simulation with the thicker film on the top (the AR = 3 case) lies further across the stratified-wavy to annular transition parameter than the AR = 4 case.

4.4 Three dimensions

As preliminary testing for the code's behavior in three dimensions, two simulations were run. The first was again a simulation taken from Rodriguez [14], shown in Fig. 16(a). To examine the code's

three-dimensional behavior in the presence of transverse gravity, a simulation was done using DSG fluid properties and pressure drop data obtained from Abengoa. The gas-liquid interface is shown, colored by velocity in Fig. 16(b). The film drainage mechanism is highlighted in Fig. 16(c). Both 3D simulations are under-resolved, but suffice for test cases and demonstrate that the code works properly.

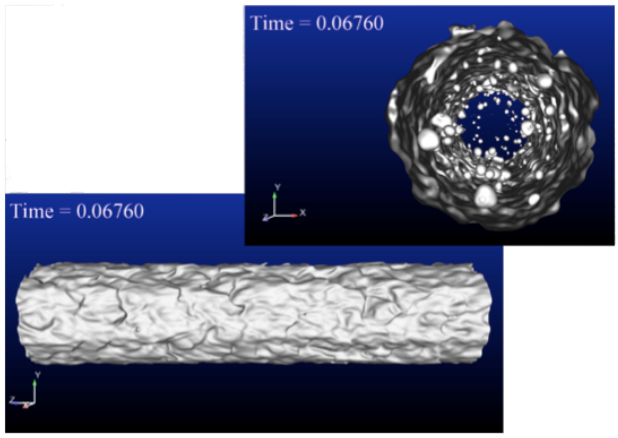

(a) 3D version of Rodriguez [14].

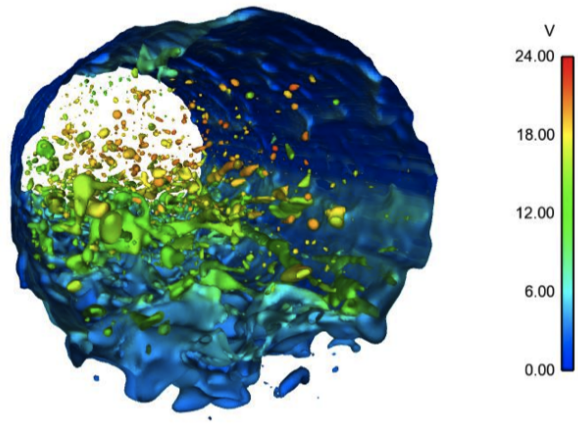

(b) Interfacial distribution in the presence of gravity.

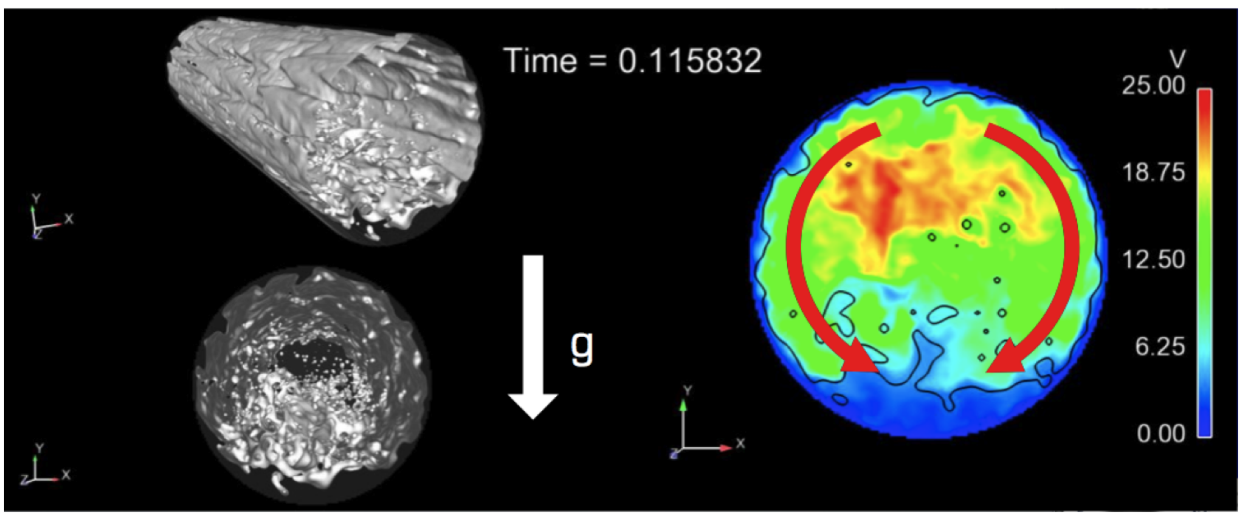

(c) Highlighting the mechanism for film drainage due to gravity.

Figure 16: Test simulations in three dimensions.

A good choice of initial conditions can affect the time that is required for a simulation to reach a statistically steady state. In anticipation of an annular flow with a gas core, we initialize the flow in a natural and simple way: with a liquid annulus of uniform thickness that is independent of orthoradial angle θ. On top of this annulus we put a perturbation to the liquid-gas interface to promote rapid destabilization. This perturbation is adapted from Rodriguez [14] and is defined as

$$\delta_\Gamma = \zeta \cos\left(\frac{2\pi}{\lambda_p} x\right) , \tag{79}$$

where

$$\lambda_p = \frac{2\pi}{\kappa_c} \quad \text{and} \quad \kappa_c = \left[\frac{(\rho_l - \rho_g)g}{\sigma}\right]^{1/2} \tag{80}$$

is the most unstable wavenumber for a Kelvin-Helmholtz instability. The perturbation amplitude is set to twice the cell size: $\zeta = 2\Delta$, where $\Delta = \Delta x = \Delta y = \Delta z$ for our simulations. In eqn (79) x is the axial coordinate, g is gravity, and σ is surface tension.

5 Resolution requirements

5.1 Turbulent scaling arguments for DNS

5.1.1 General Reynolds number considerations

We will call the characteristic velocity and lengthscale of this pipeflow U and L, and say that $L = D$, where D is the pipe diameter. The largest eddies within this flow have characteristic lengthscale l_0, which is comparable to the flow scale L. The characteristic velocity of these largest eddies we will call u_0, and this velocity is on the order of the r.m.s. turbulence intensity, which is comparable to U. The Reynolds number $\mathrm{Re}_0 = \frac{u_0 l_0}{\nu}$ based on these quantities is quite large (it is comparable to the Reynolds number based on the flow scales, Re= $\frac{UL}{\nu}$). The kinetic energy of these largest eddies is of order u_0^2, and their timescale scales as $\tau_0 = l_0/u_0$. Thus the rate of energy transfer in the turbulent cascade scales as $u_0^2/\tau_0 = u_0^3/l_0$. As the energy transfer starts with these largest eddies, the rate of dissipation of energy ε therefore scales as u_0^3/l_0.

Based on Kolmogorov's first similarity hypothesis, which states that the statistics of small-scale motions are universal and uniquely determined by ν and ε, the Kolmogorov length, velocity, and time scales can be formed:

$$\eta = \left(\frac{\nu^3}{\varepsilon}\right)^{1/4} \tag{81}$$

$$u_\eta = (\varepsilon\nu)^{1/4} \tag{82}$$

$$\tau_\eta = \left(\frac{\nu}{\varepsilon}\right)^{1/2} . \tag{83}$$

combining this with the scaling that $\varepsilon \sim u_0^3/l_0$, this reveals that the disparity between the largest length/time scales and the smallest length/time scales go like

$$\frac{l_0}{\eta} \sim \mathrm{Re}^{3/4} \tag{84}$$

$$\frac{\tau_0}{\tau_\eta} \sim \mathrm{Re}^{1/2} . \tag{85}$$

For the case of wall-bounded flows, the viscous velocity scale u_η is referred to as the friction velocity u_τ, defined from the wall shear stress as

$$u_\tau = \sqrt{\frac{\tau_w}{\rho}} .$$

The viscous lengthscale based on this velocity is then defined as

$$\delta_\nu = \frac{\nu}{u_\tau} .$$

Note that writing ε in terms of u_τ via eqn (82) and plugging into eqn (81) yields exactly this expresssion.
The friction Reynolds number based on the pipe radius δ is defined as

$$\mathrm{Re}_\tau = \frac{\delta u_\tau}{\nu} = \frac{\delta}{\delta_\nu}\,.$$

A good fit for the relation between Re_τ and Re is (Pope, 2000)

$$\mathrm{Re}_\tau \approx 0.09\mathrm{Re}^{0.88}\,, \tag{86}$$

suggesting that the disparity between the characteristic large scale δ and the characteristic scale in the near wall region δ_ν goes like

$$\frac{\delta}{\delta_\nu} \sim \mathrm{Re}^{0.8}\,. \tag{87}$$

In order to get an estimate for the total number of points required for a DNS, the number of time steps is accounted for. The timestep Δt should be on the order of the Kolmogorov time τ_η, and the simulation must also run for at least the timescale corresponding to the largest timescale τ_0 (the integral timescale). Thus the number of time steps required goes like $n_t \sim \tau_0/\Delta t$. Based on reasons relating to stability (explicit solvers) or accuracy (implicit solvers), we can relate Δt to the grid spacing Δx through the CFL condition $U\Delta t/\Delta x \sim 1$, so that $\Delta t \sim \Delta x/U$. Combining this with the fact that $\tau_0 \sim l_0/u_0$, it is shown that

$$n_t \sim \frac{\tau_0}{\Delta t} \sim \frac{l_0}{\Delta x}\,.$$

Because $\Delta x \sim \Delta y \sim \Delta z \sim \eta$, this means that from eqn (81) the total number of points required to resolve all scales is

$$N \sim n_x n_y n_z n_t \sim \left(\mathrm{Re}^{3/4}\right)^4 = \mathrm{Re}^3\,. \tag{88}$$

For wall-bounded flows, the case could actually be even worse. Performing the same analysis, but using eqn (87) to account for the disparity between the largest and smallest scales, the total number of points to resolve all scales is

$$N \sim \left(\mathrm{Re}^{0.8}\right)^4 = \mathrm{Re}^{3.2}\,. \tag{89}$$

5.1.2 Frictional resolution requirements

In order to resolve all the scales in a simulation, one must carefully resort to scaling arguments. For turbulent pipe flow driven by a pressure gradient, the Reynolds number is related to the pressure gradient through the friction factor. Having two phases complicates things, but we know that in the absence of a liquid film the gas Reynolds number approaches the conventionally defined Reynolds number for a single phase flow: $\mathrm{Re}_g \to \mathrm{Re}$ as $\alpha \to 1$. Using this reasoning, it is not unreasonable to force a gas-core dominated annular flow (this is elaborated in the following sections) with the corresponding single-phase pressure gradient that occurs in the limit as $\alpha \to 1$.

An estimate for the grid resolution required to resolve all scales of motion comes from the measured pressure gradient. As an example, consider the pressure drop provided by Abengoa for a reportedly annular flow. The pressure drop measured was -8.95 bar/200 m = -4475 Pa/m. From

Reynolds decomposition of the Navier-Stokes equations in polar-cylindrical coordinates, the axial component gives

$$-\frac{dP}{dx} = 2\frac{\tau_w}{r}\,, \tag{90}$$

where r is the radius of the pipe ($r = 0.02$ m). This leads to $\tau_w = 44.75$ Pa, and thus $u_\tau = \sqrt{\tau_w/\rho} = 0.23$ m/s (the liquid density of 844.83 kg/m^3 at 300 psig has been used). For a DNS, the grid resolution should be on the order of $\Delta x^+ = 1$ to resolve the viscous sublayer. Using this to extract the mesh spacing, we get

$$\frac{\Delta x\, u_\tau}{\nu} = \Delta x^+ = 1 \implies \Delta x = 6.53 \times 10^{-7}\ \mathrm{m}\,. \tag{91}$$

Given a diameter of $D = 0.04$ m, $D/\Delta x = 6.13 \times 10^4$, so the number of points across the diameter is roughly $n \approx 6 \times 10^4$. For a Cartesian grid with cells of aspect ratio 1, the total number of grid points is $N = (6 \times 10^4)^3\mathrm{AR}$, where AR is the aspect ratio. For AR = 4, this would mean $N = 9.2 \times 10^{14}$ grid points (on the order of 1 quadrillion).

5.1.3 Gas-liquid interface resolution requirements

The Weber number is a measure of the ratio of aerodynamic forces arising from dynamic pressure to surface tension forces, and is defined as

$$\mathrm{We} = \frac{\rho_c u^2 l}{\sigma}\,, \tag{92}$$

where ρ_c is the density of the carrier fluid, u is the relative velocity, l is the characteristic length over which surface tension acts, and σ is the surface tension. The Weber number that corresponds to vibrational breakup (the most basic type of breakup, where a single drop is broken into two) is We ≈ 12. For a DNS, all of these breakups should be captured by the computational mesh. Returning to our annular flow example, we have a flow quality of 10 % and a mass flow rate of 0.8 kg/s. An estimate of the relative velocity between the liquid film and the gas core of a droplet at the edge of the film being entrained by the core can be estimated from Fig. 17, and is roughly

$$u = u_{gas} - u_{liq} \sim (11 - 5)\ \mathrm{m/s} = 6\ \mathrm{m/s}\,. \tag{93}$$

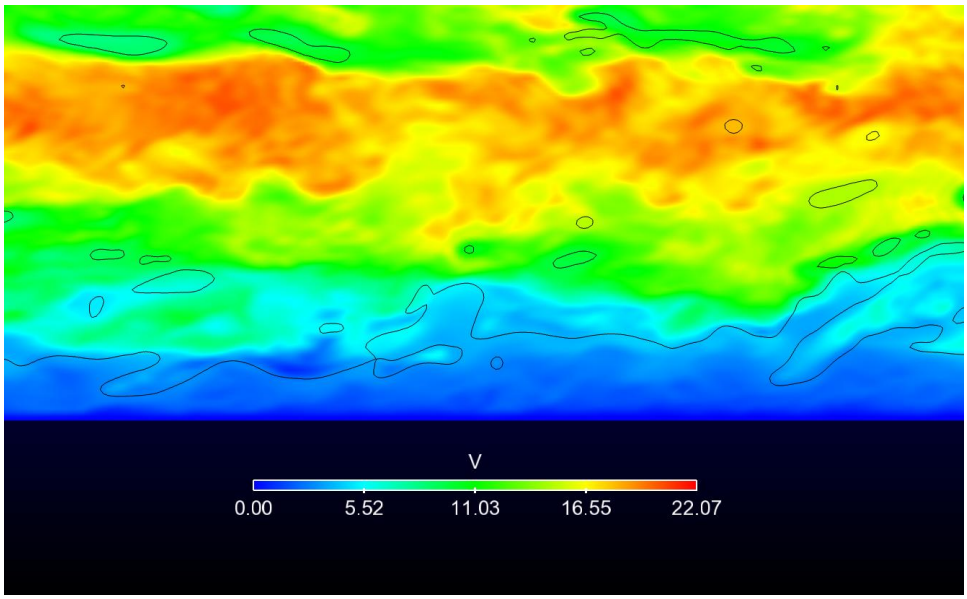

Figure 17: Relative velocity of the phases at the interface.

With a gas density of 10.87 kg/m^3 and a surface tension of 3.4×10^{-2} N/m (conditions at 300 psig), we can set a grid-based Weber number to roughly We = 8. Knowing that we need this breakup process to occur over 2 grid cells, we can extract the smallest Δx possible to capture vibrational breakup based on these parameters. This gives

$$\frac{10.87 \text{ kg/m}^3 \, (6 \text{ m/s})^2 \, 2\Delta x}{3.4 \times 10^{-2} \text{ N/m}} = 8 \implies \Delta x \approx 3.475 \times 10^{-4} \text{ m}\,, \tag{94}$$

which is about three orders of magnitude larger than the Δx obtained based on frictional resolution requirements, so *if* we had the computational resources to use that previous Δx, we should capture all of the proper physics at the interface.

5.2 Flow characterization

The friction factor as a function of Reynolds number for a single-phase pipe flow has been well-documented in the literature. The wealth of data from the Princeton superpipe and the University of Oregon research group [60] show excellent correspondence with the empirical fit

$$\frac{1}{\sqrt{f}} = 1.930 \log_{10}\left(\sqrt{f}\,\text{Re}\right) - 0.537\,, \tag{95}$$

and Prandtl's friction law for smooth pipes [61] gives

$$\frac{1}{\sqrt{f}} = 2.0 \log_{10}\left(\sqrt{f}\,\text{Re}\right) - 0.8\,. \tag{96}$$

Solving these implicit equations iteratively to obtain f for Re = 5,000, say, eqn (96) yields $f = 0.0367$ while eqn (95) yields $f = 0.0374$. Then the pressure gradient that corresponds to a given

Reynolds number for a single phase flow can be obtained from the definition of the friction factor:

$$f = \frac{(-dP/dx)D}{\frac{1}{2}\rho\overline{U}^2}\,, \tag{97}$$

where x is the axial coordinate of the pipe, D is the diameter, ρ is the fluid density, and $\overline{U}$ is the bulk velocity of the fluid (note that the denominator is the dynamic pressure due to the bulk velocity). Re is the conventional Reynolds number defined as

$$\mathrm{Re} = \frac{\overline{U}D}{\nu}\,. \tag{98}$$

In the case of a gas core-dominated annular flow, we substitute $\overline{U}$ with the superficial gas velocity j_g and the Reynolds number that is solved for becomes the gas Reynolds number. The pressure gradient used to drive the flow is then obtained from the friction factor that is iteratively solved for from this Re_g.

6 Reduction of governing flow parameters

Much of the information found in the literature regarding the interfacial distribution of the gas-liquid interface for horizontal pipe flows is based solely on visualization of the flow and experimental correlation: there is a lack of theoretical understanding that would allow to describe the form of the interface. As annular flows in which the liquid is distributed in the form of a contiguous film around the pipe walls is desirable to prevent dry-out conditions that may be damaging to DSG equipment, this regime of flow is of particular interest. As this project aims to better understand the character of gas-liquid flows in horizontal pipes from first principles, some effort was put towards understanding flow "annularity" from a theoretical perspective.

The presence of two phases makes DSG-relevant flows much more complicated than single-phase pipe flows. The best way to approach the physical system in a fundamental way is through dimensional analysis. The Buckingham-Pi theorem is a mathematical theorem that can be very useful to reduce a set of governing equations and physical parameters to equivalent expressions in dimensionless form, providing insights into the relevant physical processes. The choice of dimensionless parameters is not unique, so the output from the theorem depends on the "user input": but if the proper physical processes can be selected than this approach can be very powerful. Tthis work has been done under the assumption that the flow quality does not change much over a short length of pipe, allowing us to neglect heat transfer/phase change. Under the additional assumption of an annular flow that is dynamically dominated by the gas core (an assumption that preliminary simulations suggest is valid), dimensional analysis yields six dimensionless groups that govern the

flow:

$$\text{gas Reynolds number Re}_g = \frac{\rho_g j_g D}{\mu_g}\,, \tag{99}$$

$$\text{gas Weber number We}_g = \frac{\rho_g j_g^2 D}{\sigma}\,, \tag{100}$$

$$\text{Froude number Fr} = \sqrt{\frac{\rho_g j_g^2}{\rho_l g D}}\,, \tag{101}$$

$$\text{void fraction } \alpha_g = \frac{A_g}{A}\,, \tag{102}$$

$$\text{density ratio } r_\rho = \frac{\rho_l}{\rho_g}\,, \quad \text{and} \tag{103}$$

$$\text{viscosity ratio } r_\mu = \frac{\mu_l}{\mu_g}\,, \tag{104}$$

where $\rho_{g/l}$ and $\mu_{g/l}$ are the density and dynamic viscosity of the gas and liquid phases, j_g is the superficial gas velocity, D is the pipe diameter, σ is the surface tension, g is gravity, A is the cross-sectional area of the pipe, and A_g is the cross-sectional area occupied by the gas phase. Note that the void fraction $\alpha_g = 1 - \alpha_l$, where α_l is the liquid volume fraction (a measure of how much liquid is in the domain).

6.1 Importance of the Froude number

In order for a vapor core to sustain a liquid film at the top of the pipe, the vapor must carry a lot of momentum since the liquid has a much higher density than the vapor. Thus its velocity must be quite high, leading to issues with flow resolution. The Froude number as we have defined it is a measure of the ratio of aerodynamic forces from the gas phase to gravitational effects on the liquid phase. Fr ≈ 1 is the value that governs "annularity": $Fr > 1$ leads to the presence of a contiguous film while $Fr < 1$ means that the film is not contiguous around the pipe and that the interfacial distribution converges to a stratified flow as Fr $\to 0$. Therefore, it is possible to obtain an annular flow with any two fluids by modifying the gravity such that $Fr \gg 1$.

Two main avenues have been explored to alleviate this issue: (1) reducing the density ratio to a very low value, and (2) reducing gravitational acceleration. This is of course not physical, but in parameter space the flow is still be very relevant to the realistic, DSG-relevant flows.

6.1.1 Simulations testing Fr

In light of the above discussion, a variety of test cases have been contrived for validation. The question at hand is: how does this small amount of liquid take shape inside the pipe? After choosing the density ratio and the quality, whether or not an upper film is present is governed by the ratio of intertial (aerodynamic) forces to gravitational forces. We know that if gravity were not present, there would be nothing causing the flow to be stratified. These competing effects are encapsulated by the Froude number. Figure. 18 demonstrates this for simulations with different values of Fr.

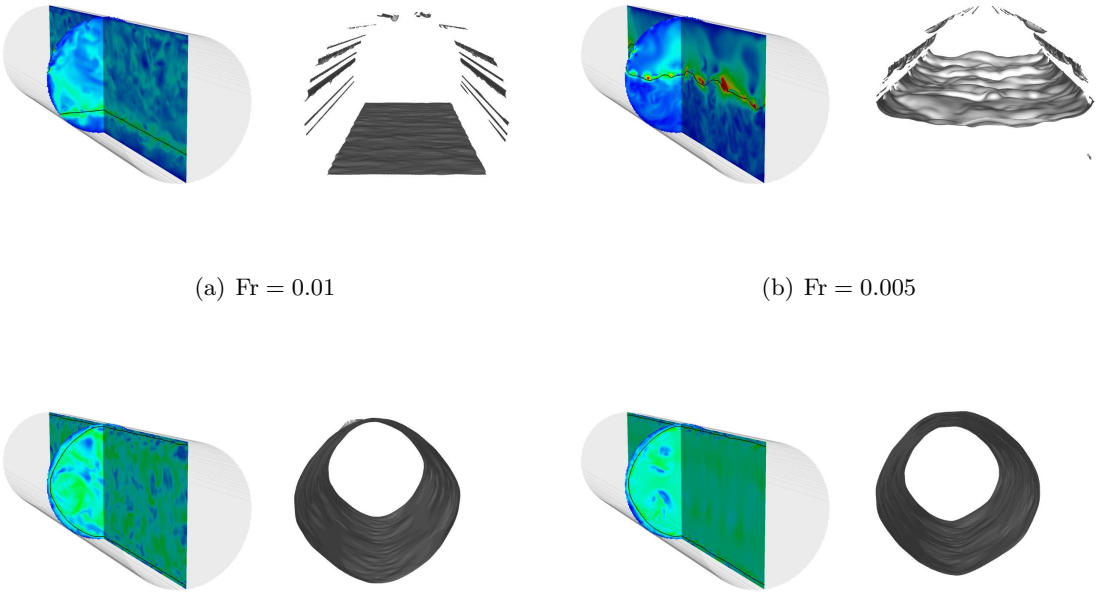

(a) Fr = 0.01

(b) Fr = 0.005

(c) Fr = 1.43

(d) Fr = 2.0

Figure 18: Test cases demonstrating the connection between Fr and flow regime.

It is worth noting that both simulations that converge to an annular flow have Fr ~ 1, while the two that converge to stratified/stratified-wavy flow have Fr $\ll 1$.

7 DSG-relevant simulations

7.1 Abengoa parameters

The Buckingham-Pi theorem used in dimensional analysis generates independent dimensionless parameters, meaning that the six groups shown above should be independent of one another. This is very useful, as it means that we can capture the relevant physics based on how well we can match the dimensionless parameters. Four different cases were given to us from Abengoa, the fluid properties for each given in Table 4 and the operating conditions given in Table 5, where $\dot{m}$ is the total mass flow rate, x is the flow quality, and dP/dz is the reported pressure drop per unit length for the DSG loop (the mean pressure gradient). The "G" and "S" refer to the Golden (low pressure) and Spain (high pressure) cases, respectively. Using the definitions provided in the literature review and the correlation for void fraction, the six dimensionless groups are computed for each case and provided in Table 6.

Although NGA [58] has the unique ability to account for high density ratios (see section 3.4), three of these dimensionless groups must be considered in light of resolution requirements, namely Re_g, We_g, and α_g. As Re_g goes up, the Kolmogorov scale (the smallest scales at which dissipation

Case	ρ_l [kg/m^3]	ρ_g [kg/m^3]	μ_l [kg/(m s)]	μ_g [kg/(m s)]	σ [kg/s^2]
G1	867.85	7.612	1.404×10^{-4}	1.625×10^{-5}	0.0384
G2	878.21	6.144	1.465×10^{-4}	1.590×10^{-5}	0.0404
S1	710.29	47.33	9.158×10^{-5}	2.025×10^{-5}	0.0143
S2	717.46	44.86	9.277×10^{-5}	2.010×10^{-5}	0.0151

Table 4: Fluid Properities for the ASI cases.

Case	$\dot{m}$ [kg/s]	x [%]	dP/dz [kg/(m^{2}s^2]
G1	0.541	3.23	385.25
G2	0.541	13.06	3257.17
S1	1.80	10.04	117.02
S2	1.80	68.20	695.67

Table 5: Operating conditions for the ASI cases.

occurs) goes down, and these scales must be resolved to account for all the physics. The smallest scales of interfacial effects are set by We_g, and these must be captured by the mesh to account for phase interaction properly. The reference length for the liquid film is set by α_g, and there must be enough mesh points inside the liquid film to properly resolve it. Typically, this is done by assuming a film that is not a function of orthoradial angle θ and ensuring that there is an excess number of points in this reference length. This accounts for the fact that the film is actually not symmetric due to gravity, being thinner near the top of the pipe than the bottom.

7.2 Description of performed simulations

It is computationally infeasible for us to simulate gas-core dominated flows with a gas Reynolds numbers $\sim 10^5$ or $\sim 10^6$, as is the case for gas Weber numbers $\sim 10^4$. We can however pick a gas Reynolds number that is high enough, such that the flow is fully turbulent. It is reasonable to assume that the flow characteristics become independent of Reynolds number once a high enough Reynolds number is reached. This is a common assumption in turbulent flow modeling for problems involving vast separation of scales, as further increasing the Reynolds number for an already turbulent flow decreases the Kolmogorov length scale but does not change the statistical character of the flow. Working under this assumption, five simulations were performed that are relevant to DSG, using Abengoa fluid properties and matching as many of the six dimensionless parameters as possible. These parameters are shown in Fig. 19 for each simulation, indicating which parameters are matched to the G2 and S2 cases (because those were reported to be annular) from Table 6 ("GS" and "SS" indicate "Golden simulation" and "Spain simulation").

Case	ρ_l/ρ_g	μ_l/μ_g	Re_g	We_g	Fr	α_g
G1	114.01	8.64	1.38×10^5	427.53	1.10	0.83
G2	142.94	9.21	1.41×10^5	504.76	1.22	0.84
S1	15.01	4.52	1.30×10^6	1.75×10^4	3.21	0.93
S2	15.99	4.62	1.31×10^6	1.76×10^4	3.28	0.93

Table 6: Dimensionless groups for the ASI cases.

Simulation	ρ_l/ρ_g	μ_l/μ_g	Re_g	We_g	Fr	α_g
GS1	142.94	9.21	5,000	504.76	1.22	0.84
GS2	142.94	9.21	13,000	504.76	1.22	0.84
GS3	142.94	9.21	5,000	504.76	1.22	0.42
SS1	15.99	4.62	5,000	1,000	3.28	0.85
SS2	15.99	4.62	10,000	3,000	3.28	0.85

not matched matched

Figure 19: The matching of the six dimensionless groups for the DSG-relevant simulations.

7.3 Effect of varying void fraction

The GS1 simulation had a quality converged under 50 %, which is high compared to the 13 % reported by ASI. This likely means that the void fraction correlation

$$\alpha_g = \left(1 + 0.28\, X^{0.71}\right)^{-1}$$

over-predicts the actual void fraction, at least with the chosen values of Reynolds number. Based on this assumption, GS3 was simulated with half the void fraction of GS1, and the converged quality is under 25 %. The qualities for the two runs are shown in Fig. 20.

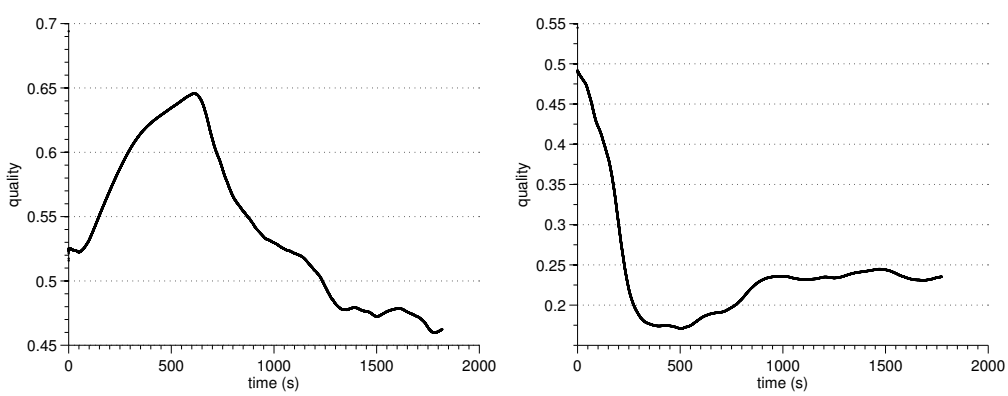

(a) GS1 quality (b) GS3 quality

Figure 20: Qualities for GS1 and GS3.

7.4 Effect of increasing Reynolds number

The converged quality of the GS1 simulation was below 50 %. Figure 21 shows the quality for two simulations, GS1 (at a higher resolution) and GS2.

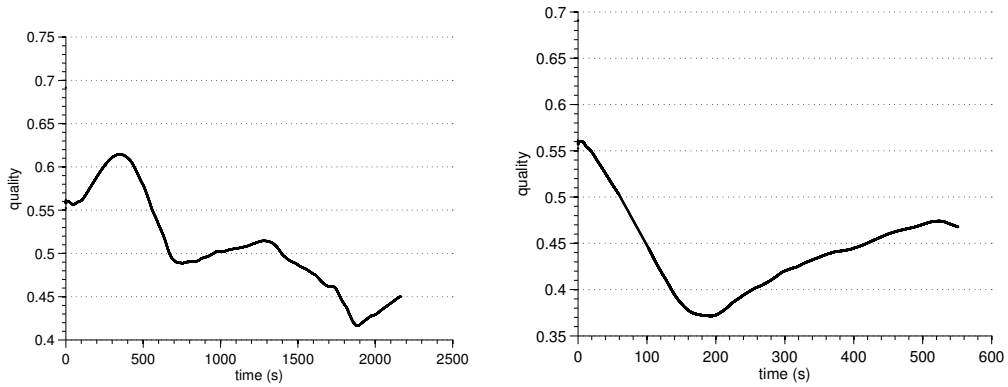

(a) GS1 (higher resolution) quality

(b) GS2 quality

Figure 21: Qualities for GS1 (higher resolution) and GS2.

Although it is difficult to conclude anything from the qualities because the simulations were not run for long enough, they certainly do not seem to suggest any reason why the qualities would be converging to different values. This may suggest that the quality is fairly insensitive to the gas Reynolds number when the void fraction is fixed.

7.5 First-order statistics

7.5.1 Liquid volume fraction

Many different statistics have been extracted for the simulations presented in Fig. 19. The most basic information to extract from the gas-liquid flow is the interfacial distribution, in other words the location of the liquid in the pipe. Figures 23 - 24 show both cross-sectional and radial averages of the liquid volume fraction $\alpha_l = 1 - \alpha_g$. Utilizing the center plane of symmetry through the pipe, radial profiles are shown at different orthoradial angles θ such that $0 \leq \theta \leq \pi$ (see the schematic in Fig. 22).

It is clear from Figs. 23(c) and 23(f) that the liquid volume fraction profiles depend heavily on the void fraction but less heavily on the gas Reynolds number. Figure 24 hints that the liquid volume fraction profiles may depend slightly on the gas Weber number. This could be possible, as droplet entrainment and deposition is one of the mechanisms for film sustainment that will be discussed later.

7.5.2 Velocity profiles

The mean velocity field is another basic statistic that provides information about the gas-liquid flow, also indicating interface topology. It is expected that velocities should be greatest in the gas core and least in the liquid film that is near the wall. Figure 25 shows both planar velocity

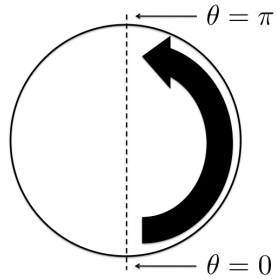

Figure 22: Definition of θ for film height and dry-out measurement.

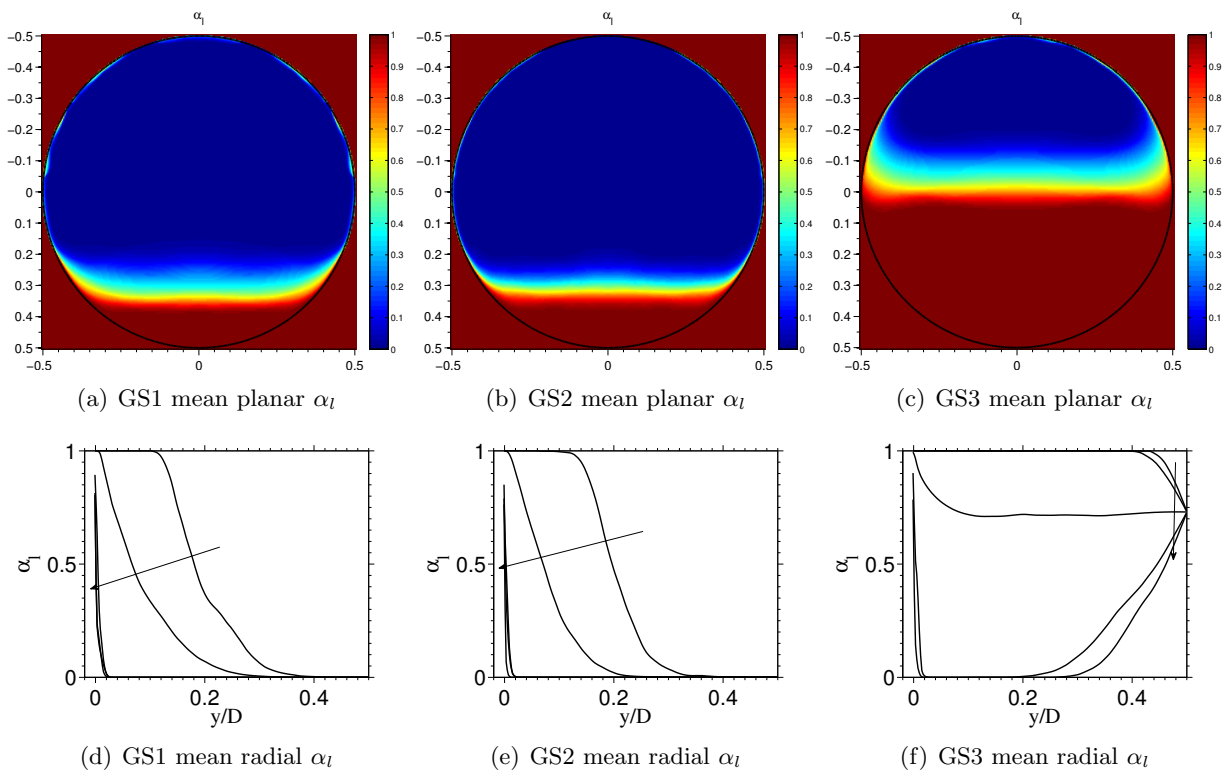

(a) GS1 mean planar α_l (b) GS2 mean planar α_l (c) GS3 mean planar α_l

(d) GS1 mean radial α_l (e) GS2 mean radial α_l (f) GS3 mean radial α_l

Figure 23: Mean planar and radial liquid volume fractions for the GS1, GS2, and GS3 simulations in Fig. 19. The arrow points in the direction of increasing θ.

magnitude in the pipe cross section and radial velocity profiles at different values of orthoradial angle θ for the GS1, GS2, and GS3 simulations. The values are shown in $^+$ units, meaning that they have been normalized by viscous scales (this is standard in turbulent velocity fields). The friction velocity is defined as $u_\tau = \sqrt{\tau_w/\rho}$, where τ_w is the shear stress at the wall and ρ is the fluid density. Based on our assumption of a gas-core dominated annular flow, τ_w is the shear stress that would be attained with a void fraction of $\alpha_g = 1$ (no liquid present), and ρ is taken to be the

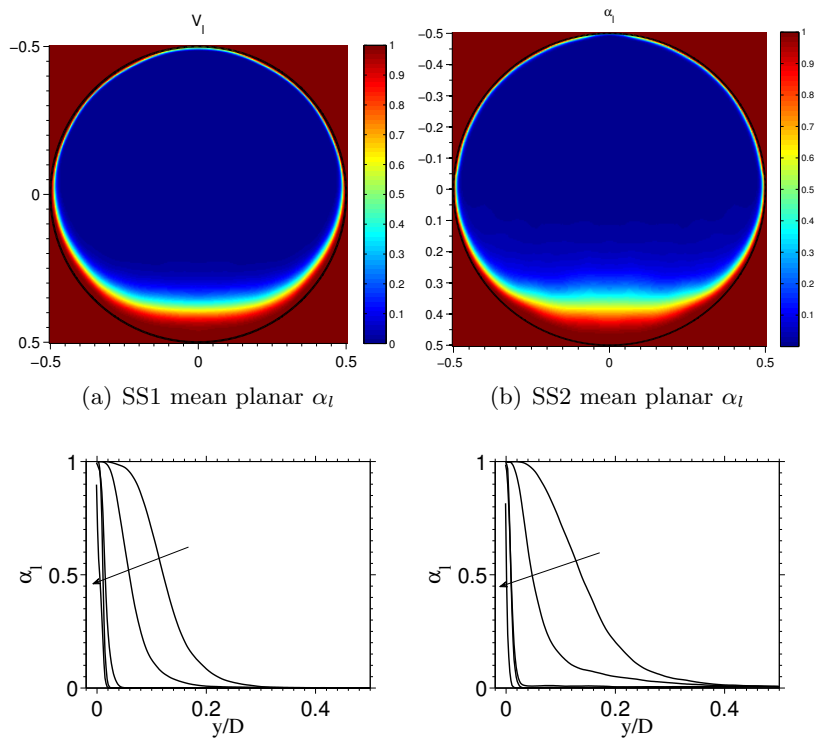

(a) SS1 mean planar α_l (b) SS2 mean planar α_l

(c) SS1 mean radial α_l (d) SS2 mean radial α_l

Figure 24: Mean planar and radial liquid volume fractions for the GS3, SS1, and SS2 simulations in Fig. 19. The arrow points in the direction of increasing θ.

density of the gas. Then our U^+ and y^+ are defined as

$$U^+ = \frac{U}{u_\tau} \quad \text{and} \quad y^+ = \frac{u_\tau y}{\nu_g}\,, \tag{105}$$

where y is the distance from the wall and ν_g is the kinematic viscosity of the gas.

Similar to the liquid volume fraction, the velocity magnitude changes in value when Re_g is increased, but statistically it has not changed much. It looks vastly different however for different values of α. Figure 26 shows the same images for the SS1 and SS2 simulations. Figures 26(a) and 26(b) show that the magnitude of the velocity has increased as Re_g has increased from 5,000 to 10,000. The radial profiles show some variation, but this is reflected in the slightly different shapes of the false color planar velocities.

7.5.3 Film height and dry-out

The average distance of the liquid film from the wall of the pipe in an annular flow is of great relevance to DSG, as the likelihood of finding dry-out conditions at the pipe wall depends on whether or not liquid is present at a particular orthoradial angle. It is clear from Fig. 27 that dry-out probability increases as mean film height decreases (normalized by the pipe diameter in Fig. 27). Shown are the dry-out and film height statistics for the GS1, GS2, GS3, and SS1 simulations. The

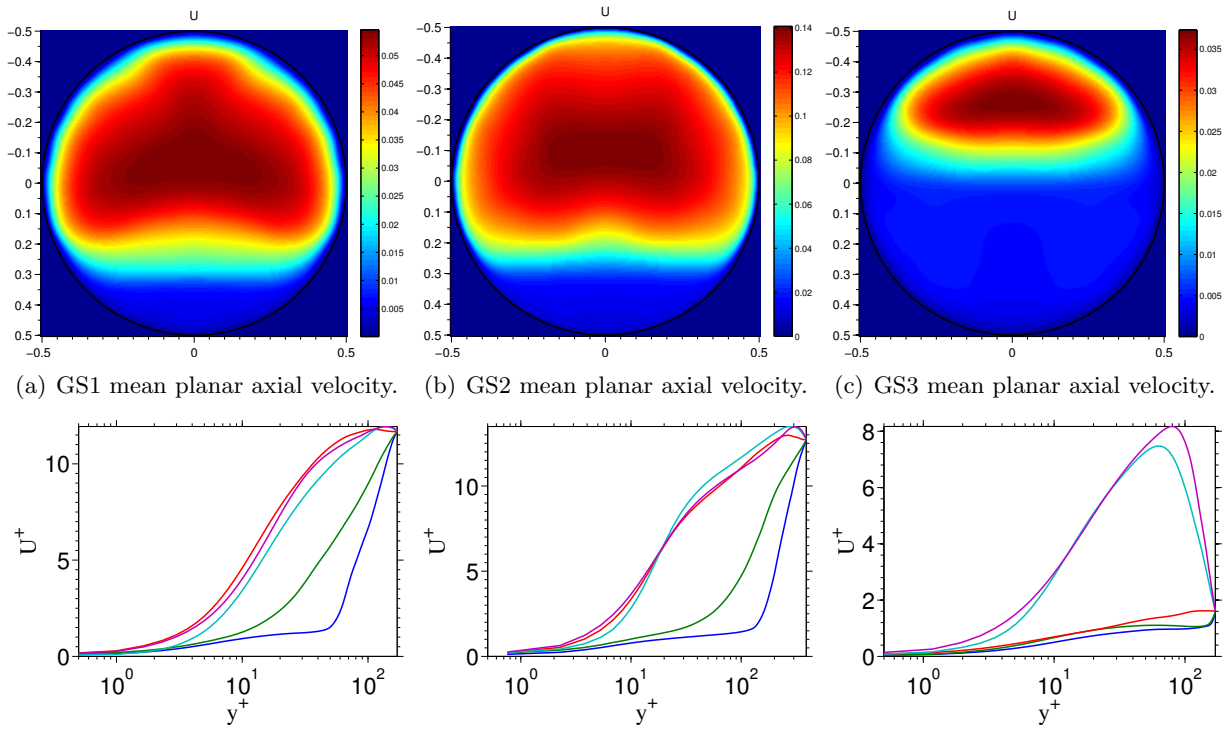

(a) GS1 mean planar axial velocity. (b) GS2 mean planar axial velocity. (c) GS3 mean planar axial velocity.

(d) GS1 radial variation of axial velocity. (e) GS2 radial variation of axial velocity. (f) GS3 radial variation of axial velocity.

Figure 25: Mean planar and radial variation of axial velocity for the GS1, GS2, and GS3 simulations in Fig. 19. Radial profiles are given at $\theta/\pi = 0$ (blue), $\theta/\pi = 1/4$ (green), $\theta/\pi = 1/2$ (red), $\theta/\pi = 3/4$ (cyan), and $\theta/\pi = 1$ (purple).

presence of the contiguous film in the SS1 simulation (due to the higher Froude number) greatly reduces the probability of finding dry-out at the pipe wall for any angle. The maximum dry-out located near $\theta/\pi = 1$ is roughly 50% for the SS1 simulation, compared to 100% for the GS1 and GS2 simulations and about 90% for the GS3 simulation.

7.6 Second-order statistics

To get an idea of where the most fluctuating regions of the flow occur, the variance in the axial component of velocity is computed. Figures 28 and 29 show both planar and radial profiles of the axial velocity variance for the Golden and Spain simulations, respectively. The notable result is that in all cases the relative variance is highest near the gas-liquid interface, likely due to interfacial shear and mechanisms such as droplet entrainment/deposition, secondary gas flow, and wave pumping (these are discussed in greater detail in the next section). For the Golden simulations this is limited to the lower regions of the pipe ($\theta/\pi \leq 1/4$) because the film is mostly drained from the top and walls of the pipe. For the Spain simulations, the variance is relatively high till $\theta/\pi \approx 1/2$ for SS1 and all the way to the top ($\theta/\pi \approx 1$) for SS2, due to the presence of a contiguous film.

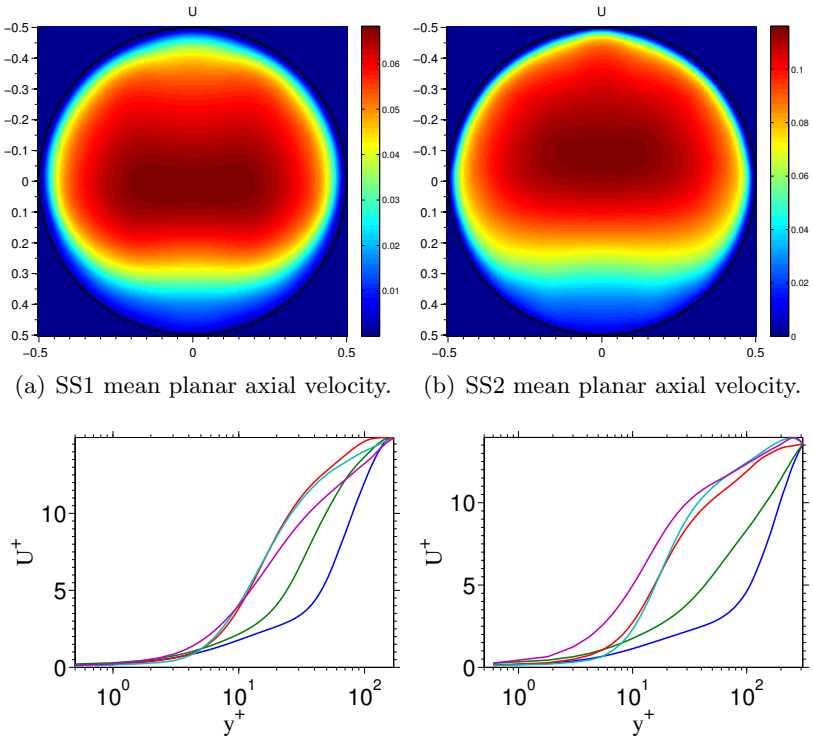

(a) SS1 mean planar axial velocity. (b) SS2 mean planar axial velocity.

(c) SS1 radial variation of axial velocity. (d) SS2 radial variation of axial velocity.

Figure 26: Mean planar and radial variation of axial velocity for the SS1 and SS2 simulations in Fig. 19. Radial profiles are given at $\theta/\pi = 0$ (blue), $\theta/\pi = 1/4$ (green), $\theta/\pi = 1/2$ (red), $\theta/\pi = 3/4$ (cyan), and $\theta/\pi = 1$ (purple).

Comparing the planar variance with the planar liquid volume fraction, It is also interesting to note the variance in the liquid phase. This is indicative of a fluctuating, turbulent liquid film.

7.7 Film sustainment

7.7.1 Mechanisms discussed in the literature

The statistics taken from the simulations shown in the previous section suggest that the Spain cases run at high pressures are much more likely to exhibit a contiguous film than the Golden cases run at low pressures. In the absence of mechanisms for replenishing the liquid film near $\theta/\pi = 1$, all of the liquid would drain down due to gravity and the flow would become stratified. What is the mechanism that replenishes the film near $\theta/\pi = 1$ in one case, but not in the other? Four main mechanisms for film sustainment have been proposed in the literature [62]:
(1) surface tension forces hold the liquid film in place,
(2) droplet entrainment from the thicker film near bottom of the pipe and deposition near the top,
(3) secondary gas flow in the circumferential direction generated by protrusions in the film surface, and
(4) wave-pumping action that pushes liquid up the pipe walls. We have extracted statistics from

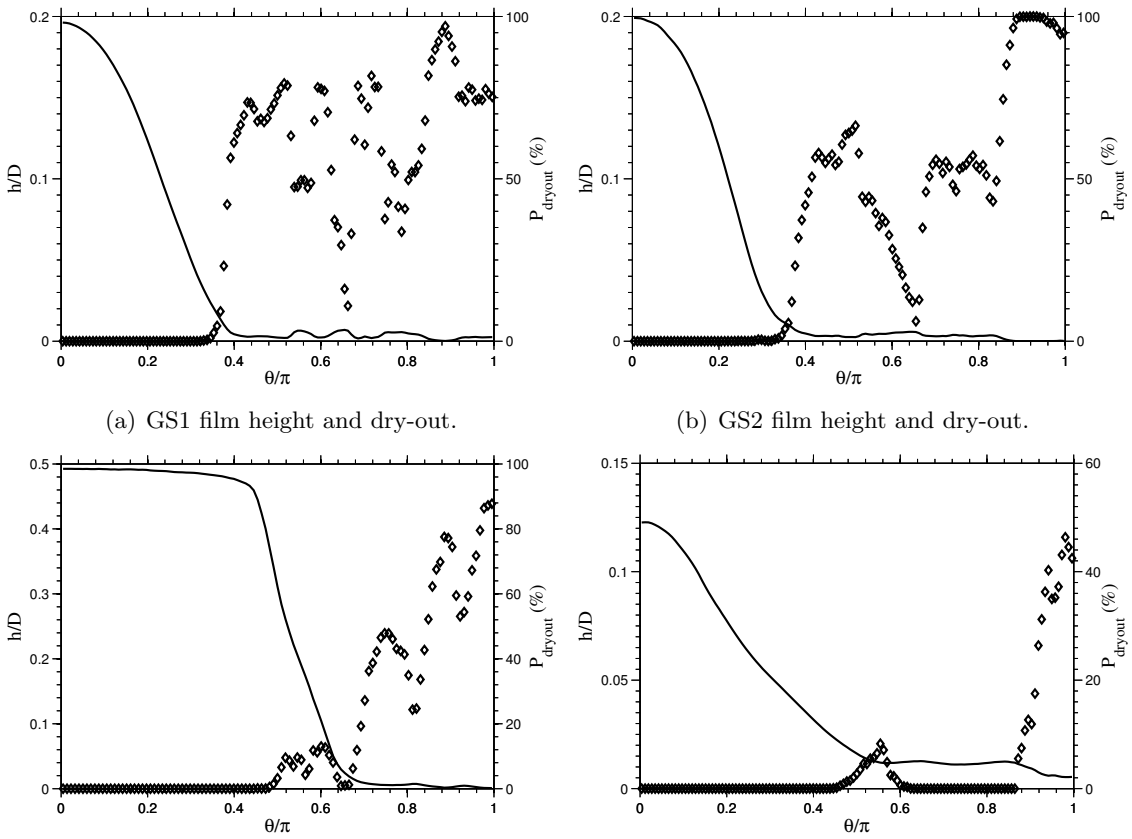

(a) GS1 film height and dry-out.

(b) GS2 film height and dry-out.

(c) GS3 film height and dry-out.

(d) SS1 film height and dry-out.

Figure 27: Mean film height and dry-out as a function of orthoradial angle for different simulations.

our simulations that seem to support mechanisms (2) - (4), demonstrating their presence for the case of Spain and absence for the case of Golden.

7.7.2 Secondary gas flow

It has been argued that the topology of the interface in an annular flow can lead to the generation of flows within the gas phase that lie in the orthoradial plane. Such flows would be physically constrained to maintain a net-zero circulation, so one would expect this secondary flow to take the form of a counter-rotating vortex pair. Figure 30 shows the extracted 2D velocities in the orthoradial plane for the GS2, SS1, and SS2 simulations, which demonstrate the presence of this vortex pair.

7.7.3 Wave pumping

Another mechanism discussed in the literature for film sustainment comes from the fact that the film is thicker on the bottom than on the top. The disturbance waves of the thicker region of the film protrude higher into the gas core, and consecutive high and low pressure regions form in front of and behind the crests. These low and high pressure regions have the effect of pumping liquid

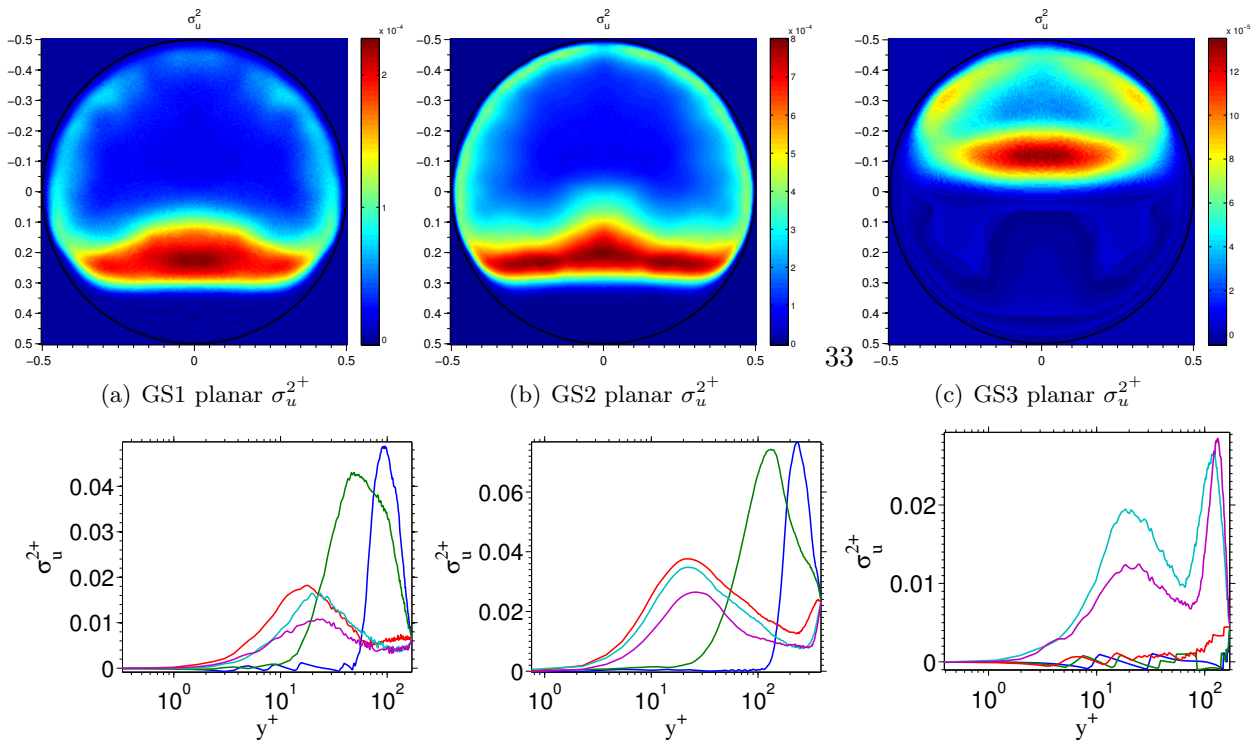

(a) GS1 planar $\sigma_u^{2^+}$ (b) GS2 planar $\sigma_u^{2^+}$ (c) GS3 planar $\sigma_u^{2^+}$

(d) GS1 radial $\sigma_u^{2^+}(\theta)$ (e) GS2 radial $\sigma_u^{2^+}(\theta)$ (f) GS3 radial $\sigma_u^{2^+}(\theta)$

Figure 28: Planar and radial axial velocity variance $\sigma_u^{2^+}$ for the GS1, GS2, and GS3 simulations in Fig. 19. Radial profiles are given at $\theta/\pi = 0$ (blue), $\theta/\pi = 1/4$ (green), $\theta/\pi = 1/2$ (red), $\theta/\pi = 3/4$ (cyan), and $\theta/\pi = 1$ (purple).

up the walls. A schematic of this mechanism can be seen in Figure 31, taken from [63]. Figure 32 shows the gas-liquid interface colored by vertical velocity for the SS1 simulation, demonstrating the propagation of liquid up the pipe walls likely due to this disturbance wave pumping. In contrast, Fig. 33 shows the lack of fluid propagation up the pipe walls. There is some positive vertical velocity, but not enough to sustain a contiguous film.

To further investigate the mechanism of wave pumping, average orthoradial liquid velocities were computed for the SS1, SS2, and GS2 simulations. Figure 34 shows that there is motion of the liquid up the pipe walls for the Spain simulations, but this propagation up the walls looks very different for the GS2 simulation in that the liquid does not propagate much past $\theta/\pi = 1/2$. The thick black line in Fig. 34 gives the average location of the gas-liquid interface, insinuating that this upward liquid motion towards the inside of the mean interface is in the form of intermittently present liquid (i.e. disturbance waves).

7.7.4 Droplet entrainment and deposition

The third mechanism for film sustainment that has been investigated in this project is droplet entrainment and deposition: droplets are entrained from the base film near lower regions of the pipe and deposited near the top and sides of the pipe, replenishing the liquid film. Figure 35

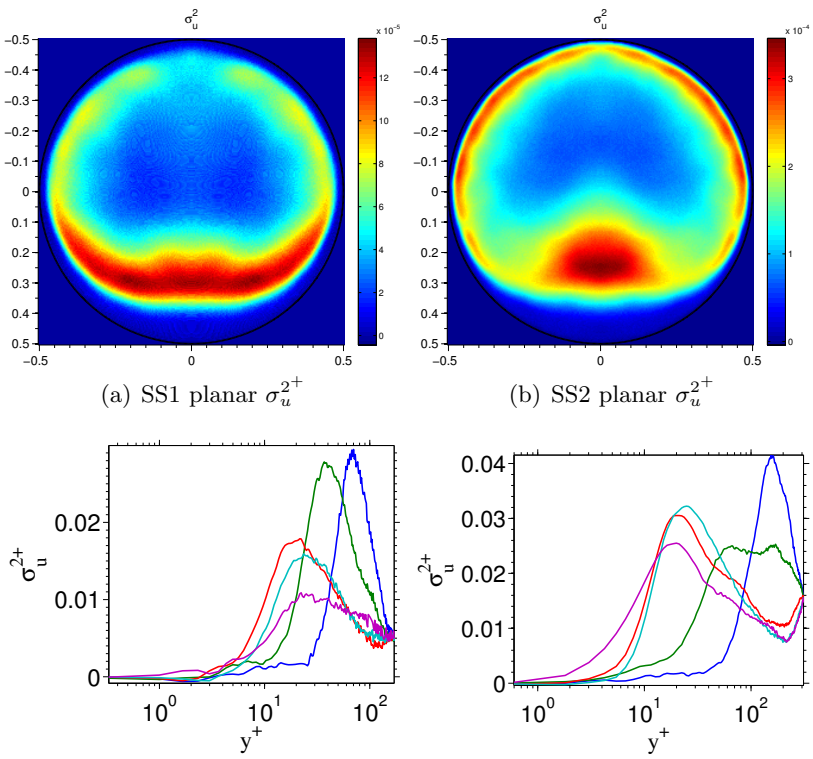

(a) SS1 planar $\sigma_u^{2^+}$ (b) SS2 planar $\sigma_u^{2^+}$

(c) SS1 radial $\sigma_u^{2^+}(\theta)$ (d) SS2 radial $\sigma_u^{2^+}(\theta)$

Figure 29: Planar and radial axial velocity variance $\sigma_u^{2^+}$ for the SS1 and SS2 simulations in Fig. 19. Radial profiles are given at $\theta/\pi = 0$ (blue), $\theta/\pi = 1/4$ (green), $\theta/\pi = 1/2$ (red), $\theta/\pi = 3/4$ (cyan), and $\theta/\pi = 1$ (purple).

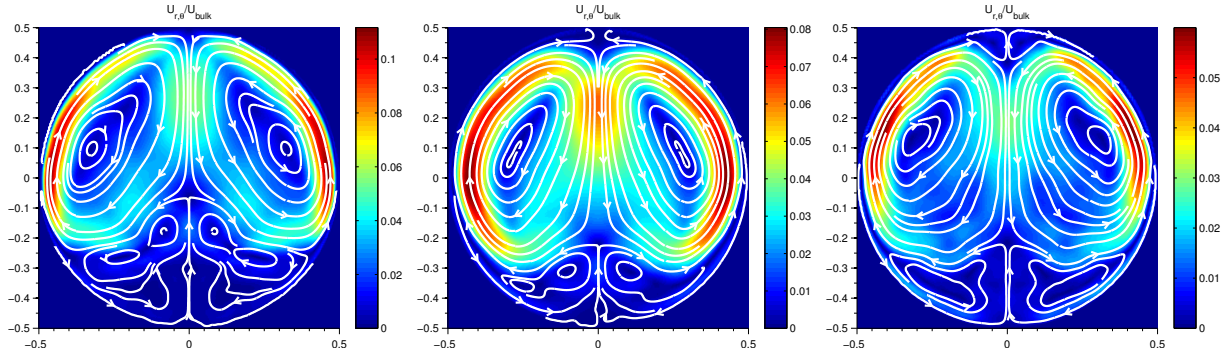

(a) GS2 orthoradial streamlines. (b) SS1 orthoradial streamlines. (c) SS2 orthoradial streamlines.

Figure 30: Streamlines demonstrating secondary gas flow.

illustrates the droplet tracking procedure that eliminates the bulk liquid film and follows only droplets that are not a part of the film. In Fig. 35(a) the drops are colored by vertical velocity,

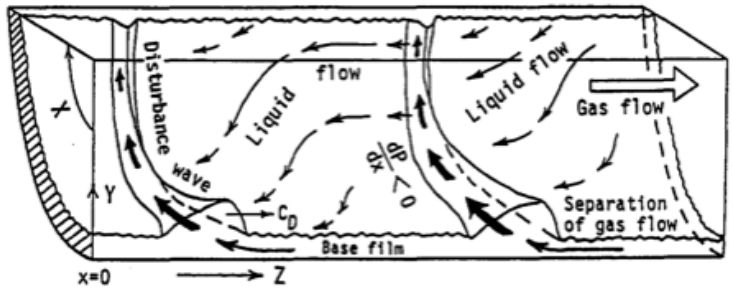

Figure 31: Illustration of the pumping action of disturbance waves [63].

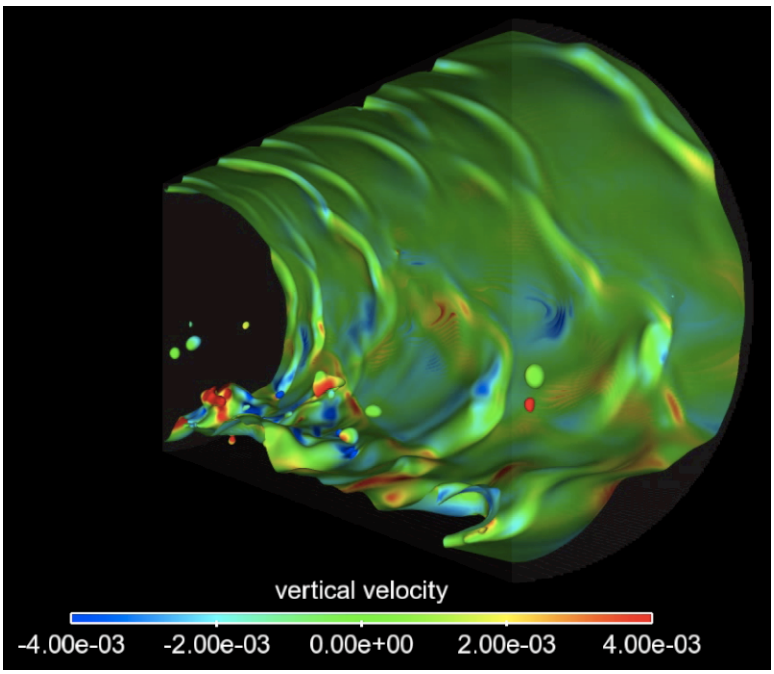

Figure 32: SS1 wave pumping.

while in in Fig. 35(b) they are colored by velocity magnitude.

It does seem that the drops that are highest in velocity magnitude tend to be the smallest, but it is unclear whether or not there is any correlation between drop size and vertical velocity. To shed light on this possibility, scatter plots of vertical position verse drop diameter are shown in Fig. 36 for the SS1, SS2, and GS2 simulations. These scatter plots are rather inconclusive, but they do show that small drops are more randomly distributed through the vertical length of the pipe while large drops are mostly toward the bottom.

Figure 37 shows integrated droplet trajectories for the SS1 simulation. Figure 37(a) shows trajectories for the 20 largest drops in the domain, while Fig. 37(b) shows trajectories for the 20 smallest drops. Although one could argue that it is more likely that drops near the top of the

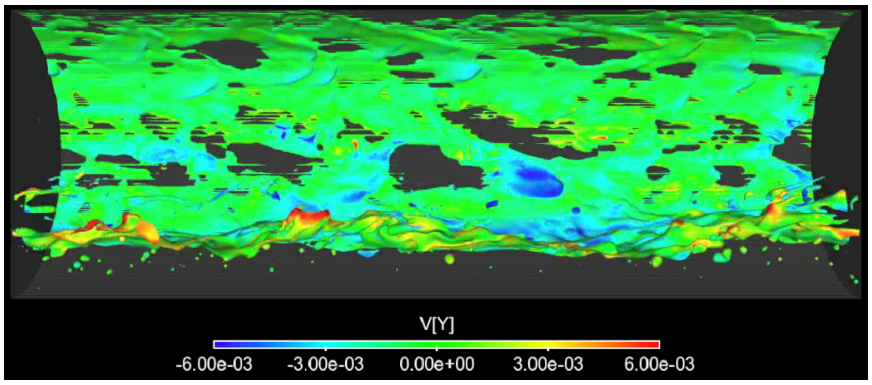

Figure 33: GS2 (lack of) wave pumping.

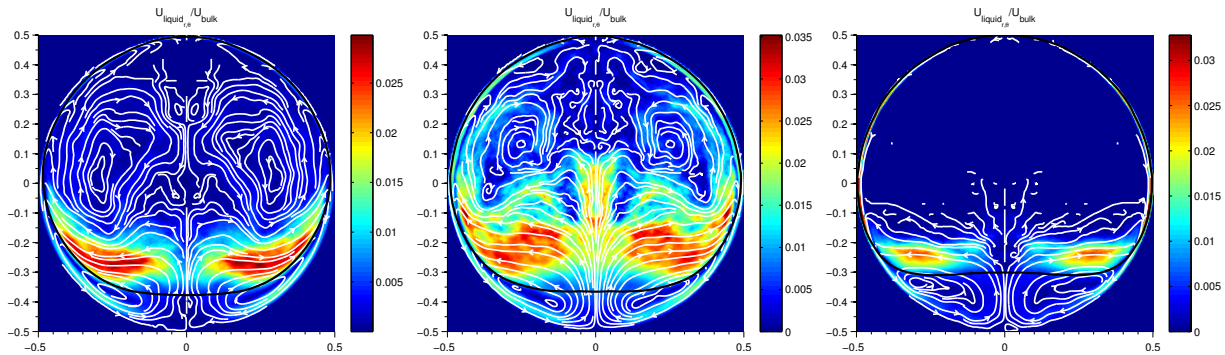

(a) SS1 orthoradial liquid streamlines.

(b) SS2 orthoradial liquid streamlines.

(c) GS2 orthoradial liquid streamlines.

Figure 34: Liquid streamlines demonstrating wave pumping mechanism.

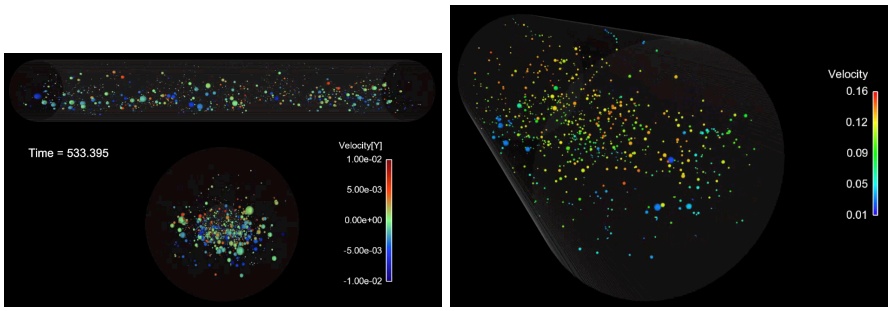

(a) SS2 droplet tracking.

(b) GS2 droplet tracking.

Figure 35: Droplets colored by vertical velocity (a) and velocity magnitude (b).

pipe are smaller, more work needs to be done to asses the implications for droplet entrainment and deposition.

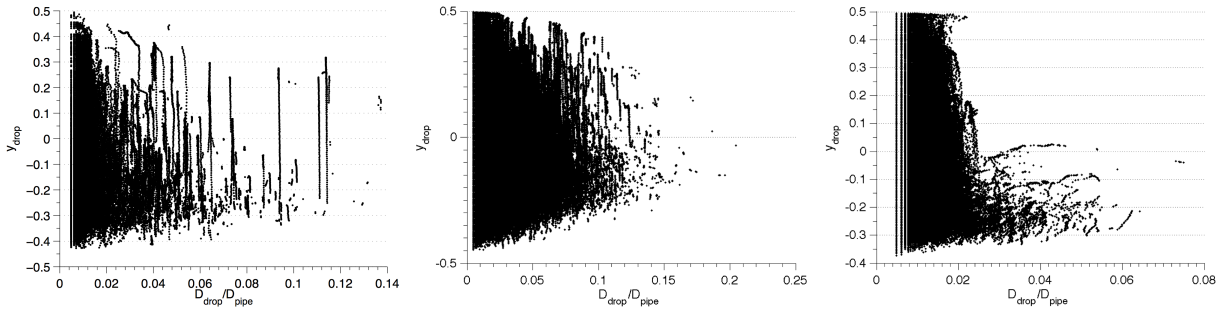

(a) SS1 scatter plot. (b) SS2 scatter plot. (c) GS2 scatter plot.

Figure 36: Scatter plots of drop vertical position verse drop diameter, normalized by pipe diameter.

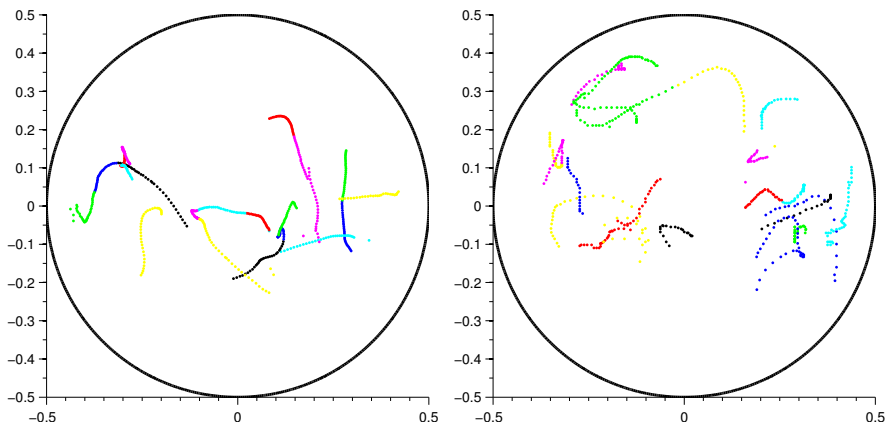

(a) 20 largest drop trajectories. (b) 20 smallest drop trajectories.

Figure 37: Trajectories of the 20 largest and 20 smallest drops in the domain. Different colors indicate different trajectories.

8 Conclusion

In summary, a state-of-the-art turbulent atomization/phase interface tracking code has been developed by our research group. This code has been used to produce simulations that are one of a kind, in that they have never been done before with respect to the physical problem, much less simulated at such large scales. High performance computing has captured the fundamental physics of gas-liquid flows through horizontal pipes, leading to new potential for regime characterization (Froude number). Readily available in our simulations is information regarding flow regime, film thickness, friction losses at the wall, probability of dry-out, and mechanisms for film sustainment (counter-rotating vortices, wave pumping, droplet entrainment and deposition, etc.). A strong platform has been laid for studying DSG and developing further models for heat and mass transfer and multiphase turbulence in the context of non-uniform heat flux in a cylindrical geometry, given the continuation of the current effort.

8.1 Summary of literature findings

A survey of literature has revealed that most work done today falls under two assumptions or models: the homogeneous flow model and the separated flow model. The main premise of the homogeneous flow model is that the vapor and liquid phases have the same velocities, allowing the two-phase flow to behave like a single phase with fluid properties that are the thermodynamic average of two phases. Obviously, this assumption becomes problematic when there is much disparity between the phases present in the flow. The annular flows we have been simulating are quite different from the limited circumstances for which the homogeneous assumption is a valid one: namely flows near the critical point when the fluid properties differ only slightly, or when the velocity difference between the phases is small (such as in bubbly flow or mist flow).

Much of the early quantification of annular flows relies on the use of flow regime maps, a thorough review of which can be found in the literature review of this paper. The literature suggests that the most predominant maps used are those of Taitel and Dukler [16], which uses the Martinelli factor on the horizontal axis and different transition parameters on the vertical axis, and Ghajar and Tang [41], which uses the superficial phase Reynolds numbers as the coordinate axis. The important thing to remember when using the Taitel and Dukler map is that although it does provide a quantitative approach to determining the regime of a particular flow, it also involves observation of the flow, which requires subjective input from the user. This approach and the transition parameters used in the Taitel and Dukler map are not very physically intuitive, which is likely a result of the complexity of the system. More specifically for annular flow, this was part of the motivation for seeking to understand more fundamentally the physical and competing processes that govern the "annularity" of the flow.

8.2 Summary of numerical approach

The scarcity of numerical work in the literature pertaining to gas-liquid horizontal pipe flow is likey attributed to the complexity of the system. The approach in the current study has been to use the NGA code [1], which implements arbitrarily high-order accurate fully conservative finite difference schemes that are both robust and accurate. The second-order version of the schemes is used in discretizing the governing equations for the present work. These second order schemes for the fluids equations are combined with the ghost-fluid method (GMF) [46] for handling discontinuities in fluid properties and the Discontinuous Galerkin Conservative Level Set (DG-CLS) for tracking the interface between the liquid and gas. This methodology relies on the Accurate Conservative Level Set (ACLS) [49] technique, combined with the improved accuracy of the quadrature-free discontinuous Galerkin discretization [50]. This method is ideal for the present work in that it is very accurate, conserves mass excellently, and scales well on parallel platforms.

The numerical techniques described above are one-of-a-kind and have been applied to periodic sections of pipe over which the flow quality and fluid properties can be approximated as constant, allowing us to perform simulations in the absence of heat and phase transfer. With this simplification, we have produced physically accurate results that are applicable to the DSG loop for the range in which the input parameters are provided. The simulations contain information that to date has not been shown numerically and is useful in the initial understanding of the hydrodynamic characteristics of the flow.

8.3 Summary of results

Data has been extracted from five different simulations that is relevant to both the high and low pressure DSG scenarios. The NGA code has provided information about the hydrodynamic properties of the gas-liquid flow, one of the most basic pieces being the relative locations of the phases within the pipe. Although the Reynolds numbers attained are much lower than those of the actual system, they are high enough that the statistical behavior of the system could be independent of Reynolds number. Thus, our findings are directly relevant to the DSG application.

One of the key findings for DSG is that the low pressure case falls into a higher likelihood of finding dry-out conditions in the upper regions of the pipe, and is therefore more likely to experience damage to operating equipment due to overheating. This has been explained through the Froude number, which is a measure of the ratio of the inertial forces sustaining the liquid to the gravitational forces draining it. This in itself is a new approach to regime characterization that is based on dimensional analysis and has firm physical reasoning from first principles. In contrast to the low pressure case, the high pressure case has a much lower probability of finding dry-out conditions at the pipe wall due to the contiguousness of the film. Dimensional analysis shows that the Froude number for the high pressure case is much larger, meaning that the forces that keep the film near the top are greater than those that drain it.

From the simulation data it is possible to compute many quantities that are important to Abengoa. Readily available to us is information regarding flow regime, mean thickness of the liquid film, pressure drop, frictional losses at the wall, and probability of dry-out. Effort has also been put towards investigating mechanisms of liquid sustainment, and results show that secondary gas flow and wave pumping action both contribute to the contiguousness of the film in the high pressure case. More information regarding droplet trajectories needs to be computed before anything conclusive can be said about whether or not droplet entrainment and deposition contributes to film replenishment.

8.4 Limitations and future work

The code in its current state is mainly limited by two things: the presence of heat transfer/phase change and the scales of the physical problem. Both of these limiting factors are surmountable given the advancement of the current project. The Computational Thermofluids Laboratory (CTFLab) at Cornell University has recently hired a post-doctoral researcher, experienced in gas-liquid interfaces in the presence of thermal fluctuations [64], to work on an evaporation model in the presence of nonuniform heating. This work will be essential in aiding the development of a model for gas-liquid flows with a non-uniform heat flux at the pipe walls.

The second issue is one of scale, which is standard in turbulent flows. The high Reynolds numbers mean that the disparity between the largest and smallest scales is large, making the flow computationally difficult to resolve. As discussed previously during the term of this project, Large-Eddy Simulation of the problem is an option, but more knowledge of the two-phase character of the flow is required before accurate sub-grid scale models can be built. A benchmark DNS to serve as a comparison for LES results is essential. Once validated, the use of an LES model will allow for simulation of much larger sections of DSG tubing and/or much higher Reynolds numbers.

Much like we have been doing currently with smaller sections of tubing, local flow conditions at different sections along the loop provided by Abengoa will be used as input conditions to the LES code, providing all of the aforementioned information (pressure drop, dry-out probability, mean

film height, etc.) for that section of the loop. Integrating pressure drop, for example, over each section of the loop would provide the predicted pressure drop for the entire DSG loop. Transient conditions in the reflector field, due to lack of sunlight or other reasons, may be investigated by driving the converged flow from one statistically stationary state to a different one (with different input parameters) and examining the transient between the two.

9 References

[1] O. Desjardins, G. Blanquart, G. Balarac, H. Pitsch, High order conservative finite difference scheme for variable density low mach number turbulent flows, J. Comp. Phys. 227 (15) (2008) 7125–7159.

[2] S. I. Kosterin, An investigation of the influence of the diameter and inclination of a tube on the hydraulic resistance and flow structure of gas-liquid mixtures, Izvest. Akad. Nauk. SSSR, Otdel Tekh Nauk 12.

[3] G. E. Alves, Cocurrent liquid-gas flow in a pipe-line contactor, Chem. Eng. Prog 50 (9) (1954) 449–456.

[4] O. Baker, Designing for simultaneous flow of oil and gas, Oil and Gas Journal 53 (1954) 185–195.

[5] L. I. Krasiakova, Some characteristics of the flow of a two-phase mixture in a horizontal pipe, Zhur. Tekh. Fiz 12 (1952) 654–669.

[6] C. J. Hoogendoorn, Gas-liquid flow in horizontal pipes, Chemical Engineering Science 9 (4) (1959) 205–217.

[7] V. Kadambi, Stability of annular flow in horizontal tubes, International Journal of Multiphase Flow 8 (4) (1982) 311–328.

[8] G. Tryggvason, B. Bunner, A. Esmaeeli, D. Juric, N. Al-Rawahi, W. Tauber, J. Han, S. Nas, Y. J. Jan, A Front-Tracking method for the computations of multiphase flow, Journal of Computational Physics 169 (2) (2001) 708–759.

[9] O. Desjardins, Numerical methods for liquid atomization and application in detailed simulations of a diesel jet, Ph.D. thesis, Stanford University, Stanford, CA (Jun. 2008).

[10] R. T. Lahey Jr., On the direct numerical simulation of two-phase flows, Nuclear Engineering and Design 239 (5) (2009) 867–879.

[11] R. I. Issa, M. H. W. Kempf, Simulation of slug flow in horizontal and nearly horizontal pipes with the two-fluid model, International journal of multiphase flow 29 (1) (2003) 69–95.

[12] M. Bonizzi, R. I. Issa, On the simulation of three-phase slug flow in nearly horizontal pipes using the multi-fluid model, International Journal of Multiphase Flow 29 (11) (2003) 1719–1747.

[13] M. Bonizzi, R. I. Issa, A model for simulating gas bubble entrainment in two-phase horizontal slug flow, International Journal of Multiphase Flow 29 (11) (2003) 1685–1717.

[14] J. M. Rodriguez, Numerical simulation of two-phase annular flow.

[15] J. M. Mandhane, G. A. Gregory, K. Aziz, A flow pattern map for gas–liquid flow in horizontal pipes, International Journal of Multiphase Flow 1 (4) (1974) 537–553.

[16] Y. Taitel, A. E. Dukler, A model for predicting flow regime transitions in horizontal and near horizontal gas-liquid flow, AIChE Journal 22 (1) (1976) 47–55.

[17] Gas-liquid flow, http://www.thermopedia.com/toc/chapt_g/GAS-LIQUID_FLOW.html.

[18] V. P. Carey, Liquid-vapor phase-change phenomena: an introduction to the thermophysics of vaporization and condensation processes in heat transfer equipment, Taylor and Francis, 2008.

[19] R. W. Lockhart, R. C. Martinelli, Proposed correlation of data for isothermal two-phase, two-component flow in pipes, Chem. Eng. Prog 45 (1) (1949) 39–48.

[20] C. D. G. King, Heat transfer and pressure drop for an Air-Water mixture flowing in a 0.737 inch ID horizontal tube, Ph.D. thesis, MS Thesis, University of California, Berkeley, CA (1952).

[21] M. Ishii, Thermo-fluid dynamic theory of two-phase flow, Eyrolles, 1975.

[22] J. J. Ginoux, Two-phase flows and heat transfer with application to nuclear reactor design problems, Hemisphere Pub. Corp., 1978.

[23] W. H. McAdams, W. K. Woods, R. L. Bryan, Vaporization inside horizontal tubes-II-benzene-oil mixtures, Trans. ASME 64 (3) (1942) 193–200.

[24] D. Chisholm, A. D. K. Laird, Two-phase flow in rough tubes, Trans. ASME 80 (2) (1958) 276–286.

[25] D. Butterworth, A comparison of some void-fraction relationships for co-current gas-liquid flow, International Journal of Multiphase Flow 1 (6) (1975) 845–850.

[26] R. C. Martinelli, D. B. Nelson, Prediction of pressure drop during forced circulation boiling of water, Recent advances in heat and mass transfer (1961) 3–18.

[27] C. J. Baroczy, SYSTEMATIC CORRELATION FOR TWO-PHASE PRESSURE DROP., in: Chem. Eng. Progr., Symp. Ser., 62: No. 64, 232-49 (1966)., 1966.

[28] M. Eck, W. D. Steinmann, Modelling and design of direct solar steam generating collector fields, Journal of Solar Energy Engineering 127 (2005) 371.

[29] L. Friedel, Improved friction pressure drop correlations for horizontal and vertical two-phase pipe flow, in: European two-phase flow group meeting, Paper E, Vol. 2, 1979.

[30] S. Natan, D. Barnea, Y. Taitel, Direct steam generation in parallel pipes, International Journal of Multiphase Flow 29 (11) (2003) 1669–1683.

[31] J. Pye, G. Morrison, M. Behnia, Pressure drops for direct steam generation in line-focus solar thermal systems.

[32] P. Spedding, E. Benard, G. Donnelly, Prediction of pressure drop in multiphase horizontal pipe flow, International Communications in Heat and Mass Transfer 33 (9) (2006) 1053–1062.

[33] R. Pletcher, H. McManus Jr., Heat transfer and pressure drop in horizontal annular two-phase, two-component flow, International Journal of Heat and Mass Transfer 11 (7) (1968) 1087–1104.

[34] J. Wurtz, et al., An experimental and theoretical investigation of annular steam-water flow in tubes and annuli at 30 to 90 bar, RISO report 372.

[35] G. K. Batchelor, Collected Works of GI Taylor, Cambridge University Press, 1958.

[36] G. I. Taylor, Generation of ripples by wind blowing over a viscous fluid, The Scientific Papers of GI Taylor (1962) 244–254.

[37] D. Kim, A. J. Ghajar, R. L. Dougherty, V. K. Ryali, Comparison of 20 two-phase heat transfer correlations with seven sets of experimental data, including flow pattern and tube inclination effects, Heat Transfer Engineering 20 (1) (1999) 15–40.

[38] D. Kim, A. J. Ghajar, R. L. Dougherty, Robust heat transfer correlation for turbulent gas-liquid flow in vertical pipes, Journal of Thermophysics and Heat Transfer 14 (4) (2000) 574–578.

[39] D. Kim, A. J. Ghajar, Heat transfer measurements and correlations for air-water flow of different flow patterns in a horizontal pipe, Experimental Thermal and Fluid Science 25 (8) (2002) 659–676.

[40] J. Kim, A. J. Ghajar, A general heat transfer correlation for non-boiling gas-liquid flow with different flow patterns in horizontal pipes, International Journal of Multiphase Flow 32 (4) (2006) 447–465.

[41] A. J. Ghajar, C. C. Tang, Heat transfer measurements, flow pattern maps, and flow visualization for Non-Boiling Two-Phase flow in horizontal and slightly inclined pipe, Heat Transfer Engineering 28 (6) (2007) 525–540.

[42] C. E. Dengler, J. N. Addoms, Heat transfer mechanism for vaporization of water in a vertical tube, in: Chemical Engineering Progress Symposium Series, Vol. 52, 1956, pp. 95–103.

[43] S. A. Guerrieri, R. D. Talty, A study of heat transfer to organic liquids in Single-Tube, natural circulation, vertical tube boilers, in: Chemical Engineering Progress Symposium Series, Vol. 52, 1956, pp. 69–77.

[44] L.-s. Tong, Y. S. Tang, Boiling heat transfer and two-phase flow, Taylor & Francis, 1997.

[45] P. Spedding, D. Spence, Flow regimes in two-phase gas-liquid flow, International Journal of Multiphase Flow 19 (2) (1993) 245–280.

[46] R. P. Fedkiw, T. Aslam, B. Merriman, S. Osher, A non-oscillatory eulerian approach to interfaces in multimaterial flows (the ghost fluid method), J. Comput. Phys. 152 (2) (1999) 457–492.

[47] M. Sussman, K. M. Smith, M. Y. Hussaini, M. Ohta, R. Zhi-Wei, A sharp interface method for incompressible two-phase flows, J. Comput. Phys. 221 (2) (2007) 469–505.

[48] O. Desjardins, H. Pitsch, A spectrally refined interface approach for simulating multiphase flows, Journal of Computational Physics 228 (5) (2009) 1658–1677.

[49] O. Desjardins, V. Moureau, H. Pitsch, An accurate conservative level set/ghost fluid method for simulating turbulent atomization, J. Comp. Phys. 227 (18) (2008) 8395–8416.

[50] M. F. Czajkowski, O. Desjardins, A discontinuous galerkin conservative level set scheme for simulating turbulent primary atomization, Ventura, CA, 2011.

[51] H. Luo, L. Luo, R. Nourgaliev, V. A. Mousseau, N. Dinh, A reconstructed discontinuous galerkin method for the compressible Navier-Stokes equations on arbitrary grids, J. Comp. Phys. 229 (19) (2010) 6961–6978.

[52] M. M. Francois, S. J. Cummins, E. D. Dendy, D. B. Kothe, J. M. Sicilian, M. W. Williams, A balanced-force algorithm for continuous and sharp interfacial surface tension models within a volume tracking framework, Journal of Computational Physics 213 (1) (2006) 141 – 173.

[53] J. A. Sethian, Level set methods and fast marching methods: evolving interfaces in, Cambridge University Press, 1999.

[54] R. Scardovelli, S. Zaleski, Direct numerical simulation of free-surface and interfacial flow, Annu. Rev. Fluid Mech. 31 (1) (1999) 567–603.

[55] M. Rudman, Volume-tracking methods for interfacial flow calculations, Int. J. Numer. Meth. Fl. 24 (7) (1997) 671–691.

[56] M. Raessi, A level set based method for calculating flux densities in two-phase flows., CTR An. Res. Briefs (2008) 467.

[57] M. Raessi, P. Pitsch, Modeling interfacial flows characterized by large density ratios with the level set method, CTR An. Res. Briefs (2009) 156.

[58] O. Desjardins, G. Blanquart, G. Balarac, H. Pitsch, High order conservative finite difference scheme for variable density low mach number turbulent flows, Journal of Computational Physics 227 (15) (2008) 7125–7159.

[59] O. Desjardins, R. Fox, P. Villedieu, A quadrature-based moment method for dilute fluid-particle flows, Journal of Computational Physics 227 (4) (2008) 2514–2539.

[60] B. J. McKeon, C. J. Swanson, M. V. Zagarola, R. J. Donnelly, A. J. Smits, Friction factors for smooth pipe flow, Journal of Fluid Mechanics 511 (2004) 41–44.

[61] S. B. Pope, Turbulent Flows, Cambridge University Press, 2008.

[62] D. Butterworth, Air–water annular flow in a horizontal tube, 1972.

[63] T. Fukano, A. Ousaka, Prediction of the circumferential distribution of film thickness in horizontal and near-horizontal gas-liquid annular flows, International journal of multiphase flow 15 (3) (1989) 403–419.

[64] P. T. Brady, M. Herrmann, J. M. Lopez, Confined thermocapillary motion of a three-dimensional deformable drop, Phys. Fluids 23.

A Opportunities for future collaboration

A.1 Questions from Abengoa Solar

Q: What are the current limitations of the code?
With respect to the DSG application, the NGA code currently has two limitations:

- Isothermal conditions are assumed in order to facilitate the simulation of turbulent liquid-gas flows. Note that NGA is not an isothermal code, it is regularly used to compute flames. It can solve an energy equation as well as mass fraction transport equations, hence it is fully capable of handling heat and mass transfer. However, simulating fully resolved gas-liquid flows under boiling conditions leads to specific challenges, such as the presence of a discontinuous velocity field. To this day, no numerical method has been proven to be accurate and scalable for simulating turbulent boiling two-phase flows. We believe that we are uniquely equipped to solve this challenge and propose such a method, and therefore we propose to make this task one of the focal point of the future project. Toward this goal, we have already developed and tested a methodology for handling discontinuous velocity fields (Pepiot and Desjardins, Proceedings of the Center for Turbulence Research Summer Program 2010, Stanford University), and we have recently hired a post-doctoral researcher (Dr. Peter Brady) who will focus on this topic.

- NGA is not capable of reaching the full DSG operating conditions at this time. In particular, the Reynolds number is out of reach for our approach. In this report, the distinctions between direct numerical simulation (DNS) and large-eddy simulation (LES) were discussed. So far, we have performed DNS, which can be described as numerical experiments insofar that no closure model is necessary. While very accurate, this approach is extremely costly, and for this reason the values of Reynolds number relevant to DSG cannot be reached. The classical solution to this problem is to use LES, where physical models are introduced to represent the smallest scales in the flow, which then need not be resolved. NGA is fundamentally an LES code, and has been shown to be ideally suited to perform this type of simulations. However, the DSG problem has the particularity of exhibiting a pipe boundary layer that contains a liquid film. No model exists for such a configuration in the scientific literature. Moreover, this feature is key to the DSG flow, and therefore it cannot simply be ignored. Consequently, we propose to make the development of such a liquid film wall model the second focus of our future research effort, using the data generated already for guidance and validation.

Q: What information can these simulations provide regarding the entire loop?
Given the limitations described above, we have focused so far on simulating isothermal sections of pipe that match all relevant DSG parameters except for the Reynolds number. If provided with a set of relevant conditions at a given position along the length of the pipe, such simulations are capable of predicting the nature of the flow field in great details. Directly accessible are the flow regime, wall friction, mean velocity profiles, and dry-out probability. Such information has been presented for different conditions in this report. In turn, information about friction can be used to derive detailed correlations that can be useful in one-dimensional models.

Assuming further work on boiling conditions and LES wall film modeling, we could significantly extend the range of data that can be extracted. In particular, we could simulate very long sections of pipe under transient conditions. Full loops will remain out of reach, but simulations of several

meters of pipe length will become possible with LES. In addition, spatial evolution in quality due to phase change will be accounted for explicitly, providing a comprehensive understanding of pressure losses and dry-out conditions. Transient scenarios such as temporal or spatial variation in cloud coverage will become readily testable to better understand optimal operating conditions.

Q: What information can these simulations provide regarding reflector field transients?
While our work so far has focused on stationary conditions, moving towards non-isothermal LES will enable NGA to simulate spatially and temporally transient pipe flows. Transient conditions in the reflector field, due to lack of sunlight or other reasons, may be investigated by imposing a presumed heating rate as a function of the pipe location. Corresponding fluctuations in mass flow rate and film distributions will be a direct result of our simulations.

Q: What can be said regarding feedback from different loops?
System-scale models require reduced-order representations of individual components of the system. A Matlab/Simulink model of a DSG system could be developed based on *transfer functions* created by transient simulations as described above. Once it is understood how the flow rate and quality distribution in a single pipe line changes due to a change in heating conditions, this information can be simplified and presented in the form of a transfer function. Using simple ideas such as conservation of mass to couple multiple lines should allow to have a inexpensive dynamic model of the full DSG system with a sound physical basis.

A.2 Discussion

A.2.1 Limitations from heat and mass transfer

The code currently deals only with two phases in isothermal conditions, in the absence of phase change. Many of the flows studied by the Computational Thermo-Fluids Laboratory (CTFLab) at Cornell University involve the presence of two phases, often of the gas-liquid variety. Developing the tools necessary to study unsteady, non-uniform heating of the DSG carrier fluid is directly in line with the mission of CTFLab. In fact, a post-doctoral researcher with experience in gas-liquid interfaces in the presence of thermal fluctuations has recently been hired to begin developing an evaporation model in the presence of non-uniform heating. This work will be in direct support of expanding the toolset for accurate DSG simulation.

A.2.2 Proposal for a wall/film LES model

The evaporation model discussed above will be combined with multiphase turbulence models to generate LES that can reach arbitrarily high Reynolds numbers and long sections of tubing. The basis of the model will be the momentum integral equation

$$\frac{d}{dx}\left(U_g^2\theta\right) + \delta^* U_g \frac{dU_g}{dx} = \frac{\tau_w}{\rho_g}\,, \tag{106}$$

where U_g is the gas flow obtained from the solution to a LES in the region outside the boundary layer, θ is the momentum thickness, δ^* is the displacement thickness, and τ_w is the shear stress at the wall (see Fig. 38). Equation (106) is obtained from integrating the axial (x) momentum equation in the wall-normal direction. In this model, θ, δ^*, and τ_w are not known: they are provided based on information about the liquid film height $h(x, y, t)$ and bulk film velocity $U_l^b(x, y, t)$.

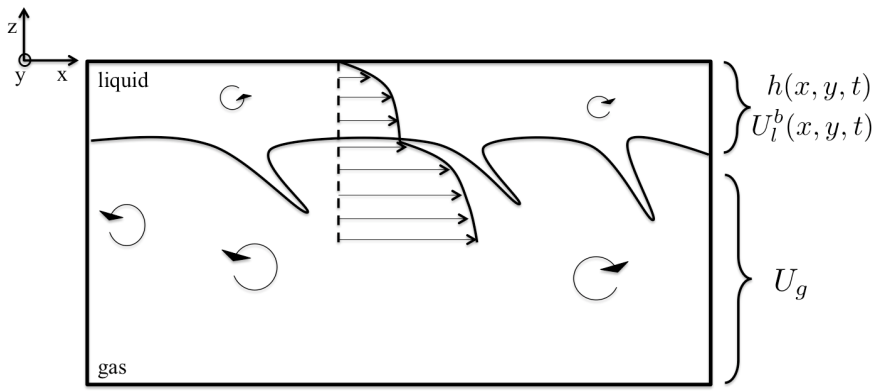

LES

Figure 38: Schematic demonstrating the proposed model based on the momentum integral equation.

To develop this model, existing DNS data generated in the completed project will be instrumental. The integral balance equation written above will be analyzed in details using both pipe DNS and simpler, more refined simulations of two-phase turbulent boundary layers (TPTBL). Such a TPTBL simulation is described in Appendix B. Use of this model will allow us to simulate significantly longer sections of pipe (several hundred times the pipe diameter) and extract hydrodynamic and thermal properties.

A.3 Work plan and deliverables

Our proposal for future research on first-principle modeling of DSG is decomposed into three phases, estimated to each be year-long endeavors. This plan is preliminary and could be modified to satisfy external constraints. Note that possible deliverables and benefits to Abengoa Solar are highlighted for each phase.

- **Current situation**
  - Full DNS at lower Reynolds number conducted on short pipe sections, database available
  - Direct prediction of dry-out probability, friction at walls (pressure drop), flow regime
  - For example: our results suggest that the Golden case is much more likely to suffer from dry-out than the Spain case, despite the presence of a generally thicker film. Our results suggest that using a lower Reynolds number is unlikely to affect the validity of this prediction.

- **Phase 1** – Addressing the limitations of NGA

  A) Enable boiling conditions in NGA resolved two-phase flow simulations
     - Finalize methodology for solving discontinuous velocity fields
     - Test and validate stationary film boiling using experiments
     - Simulate boiling TPTBL at relevant conditions but lower Reynolds number

- Simulate boiling pipe flow at relevant conditions but lower Reynolds number

B) Develop and test isothermal LES wall/film model
   - Use existing DNS database to develop closure for postulated integral equation *a priori*
   - Validate LES strategy with DNS results *a posteriori*
   - Simulate very long, non-periodic, isothermal pipe sections at high Reynolds number

Deliverables

- Code capable of predicting flow regime, dry-out, and pressure losses at a given point along the tube given a set of local conditions at realistic Reynolds number under isothermal assumption
- Code capable of predicting flow regime, dry-out, and pressure losses at a given point along the tube given a set of local conditions at low Reynolds number without isothermal assumption

- **Phase 2** – Enabling a predictive, first-principle-based DSG simulation

A) Develop and test boiling LES wall/film model
   - Using boiling DNS database developed in Phase 1, modify previously developed wall/film model to account for phase change
   - Validate LES strategy with DNS results *a posteriori*

B) Conduct non-periodic LES of long pipe sections (several meters) with fully realistic conditions and boiling, validate with Abengoa field data

Deliverables

- Report on validation of boiling LES approach
- Code capable of predicting boiling flow regime, dry-out, and pressure losses for large fractions of pipe given operating conditions only, at realistic Reynolds number
- Extensive comparison with current Abengoa Solar reduced order models, possibly new correlations

- **Phase 3** – Transient and inter-loop effects

A) Conduct transient simulations in non-periodic sections with prescribed heating pattern (spatial and/or temporal)
   - Compare with stationary results in Phase 2

B) Reduce data in the form of loop transfer function suitable for system-level modeling

Deliverables

- Report on various transient scenarios, useful for proper design of DSG loops outside of nominal operating conditions
- Transfer functions for mass flow rate, pressure profile, dry-out probably as a function of pipe length for a given spatial or temporal heating signal on the pipe surface

A.4 Opportunity

Note that this work plan is preliminary – further discussion with Abengoa Solar is likely to lead to a refined proposal with higher relevance. While the proposed research is formidable in many aspects, we believe that we are uniquely positioned to conduct it, given our numerical capabilities, computational resources, experience in turbulent multiphase reacting flows, and strong dedication to the topic. The simulations presented in the report are already unique, in that nothing in the literature approaches the level of details that they provide. The proposed future effort will focus on bridging the gap between the current simulations and the engineering challenge facing Abengoa.

By supporting future research effort in the Computational Thermo-Fluids Lab at Cornell University, Abengoa Solar will also benefit from:

1. Our computational resources: a new 1,152 core supercomputer, dedicated to Dr. Desjardins' research.

2. Our computational platform NGA, which we license at a price to companies. NGA will be made available to Abengoa Solar's researchers, should they want to transition some of the technologies we are currently developing to their own laboratory.

3. Our new post-doctoral researcher, financed independently of this project, who is working on Phase 1-A already.

B Boundary layer simulation

B.1 Motivation

Although the contiguousness of the film is governed to a first approximation by the Froude number, it is conceivable that the void fraction α_g may also tie into this. In other words, the liquid may distribute itself differently within the pipe if there is significantly less of it available. Comparing Table 6 and Fig. 19, we see that the void fraction for the S2 case is 0.93 while simulations SS1 and SS2 have a void fraction of 0.85. As discussed previously, this is because because there would not be enough points in the liquid film to achieve proper resolution for an $\alpha_g = 0.93$ case based on our mesh size. Although this difference is not large (= 8.6%), it is worth investigating as the breaking of the film near $\theta/\pi = 1$ can lead to damage of operating equipment. In order to better examine the behavior of the thin film near the top of the pipe (where the onset of dryout, if applicable, takes place), it will be necessary to perform a refined simulation in this region.

B.2 Computational domain

The reason that the void fraction in simulations SS1 and SS2 does not match the void fraction from case S2 in the first place is because of resolution issues, so naturally we will not be able to simulate the entire pipe if we hope to match the proper value of α_g. What we have chosen to do is zoom in on a region near the top of the pipe centered at $\theta/\pi = 1$ and isolate a region that is approximated by a Cartesian box. This box is periodic in y (circumferencially) and x (axially), the width being 5 % of the pipe diameter, the depth being 15 % the pipe diameter, and the length being 3 times its depth. The box is long enough in the axial (x) direction to capture the largest-scale interfacial fluctuations, validating periodicity in this direction. Similarly, the width of the box is chosen to be narrow enough to allow us to use periodic conditions. The simulation is forced by prescribing a Dirichlet boundary condition in the velocity at the bottom of the box, the prescribed value obtained from the log-law. Figure 39 shows a properly scaled illustration of the pipe region we are simulating.

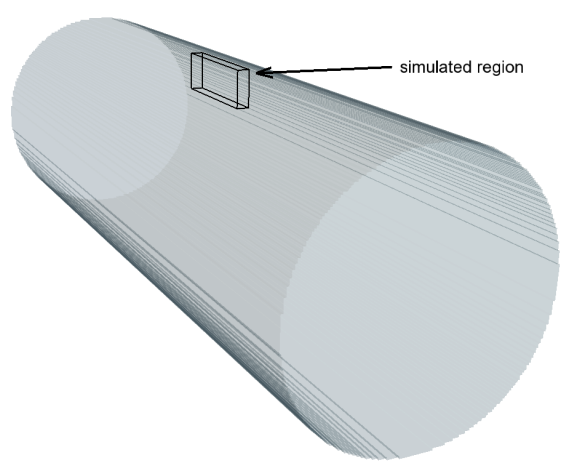

Figure 39: Illustration of the region included in the boundary layer simulation.

B.3 Results

Table 7 gives the parameters for the S2 case and the boundary layer (BL) simulation, demonstrating that the simulation matches the density ratio, viscosity ratio, Froude number, and void fraction of the actual S22 case.

Case	ρ_l/ρ_g	μ_l/μ_g	Re_g	We_g	Fr	α_g
Spain_2	15.99	4.62	1.31×10^6	1.75×10^4	3.28	0.93
BL simulation	15.99	4.62	25,000	7,000	3.28	0.93

Table 7: Parameters for S2 case and the BL simulation.

Figures 40 and 41 show still shots of the simulation once statistically stationarity has been reached: the breakup of the interface is shown in Fig. 40 while cuts of the $z-x$ and $z-y$ planes are shown in Figs. 41(a) and 41(b), respectively. Figure 42 shows the velocity magnitude and liquid volume fraction as a function of distance y from the wall.

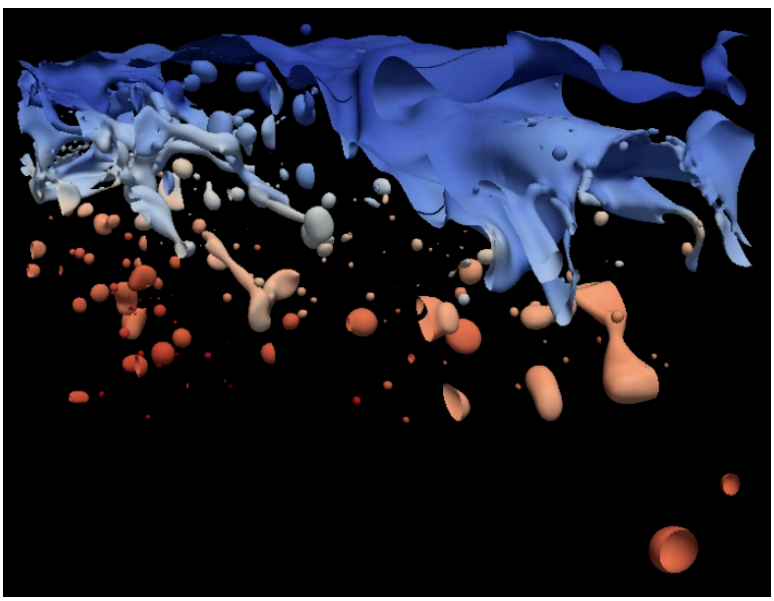

Figure 40: Breakup of the interface.

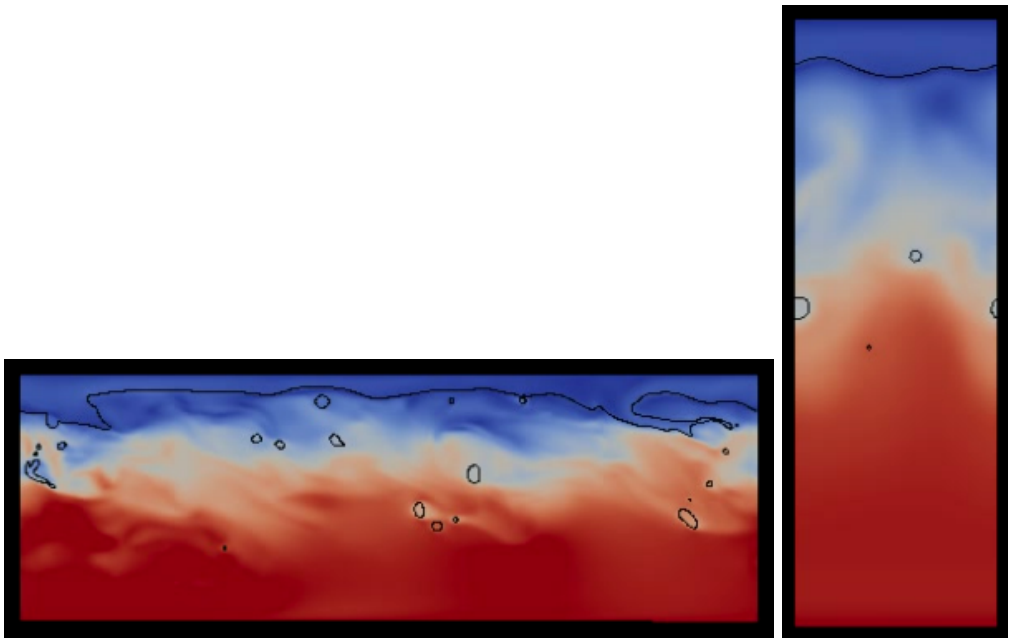

(a) A cut of the $z - x$ plane.

(b) A cut of the $z - y$ plane.

Figure 41: Visualization of the boundary layer simulation.

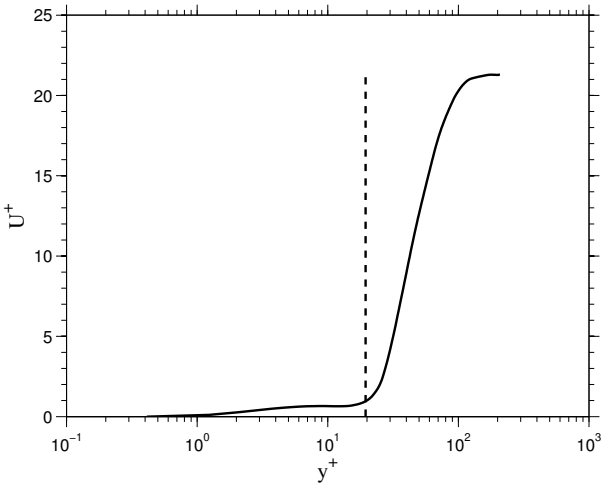

(a) $U^+(y^+)$ shown by (—), mean location of the interface h^+ shown by (– –).

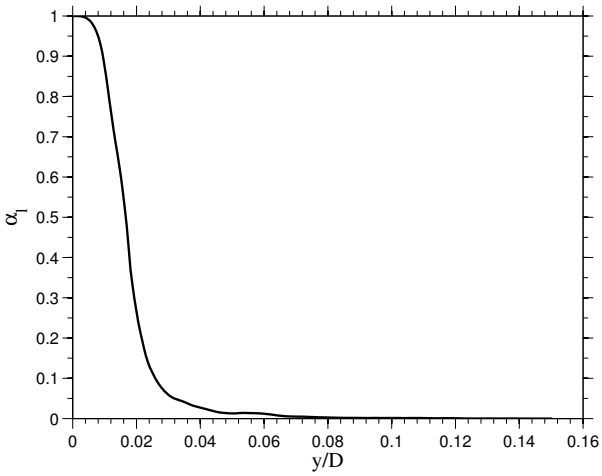

(b) $\alpha_l(y)$

Figure 42: Velocity and liquid volume fraction as a function of distance from the wall.

The velocity profile is shown in the traditional $^+$ units. The average distance of the interface from the wall in plus units is $h^+ = 19.51$, which corresponds to the change in profile of U^+ (see Fig. 42(a)). This value is compared to a value of $h^+ = 270.78$, which is the value obtained using the

actual gas Reynolds number and the void fraction correlation (assuming a uniform thickness). The probability of dry-out for this BL simulation was 0 %, meaning there is a contiguous film during the entire simulation. As simulating the actual value of α_g has not changed anything, we continue to assume that dry-out probability is governed by the Froude number and that this is decoupled from the Reynolds number and Weber number (which we are closer to, but still far from matching in this simulation). This suggests that the S2 case is a case in which dry-out should not be expected.

REV.	DESCRIPTION	APPROVED	DATE

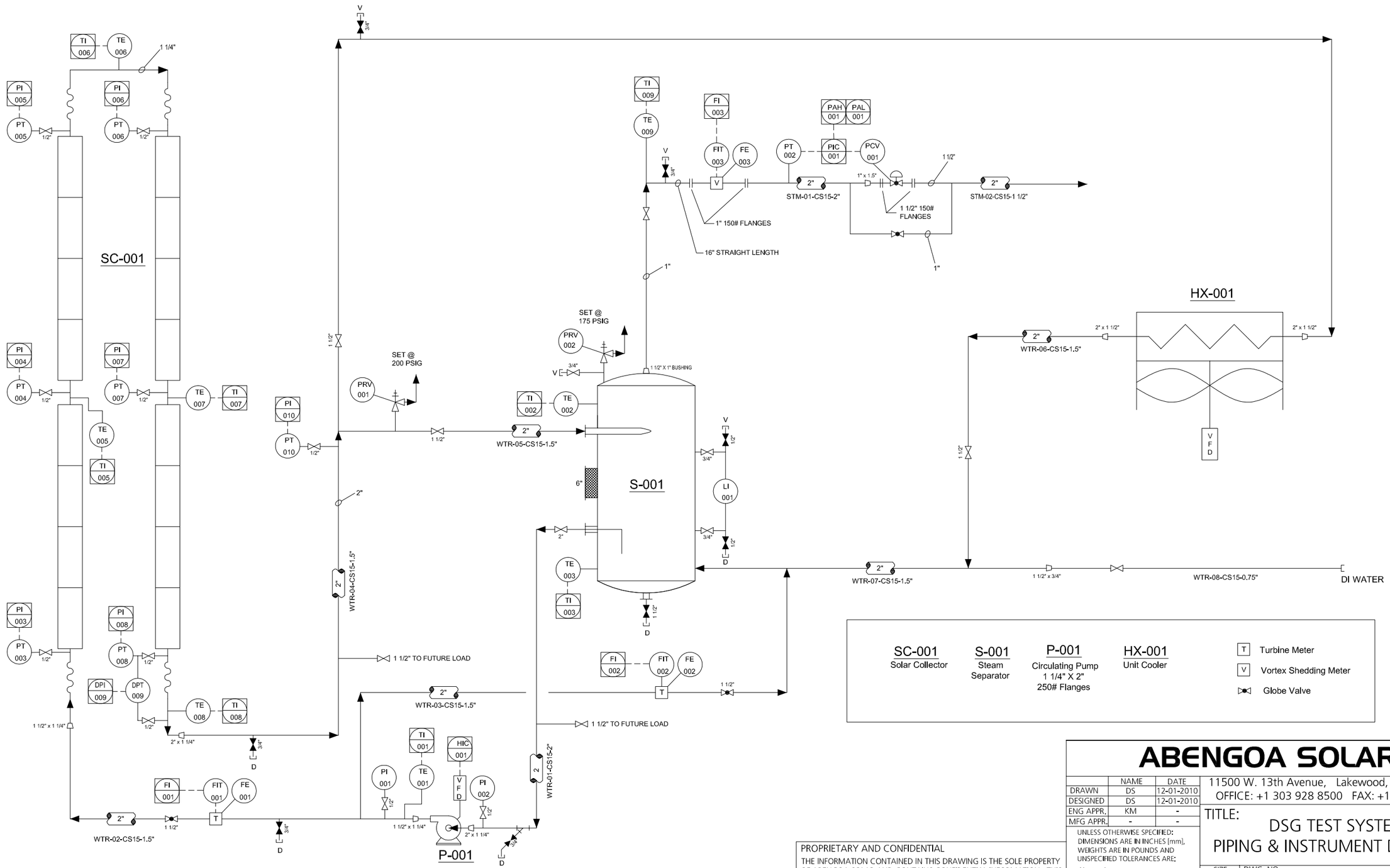

ABENGOA SOLAR

	NAME	DATE
DRAWN	DS	12-01-2010
DESIGNED	DS	12-01-2010
ENG APPR.	KM	-
MFG APPR.	-	-

UNLESS OTHERWISE SPECIFIED: DIMENSIONS ARE IN INCHES [mm], WEIGHTS ARE IN POUNDS AND UNSPECIFIED TOLERANCES ARE:
.X ± .1
.XX ± .03
.XXX ± .010
.XXXX ± .0005
ANGLE ± .5 DEG

11500 W. 13th Avenue, Lakewood, CO, USA 80215
OFFICE: +1 303 928 8500 FAX: +1 303 928 8510

TITLE:
DSG TEST SYSTEM
PIPING & INSTRUMENT DIAGRAM

SIZE	DWG. NO.	REVISION
B	4B1026-000014	-

SCALE: NONE WEIGHT: LBS SHEET 1 OF 1

PROPRIETARY AND CONFIDENTIAL
THE INFORMATION CONTAINED IN THIS DRAWING IS THE SOLE PROPERTY OF ABENGOA SOLAR AND CONTAINS CONFIDENTIAL INFORMATION. THIS DOCUMENT MAY NOT BE COPIED NOR MAY THE INFORMATION IT CONTAINS BE DISCLOSED UNLESS AUTHORIZATION IN WRITING IS PROVIDED BY ABENGOA SOLAR. ACCEPTANCE OF THIS DOCUMENT INDICATES AGREEMENT TO RECEIVE SUCH INFORMATION IN CONFIDENCE.

Appendix D: Results of DSG Experiments

Figure D-1: Temperatures and flow rate at 5.9 bar steam

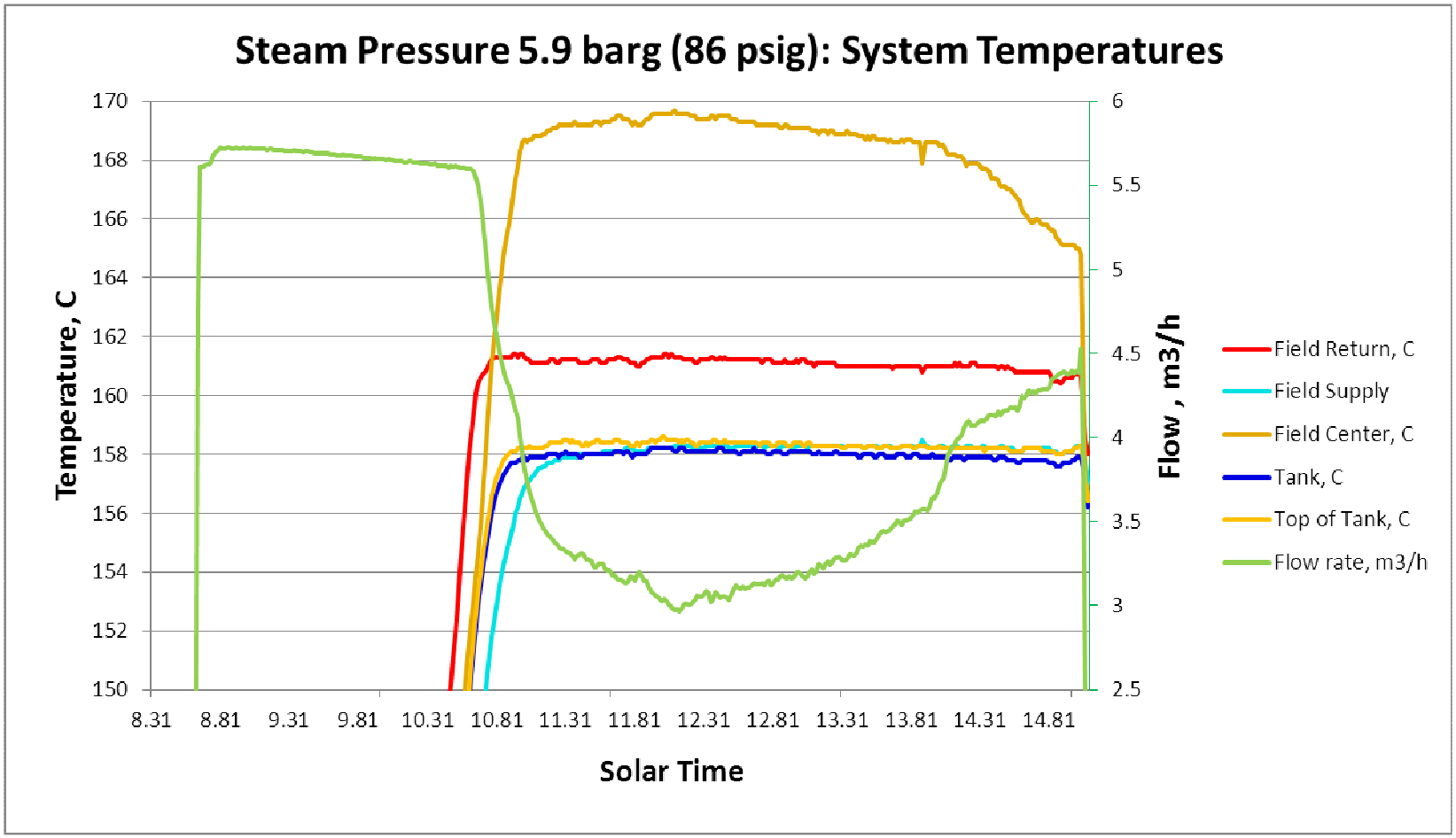

Figure D-2: Pressure and flow rate at 5.9 bar steam

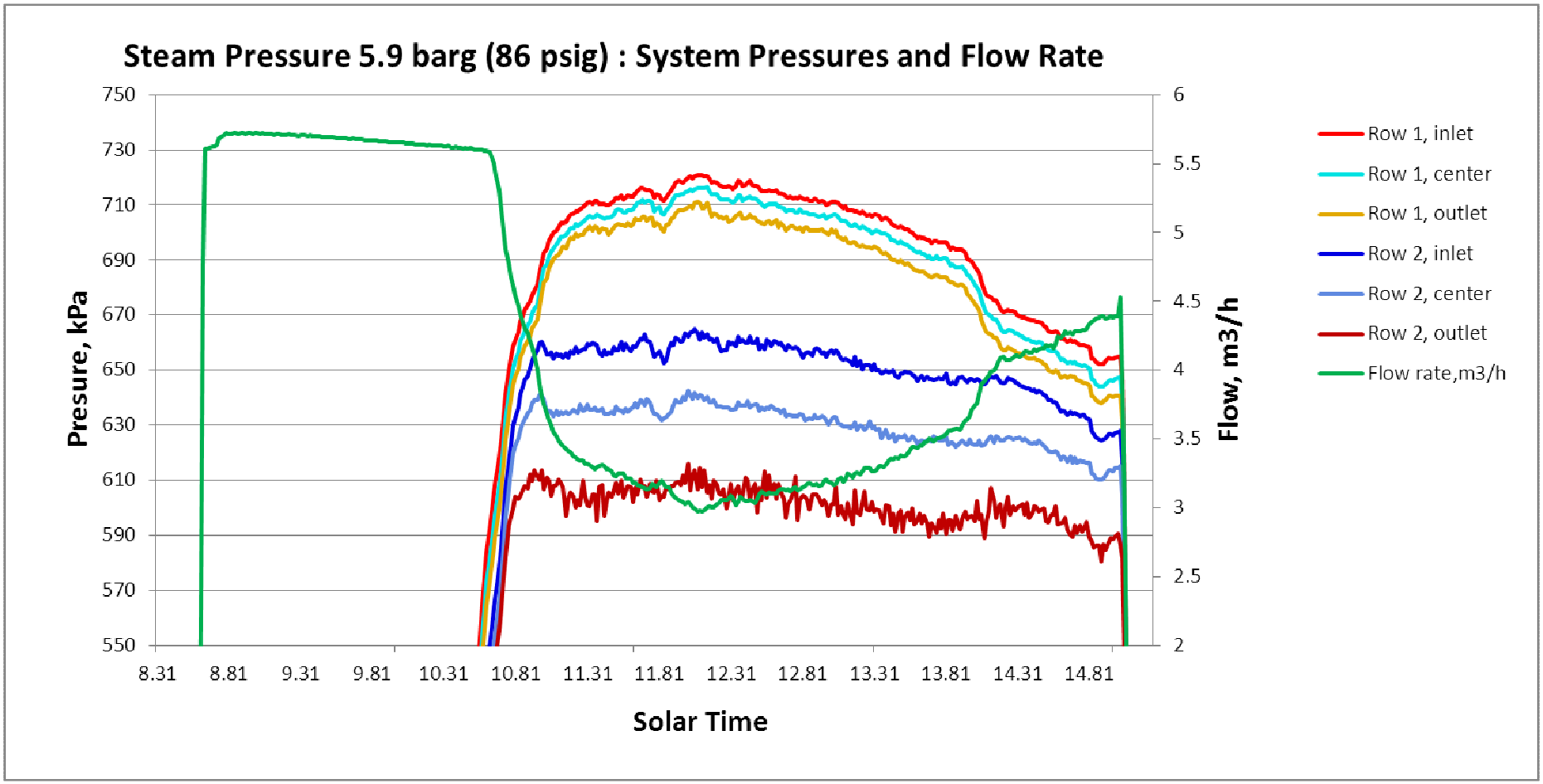

Figure D-3: Differential Pressure, Flow and Sun Intensity at 5.9 barg steam

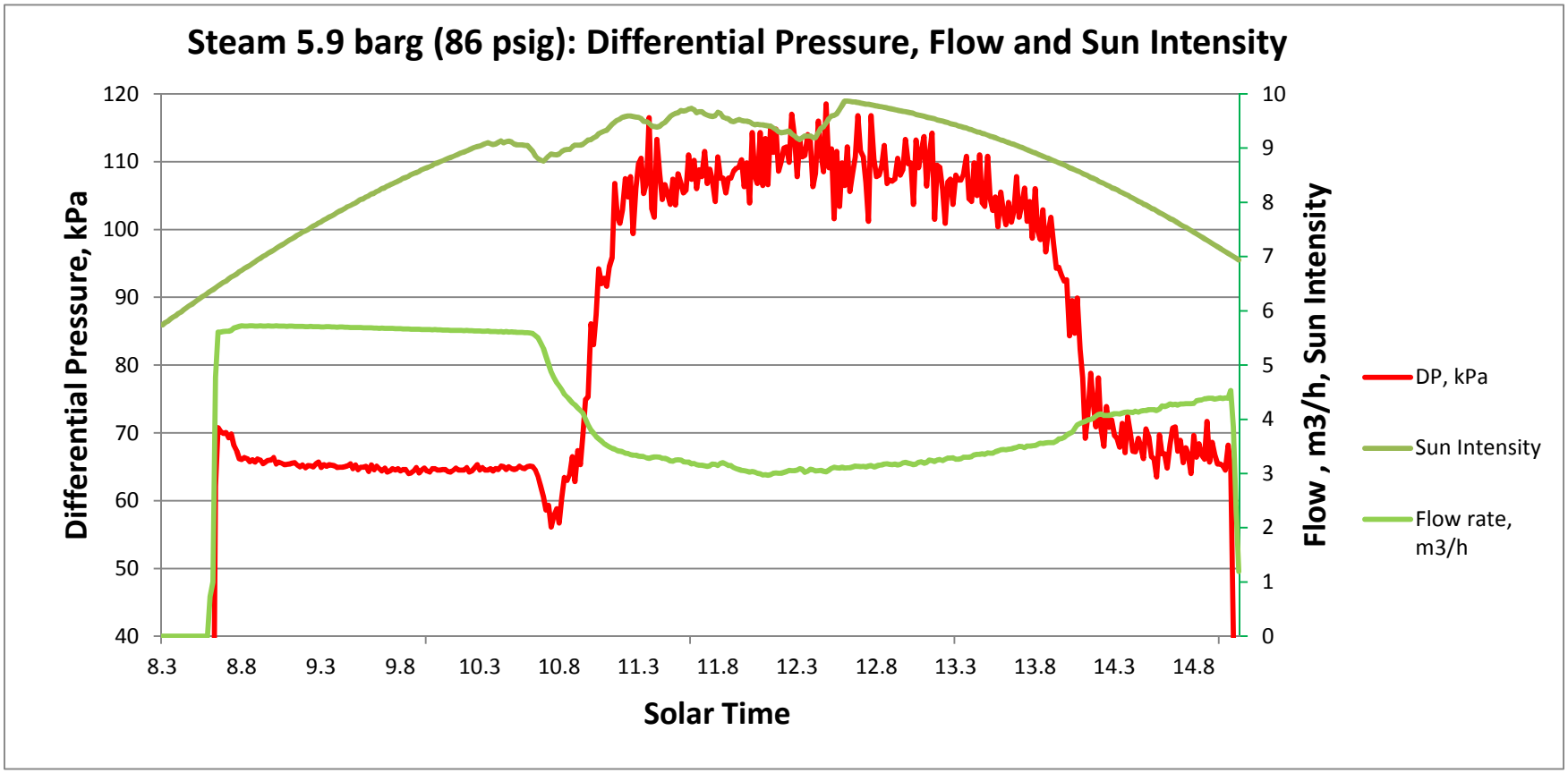

Figure D-4: Temperatures and flow rate at 8 bar steam

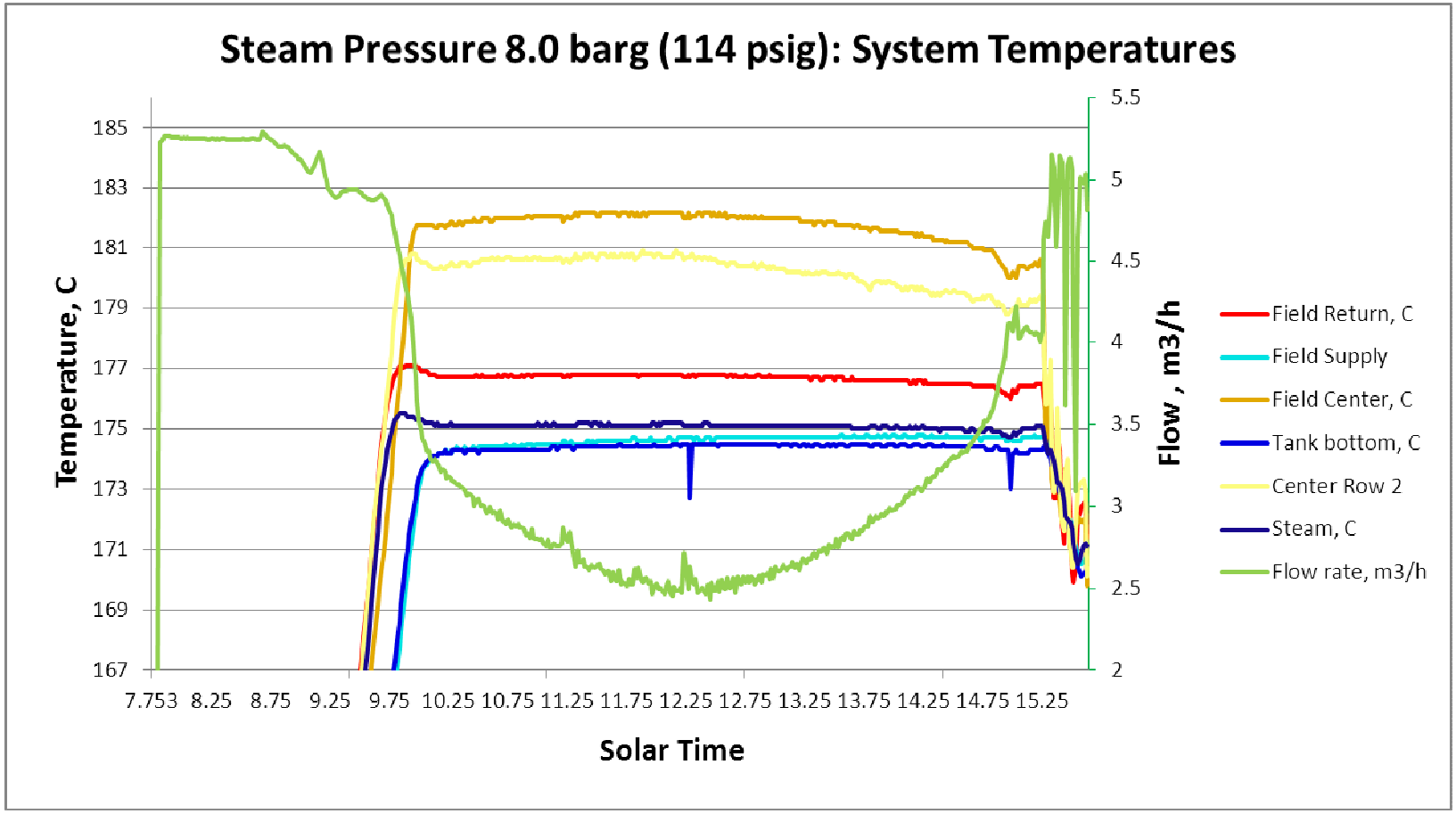

Figure D-5: Pressure and flow rate at 8 bar steam

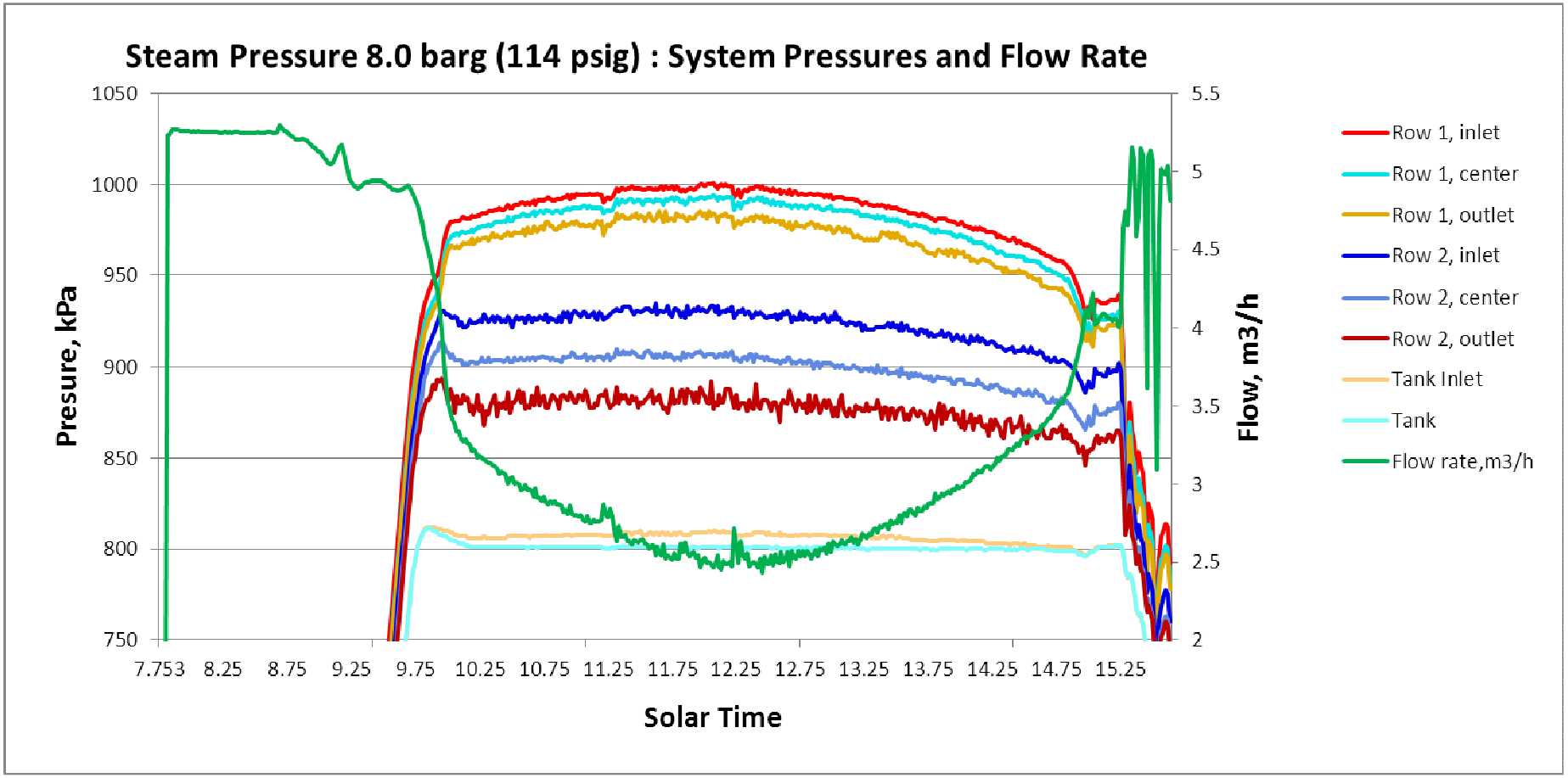

Figure D-6: Differential Pressure, Flow and Sun Intensity at 8 barg steam

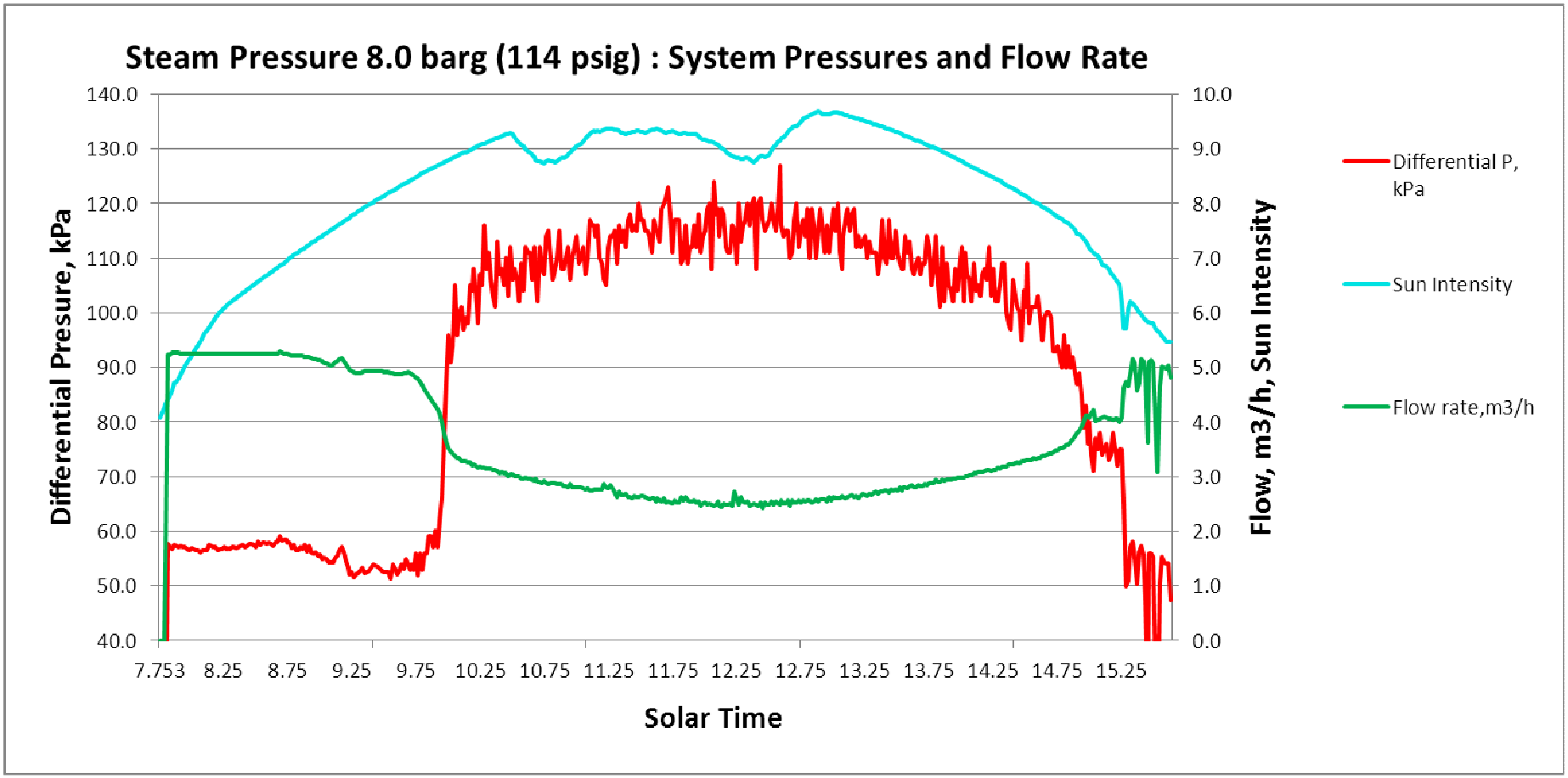

Figure D-7: Temperatures and Flow for steam at 9 and 10 bar

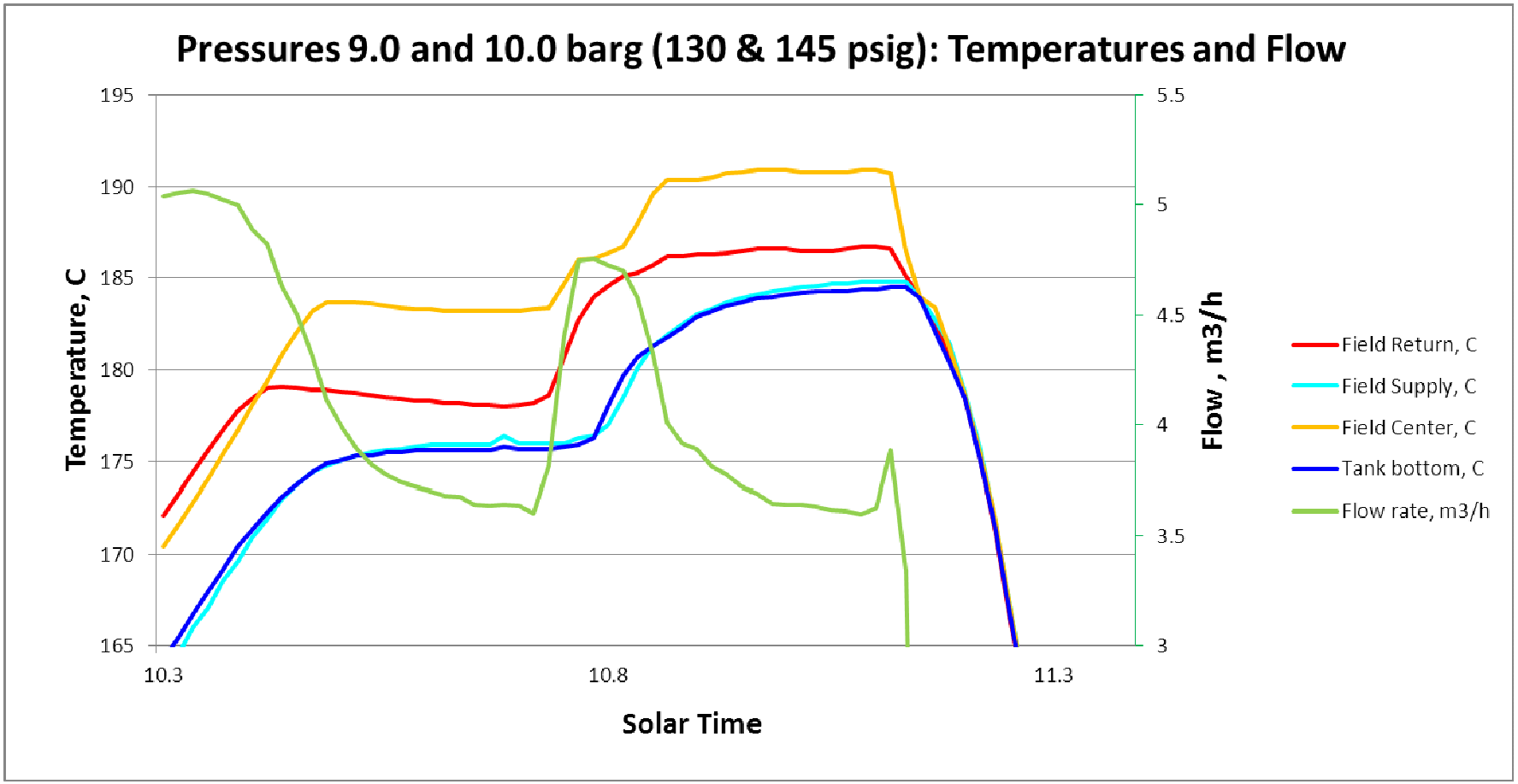

Figure D-8: Pressures and Flow for steam at 9 and 10 bar steam

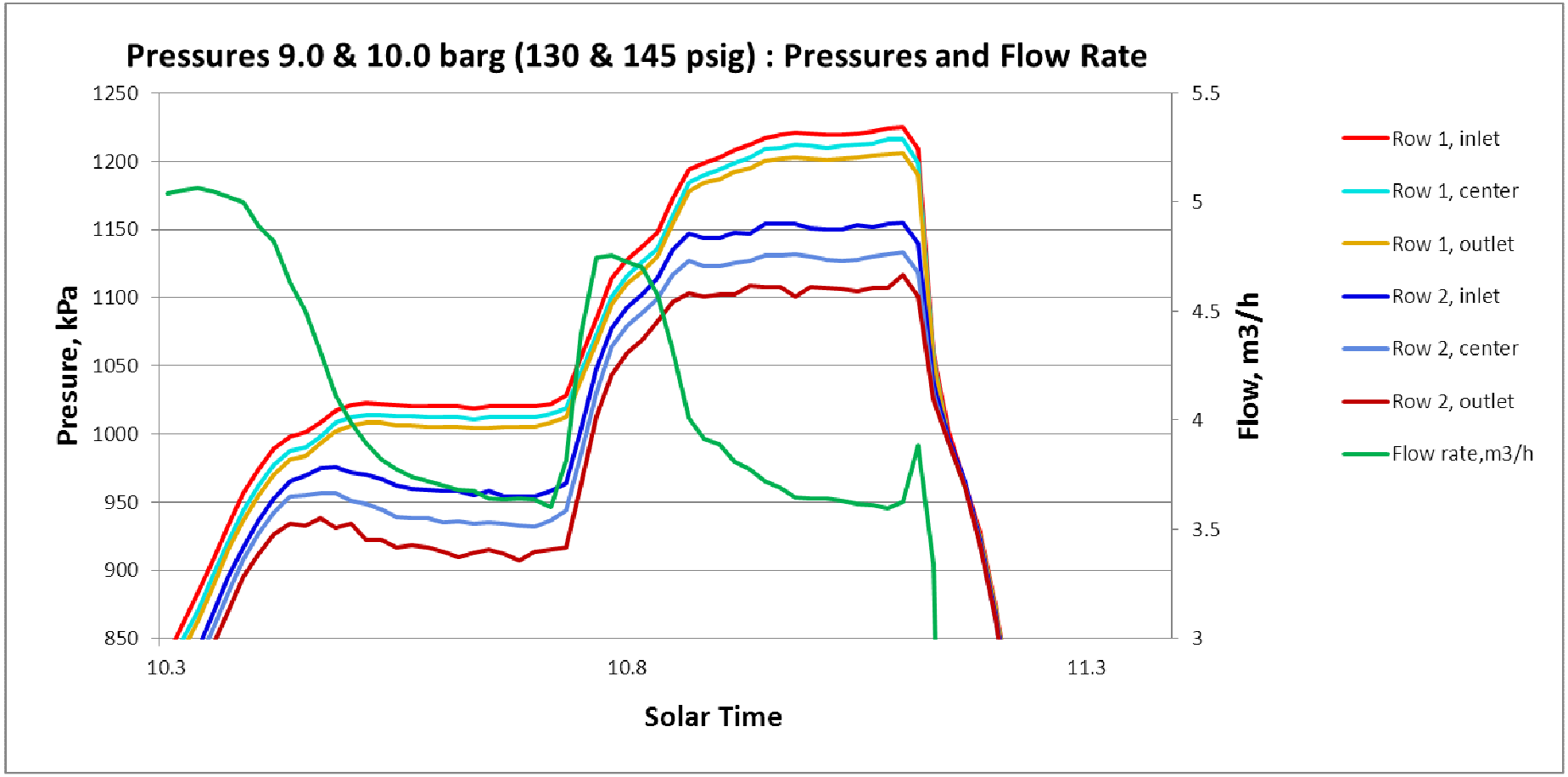

Figure D-9: Effect of Sun Intensity at 9 and 10 bar steam pressures

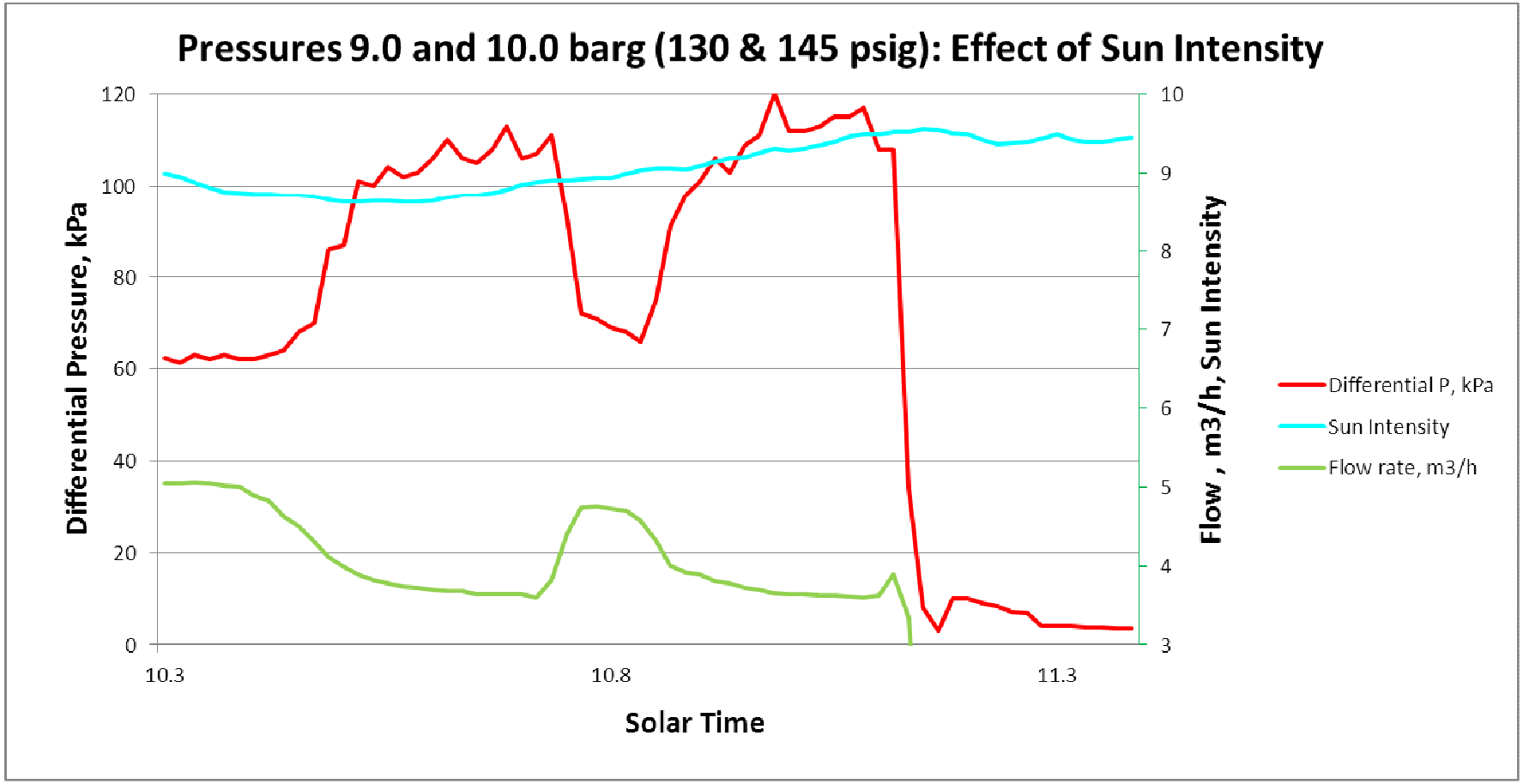

Figure D-10: Temperatures and flow rate for steam generation at 8 bar in bypass mode

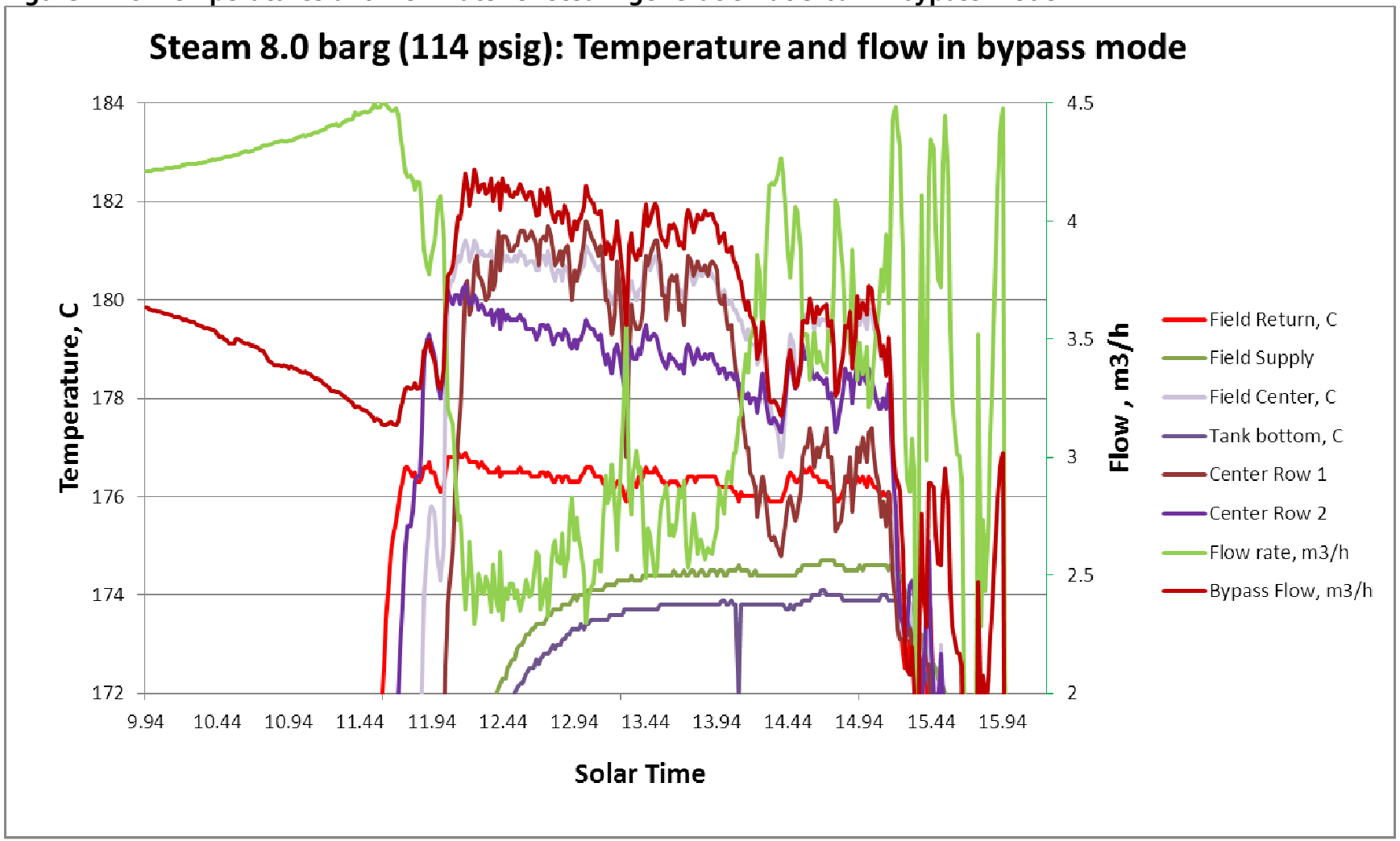

Figure D-11: Pressures and flow rate for steam generation at 8 bar in bypass mode

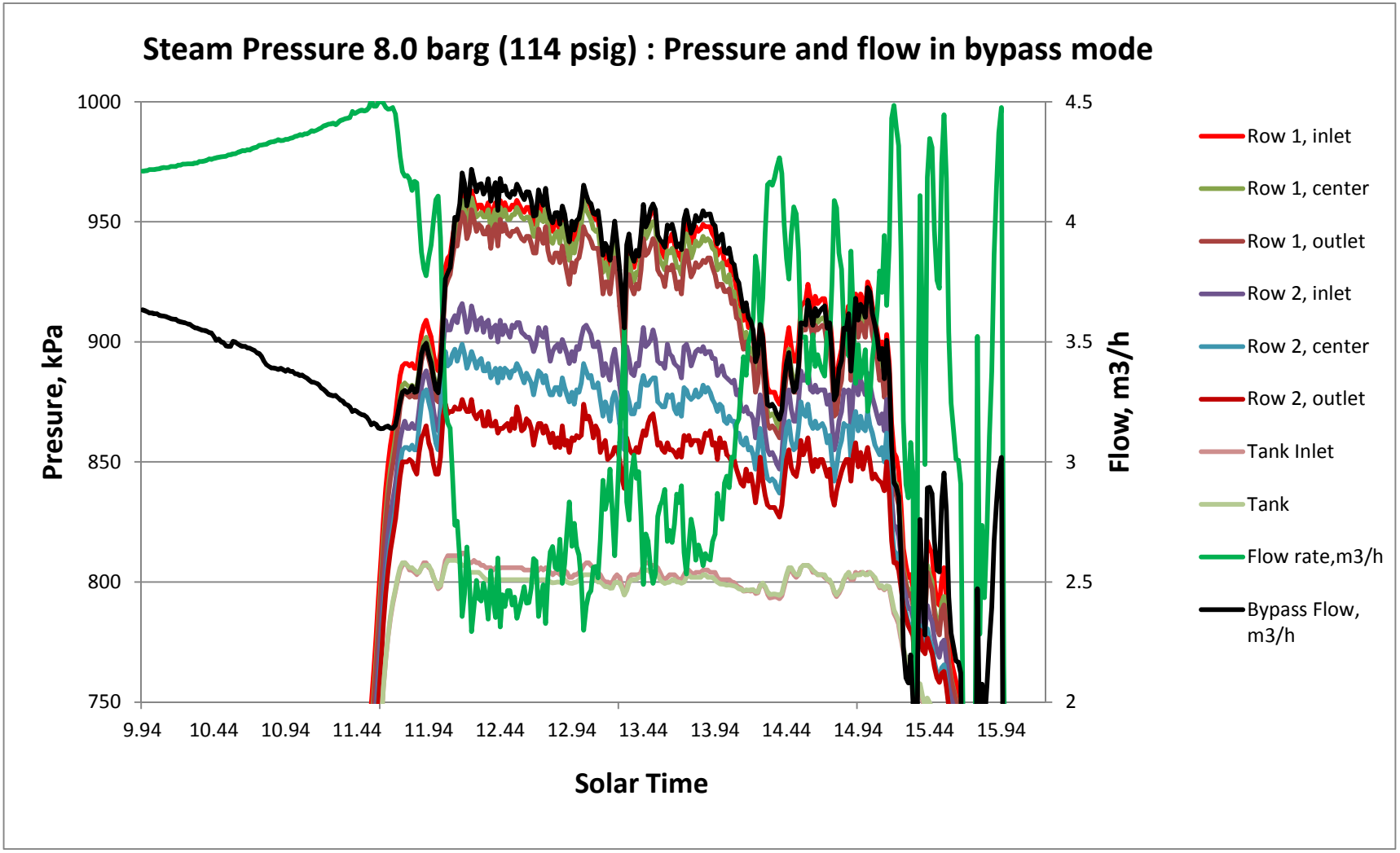

Figure D-12: Effect of Sun Intensity for steam generation at 8 bar in bypass mode

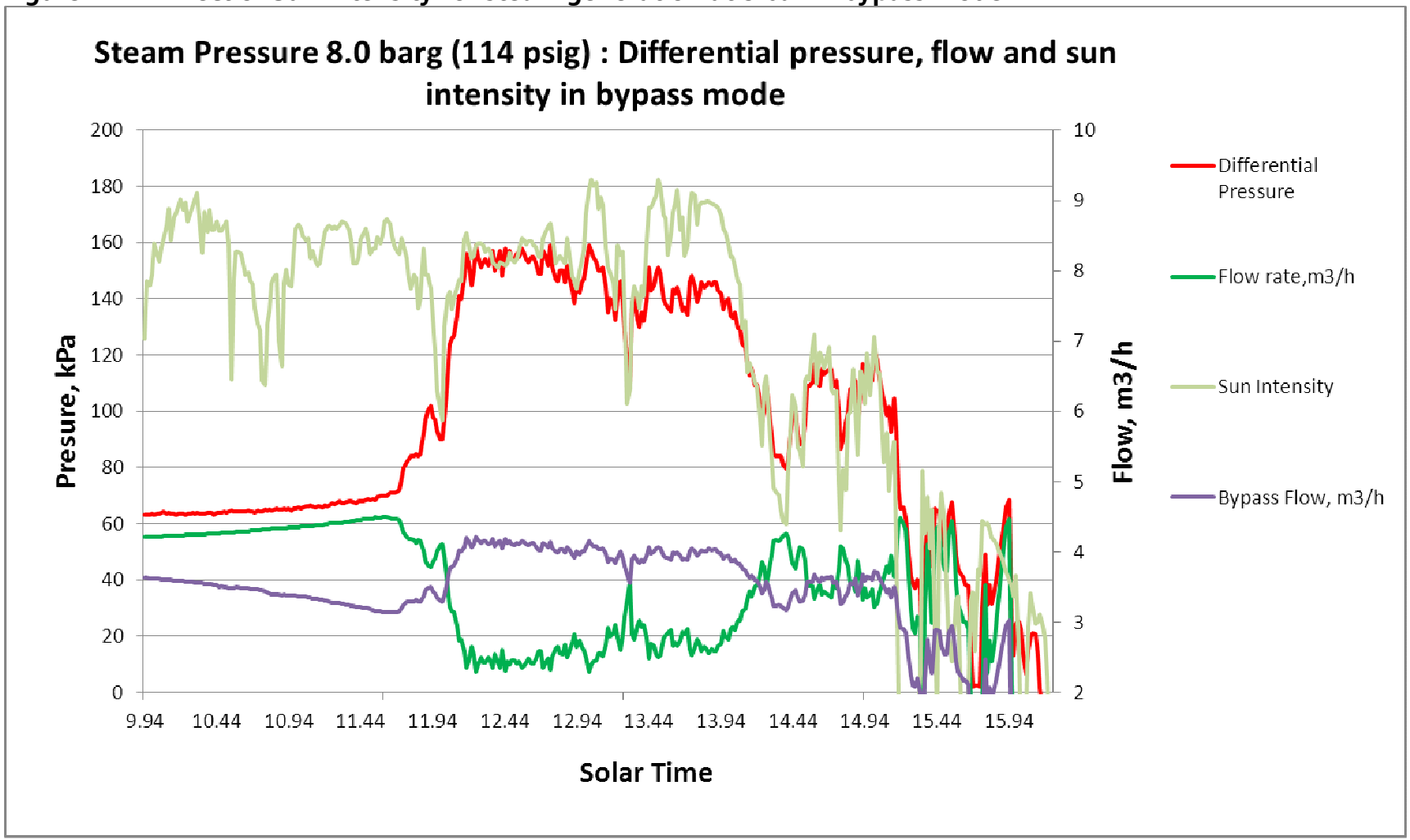

Figure D-13: Temperatures and flow rate for steam generation at 3.5 bar in bypass mode

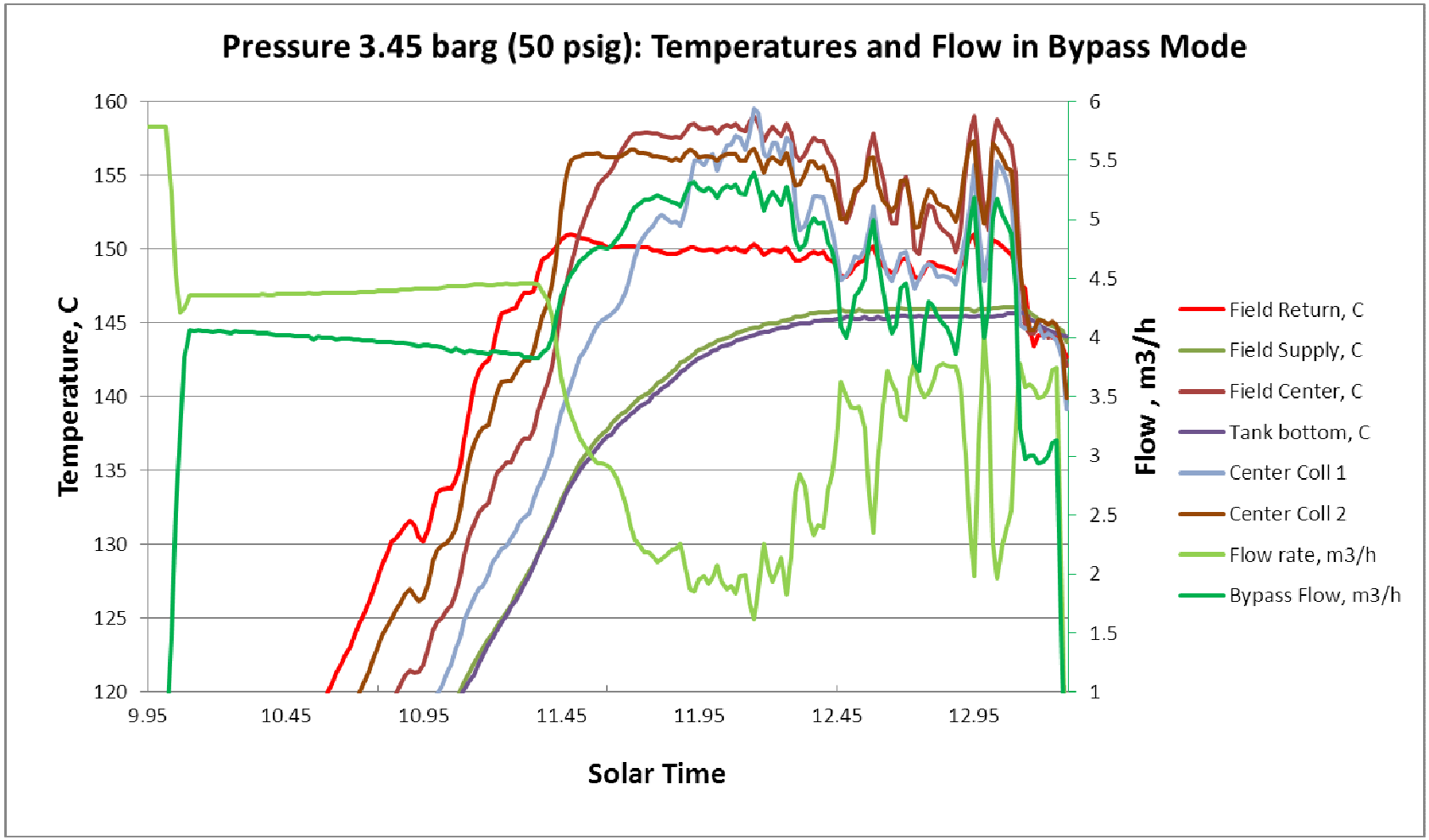

Figure D-14: Pressures and flow rate for steam generation at 3.5 bar in bypass mode

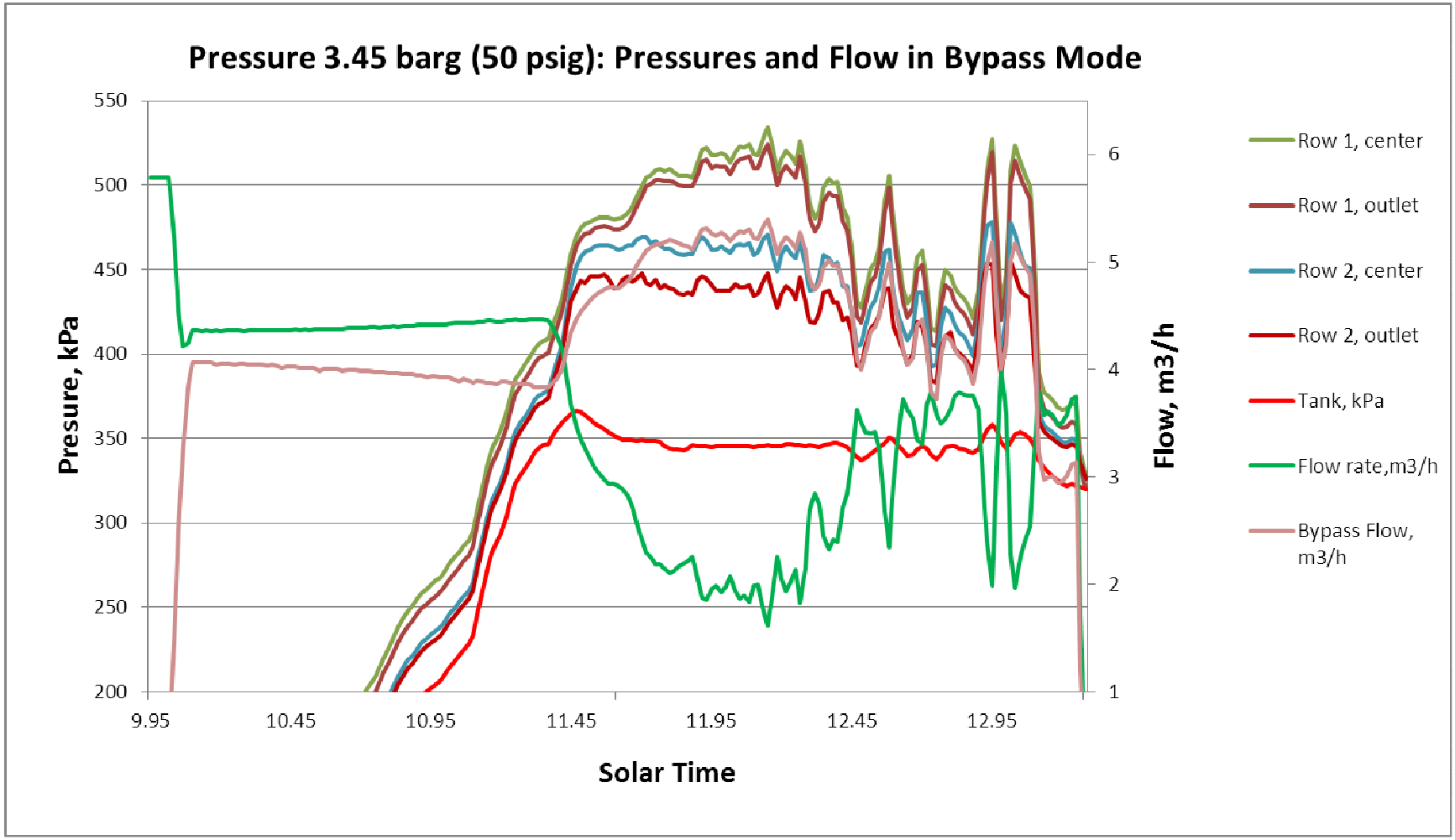
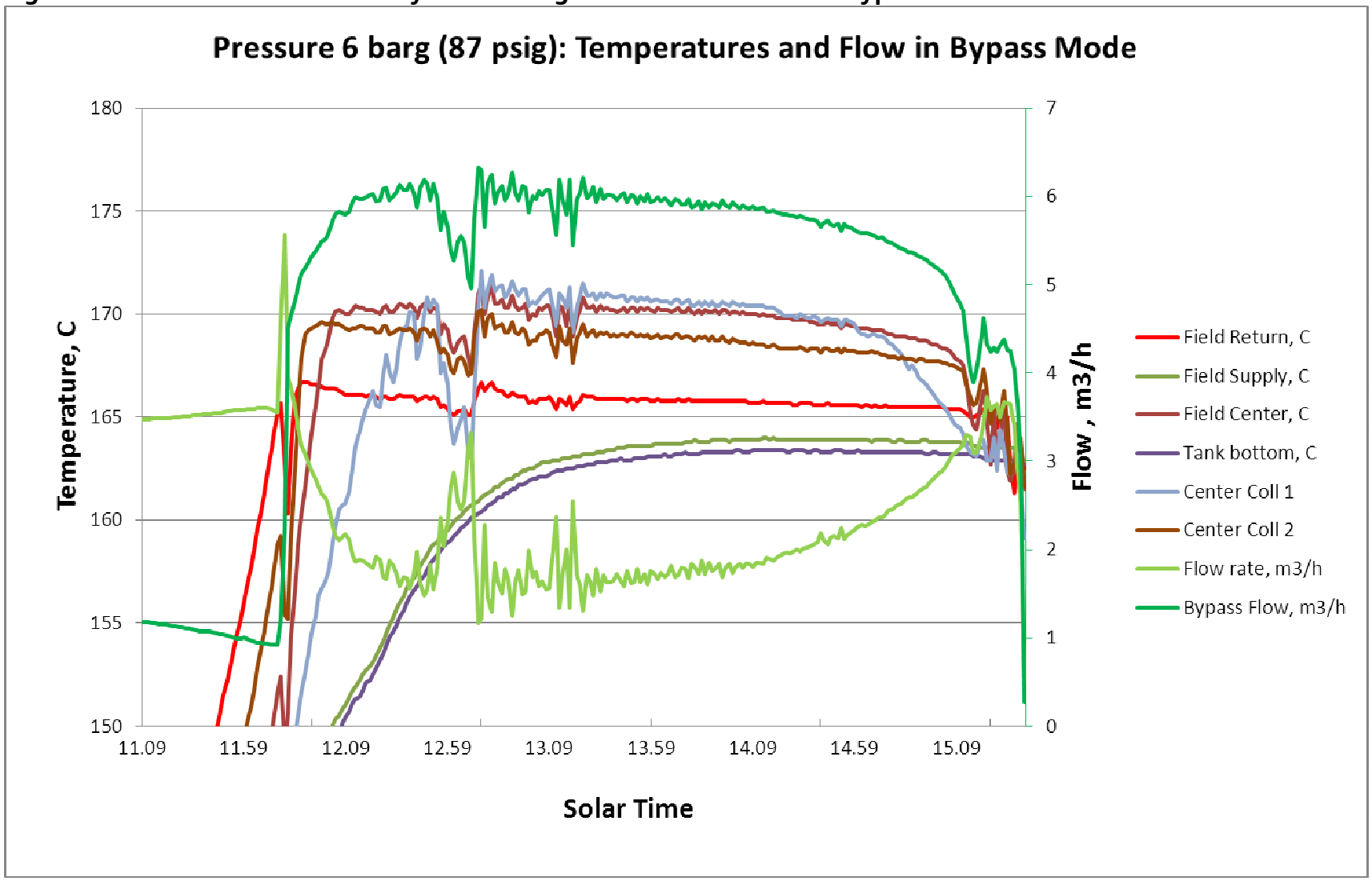
Figure D-15: Effect of Sun Intensity for steam generation at 3.5 bar in bypass mode